Experimental and theoretical investigations of the photochemistry of styrene and the creation and characterisation of shaped femtosecond ultraviolet laser pulses

Abigail Nunn

A thesis submitted for the degree of
Doctor of Philosophy

University College London
March 2010

I, Abigail Nunn, confirm that the work presented in this thesis is my own. Where information has been derived from other sources, I confirm that this has been indicated in the thesis.

...of making many books there is no end; and much study is a weariness of the flesh.

He restoreth my soul.

The flowers appear on the earth; the time of singing is come…

Abstract

This thesis is composed of three projects that are linked by the theme of light-molecule interactions. These are covered separately in Chapters 2, 3, and 4. In Chapter 1 some background to the thesis is described so that the various links between the science in the different chapters, and the motivation for the project as a whole are explained. Elements of photochemistry, both experimental and theoretical, are described in this chapter and some material about the most important experimental tools used in this work, ultrafast lasers, is covered, as well as the methodology of time-resolved spectroscopies, and time-resolved photoelectron spectroscopy in particular; the field of laser control of chemistry is also briefly reviewed. Chapter 2 is an account of the design and use of a UV pulse shaper and characterisation setup. This is an applied optics experiment, whose application is to the control of photochemical reactions with specifically shaped ultrafast laser light. Several demonstrations of the pulse shaping capacity of this new experiment are presented. In Chapter 3, calculation of the excited electronic states of the molecule styrene is described. This project is a computational study of the electronic spectroscopy and ionisation of the styrene molecule. In Chapter 4, the direct observation of internal conversion in styrene using time-resolved photoelectron spectroscopy is reported. This is an experimental laser spectroscopy project in which some of the results from the computations in the theory project, Chapter 3, will be used to analyse the experimental spectra. Chapter 5 summarises the conclusions drawn from Chapters 2, 3 and 4 and provides an outlook for future research based on the work in this thesis. Throughout this thesis, but more particularly in Chapters 1 and 2, there is quite a large volume of literature review and background material. This content reflects the personal perspective from which the thesis was approached. Much of the field of ultrafast optics and spectroscopy was entirely new to the writer at the outset of the PhD programme, and most of the review-based writing about these topics found here was originally written early on in the PhD project, as a means of helping to bridge the gap between work on optical experiment design and an undergraduate training in chemistry.

This thesis is based on the following publications

Parts of Chapters 1 and 2:

Femtochemistry and the control of chemical reactivity, Helen H. Fielding and Abigail D. G. Nunn, in *Tutorials in molecular reaction dynamics*, Edited by Mark Brouard and Claire Vallance, RSC, to be published 2010.

Chapter 2:

Frequency doubling and Fourier domain shaping the output of a femtosecond optical parametric amplifier: easy access to tuneable femtosecond pulse shapes in the deep ultraviolet, A. D. G. Nunn*, D. S. N. Parker*, R. S. Minns, H. H. Fielding, Applied Physics B 94, 181 (2009).

Parts of Chapters 3 and 4:

Ultrafast dynamics of the S_2 excited state of styrene, A. D. G. Nunn, R. S. Minns, M. J. Bearpark, M. A. Robb and H. H. Fielding, Physical Chemistry Chemical Physics, in preparation.

Acknowledgements

First of all I would like to thank my supervisor Professor Helen Fielding for allowing me to carry out a PhD in her group. I am particularly indebted to her for very thorough but very fast reading of the chapters of this thesis. I would also like to thank Dr Mike Bearpark and Professor Mike Robb at Imperial College for their supervision of my theory project; most recently, their assistance with finishing the project and writing Chapter 3 has been greatly appreciated.

I owe a debt of gratitude to many friends and colleagues who have helped and encouraged me through the course of my PhD research. Thanks go to Russell for being always so patient and helpful with all my questions and over my many mishaps in the lab. Thanks also go to Dorian for sharing the many hours spent staring at spots of light in our search for t_0. I would also like to thank all of the rest of the Fielding group, past and present who have been supportive colleagues and made the group such a friendly place to work: Rob, Rakhee, Eva, Corinne, Adam K, Adam M, Nick, Toni, Kiera, Emma, Jadranka, Maria, Ciarán and Roman. I'd also like to thank Rosie for advice about theory, and for very welcome tea breaks on many occasions!

Many other people have been helpful with practical advice and assistance during different periods of my PhD studies: Steve Firth at UCL, Matt Harvey and Simon Burbidge at the HPC service at Imperial College, Nachum Lavie at the University of Tel Aviv, members of the Walmsley Group at the University of Oxford, and other members of staff and students at UCL and Imperial.

I would like to thank my cousin Meredith and her husband Bryan for arranging their wedding so that I could have a short trip to Nova Scotia to look forward to at the end of my PhD – I was very glad to be able to be there. Most of all, I would like to thank my Dad, my Mum, my brother Jamie and my sisters Ruth and Nancy. I am very grateful for all their support for my PhD studies, and for so many other things!

Contents

List of Figures

List of Tables

Chapter 1

Introduction

This thesis is composed of three projects linked by the theme of light-molecule interactions that are covered separately in Chapters 2, 3, and 4. Chapter 2 is an account of the design and use of a UV pulse shaper – an optical instrument that can alter the properties of ultrafast laser light. The aim of this project was to create a tool with which to manipulate photochemical reactions in molecules. In the third chapter, calculations of the excited electronic states of the styrene molecule are presented, and Chapter 4 is about time-resolved photoelectron spectroscopy experiments on styrene. In this introductory chapter some background to the thesis will be described and the various links between the science in the different chapters are made clear. Firstly, some elements of photochemistry, both experimental and theoretical will be described (Section 1.1). Some background to the most important experimental tool used in this work, ultrafast lasers, will be covered (Section 1.2). The methodology of time-resolved photoelectron spectroscopy will be discussed and some results in the literature will be reviewed (Section 1.3). An alternative name for this thesis could be "Towards coherent control of styrene photochemistry", because a global aim for all the projects in this thesis has been to design an experiment in which one of the photochemical channels is optimised using ultrafast lasers. The field of coherent control is where the motivation for the work in this project is found, and therefore coherent control of chemistry will be discussed and briefly reviewed (Section 1.4). Some of the material in this chapter forms part of a chapter in a book.[1]

1.1 Photophysics and photochemistry

The experiments of Ahmed Zewail were the first experiments to record a "movie" of the progress of a photochemical reaction by using sequenced spectroscopic signatures of the nuclear motion, and the significance of his work was recognised by the award of the 1999 Nobel Prize in Chemistry.[2] Observation of bond-breaking and rearrangement processes is possible only by probing them on an ultrafast timescale, and this became practical with the advent of femtosecond lasers in the late 1980s. Controlling photochemical processes with ultrafast lasers was first suggested by Zewail, and pioneered by Gerber and Zewail in small molecules.[3,4] Development of similar experiments to control the photochemistry or photophysics of larger molecules was limited by the lack of detailed knowledge of the photochemistry involved. Recently, there has been great interest in so-called 'feedback-control' experiments that have successfully demonstrated control over chemical processes without any prior knowledge of the photochemical system involved.[5-9] This thesis presents experimental and theoretical results that pave the way for an experiment in which an ultrafast laser control scheme for the molecule styrene may be pre-determined; the hope is that the control scheme could be designed using a clear picture of the spectroscopy and dynamics of the excited potential energy surfaces of styrene from theory and experiment, and would be implemented using ultraviolet pulse shaping technology.

The Jablonski diagram summarises the basics of isolated molecular photophysical behaviour (see Fig. 1.1).

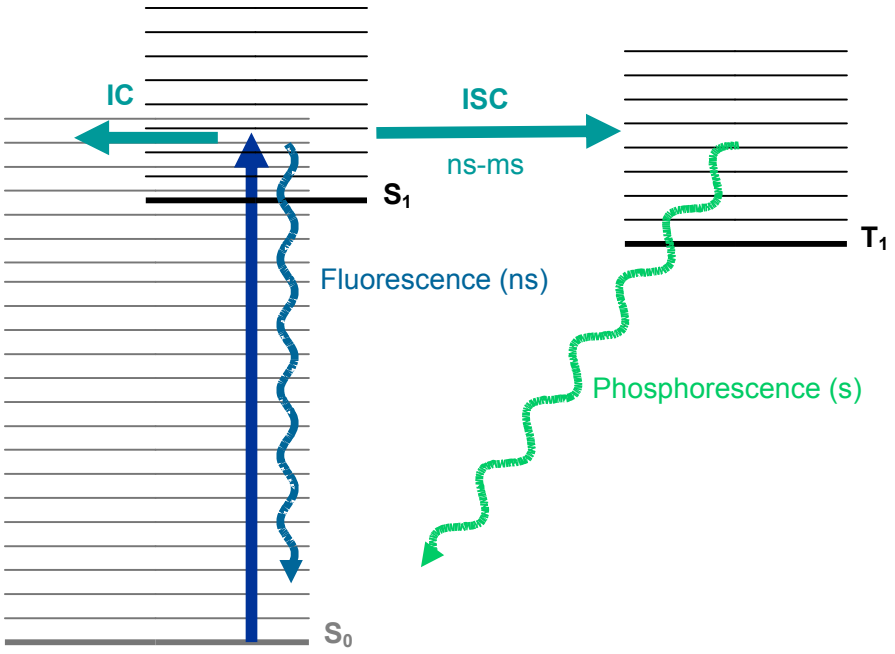

Figure 1.1 A Jablonski diagram for photophysical decay pathways from an electronically excited isolated molecule. Excitation from the electronic ground state, S_0, to the first excited electronic singlet state S_1 can be followed by either fluorescence (emission, causing decay to the ground state), internal conversion (IC - crossing to a highly excited vibrational level of the ground electronic state) or intersystem crossing (ISC) to a state in the triplet manifold. If ISC occurs then the subsequent decay can be *via* phosphorescence (emission of a photon and relaxation to the ground singlet state). Typical timescales for these processes in polyatomic molecules are given.

The timescales for internal conversions and intersystem crossings in photoexcited species can be calculated using Fermi's golden rule,

$$P \propto R^2 \left| \left\langle \psi'_{\upsilon} \middle| \psi''_{\upsilon} \right\rangle \right|^2 \rho \,, \tag{1.1}$$

where the propensity for an internal conversion or intersystem crossing, P, is dependent on the electronic transition dipole moment R, between the final and initial electronic wavefunctions, the vibrational (Franck-Condon) overlap, $\left\langle \psi'_{\upsilon} \middle| \psi''_{\upsilon} \right\rangle$, between the final, ψ'_{υ}, and initial, ψ''_{υ}, vibrational wavefunctions, and the density of (vibronic) states in the energetic region to which the crossing will occur, ρ. The value of R gives the coupling

between the two electronic states, and its form depends on the type of crossing involved. The diagram in Fig. 1.1 only shows excitation to the first excited singlet state, but according to Kasha's law,[10] excitation to higher excited states is followed by swift internal conversions or intersystem crossings to the lowest singlet or triplet state, so that phosphorecense and fluorescence are only observed from the lowest energy state of each multiplicity. The basis for this rule is the fact that the vibrationless limit of the excited states are generally closer to each other in energy than the S_1 or T_1 state is to the S_0 state, and therefore crossings between the excited states are governed by more favourable Franck-Condon factors. Intersystem crossings are facilitated by spin-orbit coupling, which is more prevalent in heavy atoms. However, in many organic species, the origin of a low-lying triplet state, T_1, is close to the S_1 state, and therefore, despite R being small for the S_1-T_1 transition, the Franck-Condon overlap will be large, and thus an intersystem crossing will be much more probable than an internal conversion to the S_0 vibrational manifold, for which the Franck-Condon overlap is likely to be very small. When a molecule is excited to a reasonably high vibrational level in S_1 or into a higher electronic state, it is likely to follow a number of different decay paths on its way back to the ground state. In Chapter 4, time-resolved spectra are presented that suggest a singlet-only decay path after excitation to S_2 and highly vibrational levels of S_1 in styrene.

From the very general one-dimensional picture described by a Jablonski diagram (Fig. 1.1), it is common to extend the picture to one with more than one dimension, in which the electronic energies of the various excited states are a function of an internuclear coordinate. For a diatomic molecule, the 1-dimensional picture, with electronic energies as a function of internuclear distance, is exact. For polyatomics it is not exact, although a 1-dimensional picture of energy *versus* reaction coordinate is often used as a simplified model or to rationalise observed behaviour. For example, a *cis-trans* isomerisation reaction is very often pictorially described by the single torsional coordinate around a double bond. A rigorous treatment, even for a very small *cis-trans* system such as a substituted ethene, necessitates consideration of all the 3*N*-6 coordinates in the molecule

when considering isomerisation within an accurate energy landscape. Before considering the complexities of a multi-dimensional potential energy surface, it is worth discussing first of all the physical origin of the potential energy surface.

The Born-Oppenheimer approximation

The non-relativistic time-independent Schrödinger equation is given by

$$\hat{H}\Psi(\mathbf{r},\mathbf{R}) = E\Psi(\mathbf{r},\mathbf{R}). \tag{1.2}$$

The total wavefunction, $\Psi(\mathbf{r},\mathbf{R})$, is a function of the spatial and spin coordinates for the electrons, $\mathbf{r}$, and nuclei, $\mathbf{R}$. Separation of the correlated electronic and nuclear motion by the Born-Oppenheimer approximation is possible because of the vastly differing masses of the two types of particles; the heavy nuclei have much greater inertia than the electrons, and so the motion of the electrons is considered to respond instantaneously to the slower motion of the nuclei. Thus, the total wavefunction is a product of electronic and nuclear wavefunctions, and the form of Eq. 1.1, as well as the Franck-Condon law, follows from this approximation. The Born-Oppenheimer wavefunction, $\Psi(\mathbf{r};\mathbf{R})$, and energy, $E_e(\mathbf{R})$, of the molecule at frozen geometry, $\mathbf{R}$, are computed with the nuclear coordinates frozen at a particular geometry by solution of the Schrödinger equation with a Hamiltonian of the form

$$\hat{H}_e = -\sum_i \frac{\hbar^2}{2m_e}\nabla_i^2 - \sum_i \sum_k \frac{e^2 Z_k}{r_{ik}} + \sum_{i\langle j} \frac{e^2}{r_{ij}} + \sum_{k\langle l} \frac{e^2 Z_k Z_l}{r_{kl}}, \tag{1.3}$$

where the terms, from left, are the sum of the electronic kinetic energies, the electron-nuclei attraction energies, the electron-electron repulsion energies, and the total potential energy of the frozen nuclei. By changing the geometry of the molecule and re-computing the energy, a detailed picture of the energy of the molecule as a function of its geometric parameters can be obtained. These are the potential energy surfaces. Multiple potential energy surfaces can be constructed by computing more than one electronic energy solution at each geometry. Linking the *n*th electronic energy solution, calculated at each point on a grid of molecular geometries in the 3*N*-6 nuclear dimensions gives the *n*th adiabatic potential energy surface for the molecule. The calculation of electronic energies of molecules is known as electronic structure theory.

Some details about electronic structure theory calculations for excited states will be described in Chapter 3, Section 3.2.

The potential energy surface obtained using the Born-Oppenheimer approximation is a potential within which the nuclei move. Using these potential energy surfaces, the nuclear wavefunction could be solved. Exact calculation of the nuclear wavefunctions within the Born-Oppenheimer approximation requires exact knowledge of the potential energy surfaces involved, and this is rarely carried out. In order to calculate nuclear energies for spectroscopic vibrational frequencies, the calculation of a small $3N$-6 dimensional region of the potential energy surface around a minimum is required, and very often a multi-dimensional harmonic potential is used as an approximation for this purpose.

Critical points

Calculation of the full dimensionality of multiple or even a single potential energy surface is not feasible for any but the smallest of molecules. However, knowledge of certain critical points on the surface allows for an understanding of the photochemical behaviour of a molecule to be built up. Classically, the nuclei can be considered to move around a potential energy surface following a Newtonian trajectory between the various structural features of the surface. In this model, after photon absorption, which leads to a vertical excitation of an excited electronic surface at the same geometry as the ground state minimum, the subsequent trajectory on the surface is dependent on the slope of the excited state potential energy surface at the geometry at which the transition takes place. Thus, an indication of the initial photoexcited dynamics may be obtained from the ground state equilibrium geometry of the molecule (the minimum on the ground state potential energy surface), and the shape of the surface in the region of the excitation, the Franck-Condon region. Numerical methods may be used to search in the full space to find the critical points such as energy minima. Given a good initial starting geometry (one that from chemical intuition is known to be close to a minimum on the potential energy surface), optimisation algorithms, usually based on the Newton-

Raphson method,[11] are able to rapidly find the nearest stationary point, which generally corresponds to the desired minimum. For some electronic structure methods, an analytical expression for the energy may be obtained, and the calculation of the gradient of the energy and the second derivative with respect to the nuclear coordinates (the Hessian matrix) of any of the *n* electronic solutions can also be calculated analytically, simplifying the optimisation of molecular geometries.

Non-adiabatic effects

The Born-Oppenheimer approximation, and the closely related adiabatic approximation sometimes invoked, is good for many situations - the Fermi Golden Rule in the form in which it is given in Eq. 1.1, with the separation of nuclear and electronic coordinates, is a consequence of this approximation - but the whole of photochemistry, as summarised by the Jablonski diagram in Fig. 1.1, is a consequence of its breakdown under certain conditions. In the Born-Oppenheimer model, light absorption is modelled by the instantaneous vertical transfer of population from the ground potential energy surface to an excited potential energy surface. A purely classical model for the nuclei then sees the population propagate on the excited surface along a path of steepest descent according to Newtonian mechanics. Within this model, the probability of crossing between the surfaces (conical intersections) can be computed using the Landau-Zener model in which the probability of a radiationless decay between two surfaces increases with the speed of the nuclear coordinate motion and with the difference in slopes of the two surfaces, and decreases with the size of the energy gap between the electronic states. A quantitative measure of the rate of decay may be obtained by calculation of the nonadiabatic coupling matrix element, which for a singlet-singlet coupling is a function of the nuclear kinetic energy operator.[12] To get an exact understanding of the behaviour of the wavefunction after photoexcitation, the time-dependent Schrödinger equation must be solved

$$i\hbar \frac{\partial \Psi(\mathbf{r},\mathbf{R},t)}{\partial t} = \hat{H}\Psi(\mathbf{r},\mathbf{R},t). \tag{1.4}$$

The total wavefunction (electronic and nuclear) can be expanded in a basis that is the complete set of solutions to the electronic Schrödinger equation.

Conical intersections

Conical intersections (CI) are an important class of nonadiabatic effect. The discovery of their ubiquity was a major development of a modern understanding of photochemistry. Conical intersections occur where the potential energy surfaces cross. In a diatomic molecule, electronic states of the same symmetry will not cross. However, for a molecule with more than one degree of freedom, the symmetry of the state can be lowered by deformation and real surface crossings between potential energy surfaces exist. In the two dimensions that form the branching space, a surface crossing appears as a funnel or pair of inverted cones. In the full molecular space, a conical intersection is a 3*N*-8 dimensional hyperline. The existence of real crossings in molecules allows for the prediction of internal conversions that are faster than those predicted by the earlier avoided crossing model, due to the energy degeneracy of the states at the intersection, and this has been observed in many molecules.[13]

The conical intersection forms a part of the photophysical and photochemical reaction pathway of molecules; in this model, points on the excited state (Franck-Condon region, minima, transition states and conical intersections) are linked by a path of steepest descent. The CI acts as a point from which the reaction may branch, as the population moves from the higher to the lower state, with at least two paths being created on the cone of the lower surface. The exact structure of the CI can be used to determine the photochemical stability of molecules in which one of the branches of the reaction pathway leads to the ground state reactant geometry. Algorithms have been developed that are able to search for a conical intersection from the Hessian and gradient of the electronic energy for a state, as calculated by some *ab initio* electronic structure methods. The reaction pathway approach to photochemistry has been described more fully and reviewed elsewhere.[14]

Other light-induced processes

The photochemical reaction pathway model described above is really a pathway for photochemical isomerisation or bimolecular photochemical reactions. Other light induced processes such as photodissocation and photoionisation often occur under conditions of higher light intensity, sometimes in multi-photon absorption processes. Typical ionisation energies for small polyatomic molecules are around $9-15\,\mathrm{eV}$ and therefore require multiple visible or UV photon absorption or a vacuum UV single photon absorption. Photoionisation is generally modelled as a vertical process. At the most basic level, the photoionisation propensities can be determined, like electronic excitations, from the molecular orbital structure. In Koopmans' theorem, the first ionisation energy of a molecule is minus the energy of the highest occupied molecular orbital. For excited states, the ionisation energy can be given using the same approach, taking the energy of which ever orbital is promoted, assuming the state is described by a single excitation process. A more general approach to ionisation of the excited states of a molecule can be derived from this by calculating the difference between the energy of the excited neutral of a particular electronic configuration and the energy of the ion with the same configuration, minus the highest energy electron. For a multi-configurational excited state, the relative ionisation propensities to the cation states may be determined similarly by comparison of the configuration weights for the excited state to the electronic structures of the cation states. Analysis of the Koopmans'-type single electron ionisation correlations are useful for deciphering the ultrafast dynamics that are measured in ultrafast time-resolved photoelectron spectroscopy experiments. Before describing some of the particular effects of ultrafast light on molecules, a few definitions of ultrafast laser light must first be discussed.

1.2 What is an ultrafast laser pulse?

Laser light is coherent and in traditional laser sources, it is also monochromatic. By contrast, in femtosecond laser cavities, electromagnetic laser radiation oscillating with a

range of frequencies creates the interference required to spatially localise the optical field into a travelling ultrashort pulse. Localisation of the different frequencies ('modes') is known as mode-locking. Intuitively, the duration of the pulse is in inverse proportion to the range of frequencies of which it is composed, and the minimum pulse duration, Δt, for a given range of photon energies, ΔE, or optical frequencies, $\Delta \nu$, is limited, in accordance with the uncertainty principle:

$$\Delta E \Delta t \geq \hbar , \tag{1.5}$$

$$\text{or} \quad \Delta \nu \Delta t \geq 1/2\pi . \tag{1.6}$$

Together, the duration, Δt, and the bandwidth, $\Delta \nu$ (or the more commonly expressed angular frequency width, $\Delta \omega$), are fundamental properties of ultrashort laser pulses and they represent a pair of properties, implying information about the time-domain intensity profile and frequency-domain intensity profile (the spectrum) respectively; they give an indication of how close the laser pulse is to the limiting value predicted by the uncertainty principle (the transform limit).

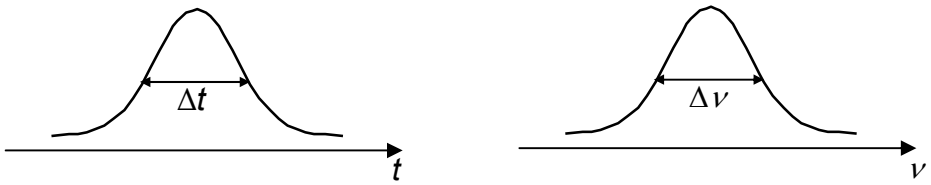

Figure 1.2 Time and frequency domain electric-field envelope intensities of an ultrashort Gaussian laser pulse. This shape is a typical output for many femtosecond laser cavities. A Gaussian time-domain pulse Fourier transforms to a frequency-domain Gaussian pulse. The pulse duration, Δt, and spectral width, $\Delta \nu$, shown are the full-width at half maximum (FWHM). The FWHM is most usually used in the literature to describe a pulse, although the uncertainty principle as given in text (Eq. 1.6) strictly describes the root mean-square (RMS) quantities.

Deviations from the uncertainty principle limit, *i.e.*, pulses with temporal durations larger than predicted by Eq. 1.6, arise from the different frequency components of the laser pulse electric field being out of phase with one another: the case of optimal spatial

and temporal localisation of a pulse is called a 'transform limited' laser pulse, and most laser cavities emit pulses in which some of the modes are slightly out of phase, *i.e.*, they occur at slightly different times. A depiction of a transform limited ultrashort pulse is shown in Fig. 1.3.

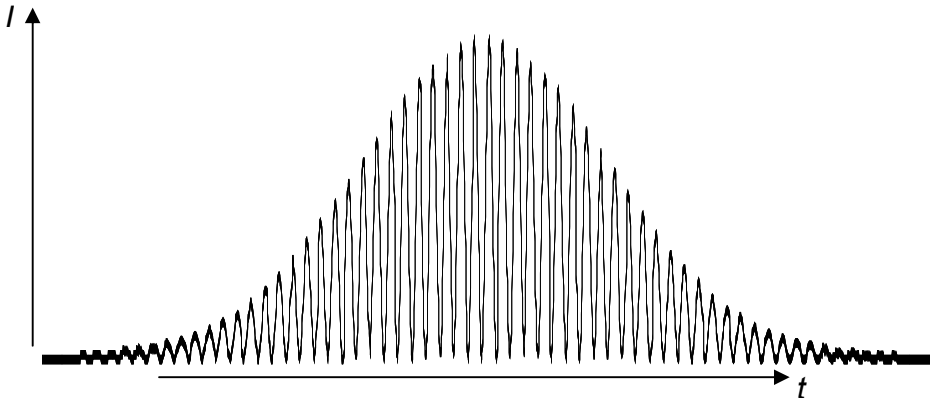

Figure 1.3 A plot of a laser pulse produced by a typical idealised mode-locking cavity. The horizontal axis is time, with the total time of the pulse of the order of 10^{-15} s (femtoseconds). The vertical axis is the intensity of the electric field produced by the mode-locked cavity. The pulse shape is the product of a carrier oscillation and a Gaussian envelope. The carrier oscillation frequency is the average frequency of the modes that are "locked" together in the cavity; the width of the envelope defines the duration of the pulse. This drawing is approximately to scale for a pulse with a carrier frequency around 800 nm, and duration in the 10s of femtoseconds.

A definition of the electric field of a laser pulse may be given in either the time *or* the frequency domain, by specifying the amplitude (or intensity) and phase of the different temporal or frequency components of the complex light electric field. The phase of a travelling wave at any point in time is always a function of both its time and its frequency of oscillation. The relative temporal positions of a pair of frequencies of the laser pulse can be given in terms of the phase difference between them. Similarly, the difference between the carrier oscillation phases at two different times in the laser pulse electric field will be a function of its frequency. Thus, phase forms a link between the

frequency and time domains. The real time-domain electric field, $\varepsilon(t)$, neglecting entirely its spatial (or reciprocal space) variation, is

$$\varepsilon(t) = \tfrac{1}{2}\sqrt{I(t)}\exp\{i[\omega t - \phi(t)]\} + c.c., \tag{1.7}$$

where $I(t)$ is the intensity as a function of time, and $\phi(t)$ is the phase as a function of time. The slowly varying envelope approximation (SVEA) allows the fast carrier phase oscillation, $\exp[i\omega t]$, to be factorised out. This is the assumption that the optical carrier phase varies so much more quickly than the pulse envelope, that the relative phase between the pulse envelope and the carrier oscillation, (termed the "absolute phase" in the literature) is independent of the pulse envelope; this is valid for pulses such as that shown in Fig. 1.3, and indeed is valid for all but the very shortest femtosecond pulses in the near infrared and at shorter wavelengths. Using the SVEA together with the analytic signal approximation to ignore the complex conjugate (*c.c.*), the analytic electric field, $E(t)$, can be defined:

$$E(t) = \sqrt{I(t)}\exp[-i\phi(t)], \text{ or} \tag{1.8}$$

$$E(t) = |E(t)|\exp[-i\phi(t)]. \tag{1.9}$$

Thus, the phase, $\phi(t)$, and amplitude, $|E(t)|$, of a single complex function define the temporal domain light field. This expression (Eq. 1.9) will be referred to from now on simply as the electric-field. Fourier transforming $E(t)$ and centring at the carrier frequency gives the frequency-domain electric field, $\tilde{E}(\omega)$, in terms of a spectral amplitude, $|\tilde{E}(\omega)|$, and spectral phase, $\varphi(\omega)$.

$$\tilde{E}(\omega) = |\tilde{E}(\omega)|\exp[-i\varphi(\omega)]. \tag{1.10}$$

The spectral amplitude is the square root of the spectrum, an easily measured property of a short laser pulse, but in order to Fourier transform the pulse to the time domain, to assess the impact of spectral pulse manipulation on the temporal profile of the pulse, the spectral phase must also be measured, and this is a more challenging technical problem. Some details about current experimental pulse characterisation methodology are reviewed in Chapter 2.

Chirped pulses and phase

Passing an ultrashort pulse through any medium creates a chirped pulse. The time domain picture of a chirped, approximately Gaussian pulse is like that in Fig. 1.3, except with a net lowering or raising of the carrier phase frequency across the duration of the pulse (see Fig. 1.4). Such a pulse can be generated easily by passing a femtosecond pulse through a medium such as glass, or even air. The phase increase across the pulse is a quadratic function of time, and the duration of the pulse is increased with respect to the transform limit. It is the frequency-dependence of the refractive index of a material that induces chirp. A short pulse has a large bandwidth, so the temporal stretch produced after it passes through a medium will be high. For example, a 30 fs pulse centred at 800 nm will be stretched to 51 fs when passing though 1 cm of an optical glass.[†]

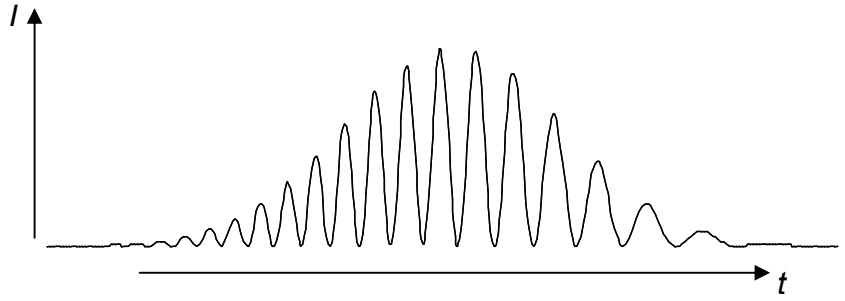

Figure 1.4 Intensity profile of a chirped, Gaussian envelope, pulse plotted as a function of time. Such a pulse has a negative quadratic variation of phase with time and a Gaussian intensity envelope with time. In the frequency domain, the pulse also has a Gaussian intensity and a quadratic phase.

Both the temporal and spectral phases are commonly expanded as a function of their derivatives in a Taylor series about the central time, t_0, and central frequency (carrier phase frequency), ω_0, respectively:

[†] This value can be computed from a literature value of the group velocity dispersion (GVD, see p27), which is 44.7 fs^2 mm^{-1} for BK7 glass,[15] and the expression for the new time duration as calculated from the initial time duration, Δt, of a transform limited pulse, using $\Delta t_{new} = \sqrt{\Delta t^4 + \left(4\phi'' \ln 2\right)^2} \Big/ \Delta t$, as described in Ref. 16.

$$\phi(t) = \phi(t_0) + \phi'(t - t_0) + \tfrac{1}{2}\phi''(t - t_0)^2 + \ldots \tag{1.11}$$

and

$$\phi(\omega) = \phi(\omega_0) + \phi'(\omega - \omega_0) + \tfrac{1}{2}\phi''(\omega - \omega_0)^2 + \ldots, \tag{1.12}$$

where the zeroth order phase is the same quantity, $\phi(t_0) \equiv \phi(\omega_0)$, and is the absolute phase of the carrier oscillation of the laser pulse relative to its intensity envelope. The zeroth order phase is not a measurable quantity, and because of the SVEA, it is of little physical importance. The first order terms in both the angular frequency and time expansions of the phase terms are also of little interest. In the frequency domain, a phase that increases linearly with frequency, *i.e.*, a non-zero value of $\phi'(\omega)$, corresponds to a shift in time from t_0. Analogously, in the time domain, a linear phase, a non-zero value of $\phi'(t)$, corresponds to a frequency shear away to a higher or lower value of the carrier oscillation frequency, ω_0. The linear chirp, $\phi''(\omega)$, in the frequency domain is also called the group delay dispersion (GDD). The amount of chirp can be calculated from the group velocity dispersion (GVD) for a material. GVD is the amount of GDD per unit length, usually measured in units of fs^2 mm^{-1}. From the GDD, the expected increase in pulse duration for an initially transform limited pulse may be calculated (see footnote on preceding page). Fig. 1.5 illustrates the role of the different orders of phase.

The losses of coherence within femtosecond pulses produced by mode-locked laser cavities are a major technological challenge for laser cavity design. But of more interest to us in the context of this thesis is the possibility of *utilising* specific differences in phase between sections of the bandwidth of an ultrashort pulse, as a mechanism by which the branching ratio of a photochemical reaction may be optimised, as described in Section 1.4. Using commercial pulse shaping technology, the phase of a light pulse can be manipulated to take any functional form. This is discussed in more detail in Chapter 2, where an experiment that creates and characterises UV femtosecond light pulses is described.

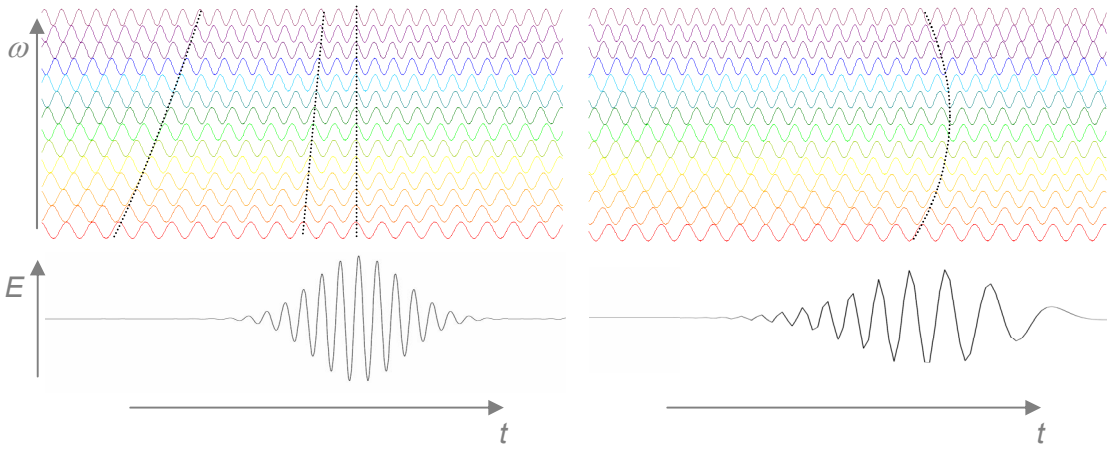

Figure 1.5 Illustration of the role of phase in defining ultrafast pulse electric field structure. The left-hand panel shows a transform limited pulse, $\phi''(\omega) = 0$, and some of the frequencies of which it is composed. The right-hand panel shows a negatively chirped pulse, $\phi''(\omega) < 0$. The dashed lines on both panels join some of the phase fronts, and it is clear that for the transform limited pulse, the phase-fronts combine coherently and add at the pulse maxima. By contrast, it is also clear that such a coherent maximum does not exist for a chirped pulse, where the phase fronts are arranged quadratically as a function of both frequency (top) and time (bottom), and hence the duration of this pulse is always increased, and its peak intensity reduced, with respect to the transform limited pulse. The linear instantaneous frequency characteristic of the linearly chirped pulse is obvious in the temporal waveform shown in the lower part of the right-hand panel: the early-time part of the pulse is 'redder,' and the later-time part of the pulse is 'bluer'. On the left-hand panel, some of the phase-fronts that are linear with frequency are highlighted to illustrate the role of non-zero value of $\phi'(\omega)$.

The central wavelength of a femtosecond laser pulse propagates at the phase velocity, while the modulating pulse envelope moves at the group velocity. In vacuum, the phase velocity of the pulse,

$$v_p = \omega / k \,, \tag{1.13}$$

and the group velocity,

$$v_g = d\omega / dk \,, \tag{1.14}$$

are constant and equal to *c*. In a medium, solid, liquid or gas $v_p \neq v_g$ because the refractive index, *n*, is a function of ω, and hence a temporal spreading of frequencies, dispersion, and non-zero GDD and GVD (group velocity dispersion) occur.[‡] Two other properties that are a measure of the shape or the chirp in a pulse, the group delay, $t_{group}(\omega)$, and the instantaneous angular frequency, $\omega_{inst}(t)$, may be defined:

$$t_{group}(\omega) = d\phi(\omega)/d\omega, \tag{1.15}$$

$$\omega_{inst}(t) = \omega_0 - d\phi(t)/dt. \tag{1.16}$$

The group delay is a function of the derivative of the spectral phase and is a measure of the temporal position of a frequency in a pulse. The instantaneous frequency is, as its name implies, a measure of the frequency at a particular time in a pulse. In a linearly chirped pulse the instantaneous frequency is a linear function of time, hence the name, 'chirp'; if the average frequency increases with time it is called a positive chirp and if it decreases with time it is called a negative chirp.

It is possible to define an ultrashort pulse without using a phase as in Eq.s 1.9 and 1.10, but instead using a joint time-frequency representation. Wigner functions and spectrograms are two such representations. A well-known example of a spectrogram from acoustics is the musical score; in optics, it is defined in terms of the optical electric field, $E(t)$, and a gate, $g(t-t')$, by

$$S(t',\omega') \equiv \left| \int_{-\infty}^{\infty} E(t) g(t-t') \exp(i\omega' t)\, dt \right|^2. \tag{1.17}$$

A spectrogram provides an intuitively useful map of the frequency intensity as a function of time for the pulse. An example spectrogram is shown in Fig. 1.6. An important class of ultrafast pulse measurement techniques is based on experimentally recording the spectrogram of the laser pulse. This is discussed in more detail in Chapter 2, Section 2.4.

[‡] Although group velocity dispersion (GVD) quantifies the GDD per unit length, GVD is often used as a general term to describe the stretching or compression of an ultrafast pulse in a medium.

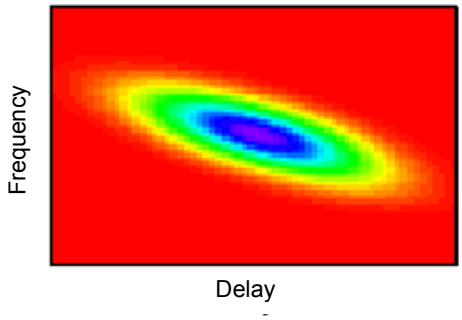

Figure 1.6 A Spectrogram showing a negatively chirped pulse. The intensity variation is shown using colour, with red for the lowest intensities and purple for the highest. The envelope of the electric field amplitude (or intensity) for this pulse is Gaussian, in the time and frequency domains, the phase, in both the time and frequency domains is quadratic, and the instantaneous frequency is linear (compare with the intensity profile of the negatively chirped pulse shown in Fig. 1.4). Figure adapted from Ref. 17.

Examining Eq. 1.17, it can be seen that the spectrogram is closely related to pump-probe spectroscopy experiments, where a pump-laser pulse is used to excite a molecular species, and after a delay a probe laser is used to project the excited species to a state where an observable can be monitored. In s spectrogram, the gate, $g(t-t')$, acts as the probe in a pump-probe process. Pump-probe spectroscopic methods are the subject of the next section of this chapter.

1.3 Time-resolved spectroscopy

There has been an explosion in activity in the field of ultrafast spectroscopy during the last decade since the award of Zewail's Nobel Prize in 1999. A wide variety of problems have been investigated, ranging in complexity from simple bond breaking in diatomic molecules, to intramolecular processes in larger molecules such as internal conversion, isomerisation and electron transfer. There are a number of excellent reviews describing the scientific achievements, for example, see Ref. 18 and references therein.

Even the fastest electronic devices cannot measure femtosecond transients, so femtochemistry experiments employ an optical pump-probe technique to follow the molecular dynamics, in which the pump laser pulse initiates a chemical reaction or creates a non-stationary state known as a wave packet. A probe laser pulse is then fired at a series of precisely-timed intervals after the pump pulse and is configured to generate an observable that will provide information about the evolving system. Exactly how much and which type of dynamical information can be retrieved from a pump-probe experiment is highly dependent on the excitation scheme and the observation method, and so a great deal of effort is directed towards developing innovative detection schemes to map out as much of the dynamical pathway as possible.

The pump-probe method itself was pioneered over 60 years ago by George Porter and Ronald Norrish, who were awarded part of the 1967 Nobel Prize for Chemistry for their investigations of 'extremely fast' chemical reactions.[19,20] The concept is illustrated schematically in Fig. 1.7. A pump pulse excites the system of interest from its initial state into an excited state that subsequently evolves along a reaction coordinate. This first pulse defines the zero of time. The excited state is transferred into a new state whose population can be monitored by the probe pulse which is fired at Δt. The delay is controlled using an optical delay line in which a moveable mirror is mounted on a computer-controlled translation stage that is capable of very precise movements ($\Delta t = 10$ fs corresponds to 3 μm path difference). Many gas-phase dynamics experimental techniques – absorption spectroscopy, resonance-enhanced multi-photon ionisation (REMPI) and laser induced fluorescence (LIF) – may be used in combination with femtosecond lasers as a probe measurement method in order to deduce valuable time-resolved information.

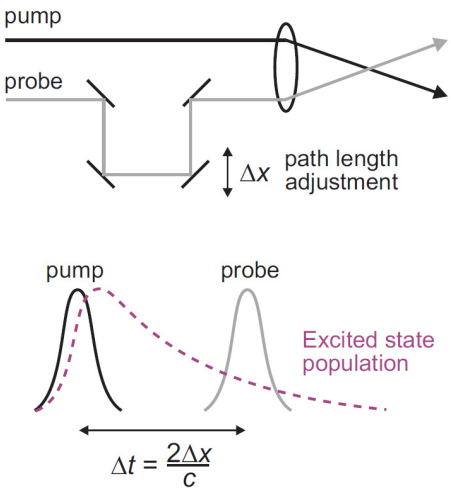

Figure 1.7 Two-colour pump-probe experiment. Two femtosecond laser beams are delayed with respect to one another using a delay line and the two beams are then focussed together into a molecular sample (top). The first beam, pump (black solid line), produces an excited state population in the sample (purple dashed line), that the second beam, probe (grey solid line), is allowed to probe at different values of delay, Δt, by creating an observable signal. Figure adapted from Ref. 1 with permission of the Royal Society of Chemistry.

The large spectral width of a femtosecond light pulse results in a number of molecular eigenstates being excited coherently. This coherent superposition of wave functions then evolves in time. Following on from the work of Zewail[21] and others, most of the experimental pump-probe signals have been interpreted as resulting from a coherent superposition of vibrational wave functions, $\psi_\upsilon(R)$. This wave packet can be written as

$$\Psi(R,t) = \sum_\upsilon a_\upsilon g_\upsilon \psi_\upsilon(R) e^{-i\omega_\upsilon t}, \tag{1.18}$$

where a_υ are the transition dipole matrix elements connecting the excited vibronic states to the initial state, and here g_υ is the amplitude of the laser field at each excitation frequency within the spectral profile of the laser pulse, which is assumed to be transform limited. In accordance with the simple picture of a photochemical reaction path arising from a Born-Oppenheimer treatment of photodynamics, the wave packet oscillates back

and forth along the internuclear coordinate at the vibrational period, like a classical particle.

When projecting a molecular wave packet onto a final state, it is necessary that the transition to the final state is fairly well understood in order for the dynamics of the excited state to be deconvoluted successfully from the final state excitation probabilities. The most versatile techniques are able to project the entire excited state wave packet onto a measurable signal that can be dispersed in energy, so that any transfer between different energy channels may be observed. Thus, the choice of probe in a pump-probe experiment is critical in determining what aspect, or aspects, of the excited state dynamics may be observed.

A classic illustration of nuclear vibrational wave packets is an elegant experiment in Na_2 performed by Gustav Gerber and his colleagues.[22] The excitation scheme is shown in Fig. 1.8. From the Na_2 $X^1\Sigma_g^+$ ground electronic state, a femtosecond pump pulse creates a vibrational wave packet in the $A^1\Sigma_u^+$ state that oscillates with a period of 306 fs, from an excitation that spans the $\upsilon' = 10-14$ vibrational levels. The same femtosecond pump pulse also creates a wave packet in the $2^1\Pi_g$ state ($\upsilon^* = 11-18$) state that oscillates with a period of 363 fs. A delayed, but otherwise identical femtosecond probe pulse is used to probe the wave packet motion in both states and the detected signal is the number of Na_2^+ ions formed from both states. Two-photon ionisation from the inner turning point of the A state leaves the Na_2^+ ion in its $^2\Sigma_g^+$ state. Single-photon excitation from the outer turning point of the $2^1\Pi_g$ state wave packet excites a doubly excited Rydberg state, which autoionises to Na_2^+ ($^2\Sigma_g^+$), and then dissociates to give Na^+ and Na(3s). A Fourier analysis of the pump-probe signal reveals the two sets of vibrational spacings in the wave packets, and the position of the envelope maximum with respect to the zero-of-time in the Na_2^+ ion signal as a function of pump-probe delay reflects the 180° phase-shift between the absorption of the probe photons by the two wave packets, at the inner and outer turning points of their respective origins.

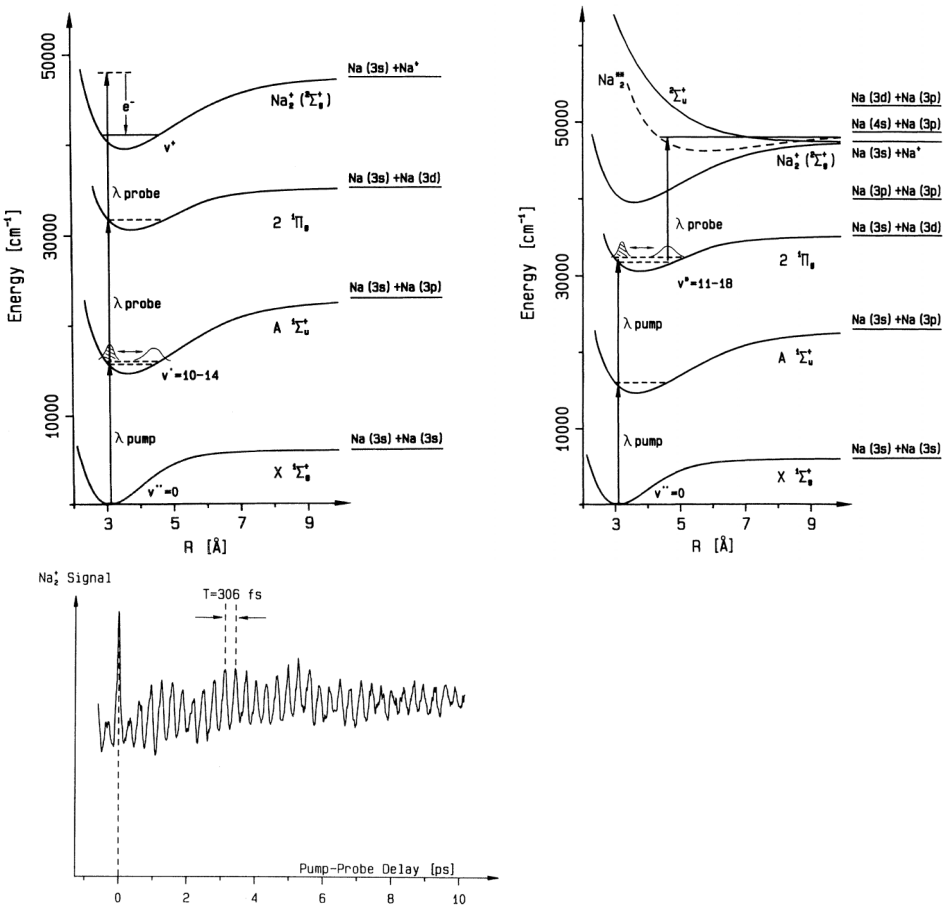

Figure 1.8 Na_2 potential energy curves (top). A wave packet is produced on each of the $A^1\Sigma_u^+$ (left) and $2^2\Pi_g$ (right) states of the neutral molecule and probed at the inner and outer turning points, respectively. The total population of Na_2^+ ($^2\Sigma_g^+$) is the probe signal (bottom), with the wave packet oscillation period in the $A^1\Sigma_u^+$ state (306 fs) apparent at a maximum in the envelope structure. Figure reprinted with permission from Figs. 1, 2 and 4 in T. Baumert, M. Grosser, R. Thalweiser *et al.*, Physical Review Letters 67 (27), 3753 (1991). Copyright 1991 by the American Physical Society http://link.aps.org/doi/10.1103/PhysRevLett.67.3753.

The photodissociation of NaI was a landmark experiment in the development of the field of femtochemistry.[23] The relevant potential energy (PE) curves for NaI photodissociation are presented in Fig. 1.9. The lower energy adiabatic PE curve has ionic character for small internuclear separations *R*, and is covalent for large *R*. The

opposite is true for the higher energy adiabatic PE curve, which is covalent for small *R* and ionic for large *R*. Ahmed Zewail's experiment used a femtosecond pump laser to promote the molecule from the ground state to a coherent superposition of excited vibrational states. The NaI molecule then oscillates within the excited PE well, but each time the Na-I bond length reaches about 0.25 nm, there is a 10% probability that the wave packet crosses non-adiabatically to the lower PE curve to form neutral Na and I atoms. The remaining excited state population continues to oscillate within the upper PE curve. Varying the probe wavelength changes the position of the 'observation window' allowing the dynamics to be observed at different points on the excited state. When the probe is tuned to 589 nm it is resonant with the Na D-line transitions. These transitions occur for very large (essentially infinite) Na-I bond lengths and the fluorescence signal obtained provides a measure of the total number of dissociated Na atoms. If the probe is tuned off-resonance from the Na D-line transitions, it monitors the population of the bound wave packet oscillating within the upper PE curve, *i.e.*, it provides a direct probe of the transition-state for the dissociation reaction.

Laser-induced fluorescence proved a sensitive and extremely illuminating tool, in the Na-I dissociation experiment. Its general utility as a probe, however, and that of the closely related technique of transient absorbance is limited due to the lack of sensitivity for most large molecular systems. In larger molecules, where there is more than one bond to break, different dissociation products can often be distinguished by femtosecond single-photon or multiphoton ionisation followed by time-of-flight mass spectrometry.

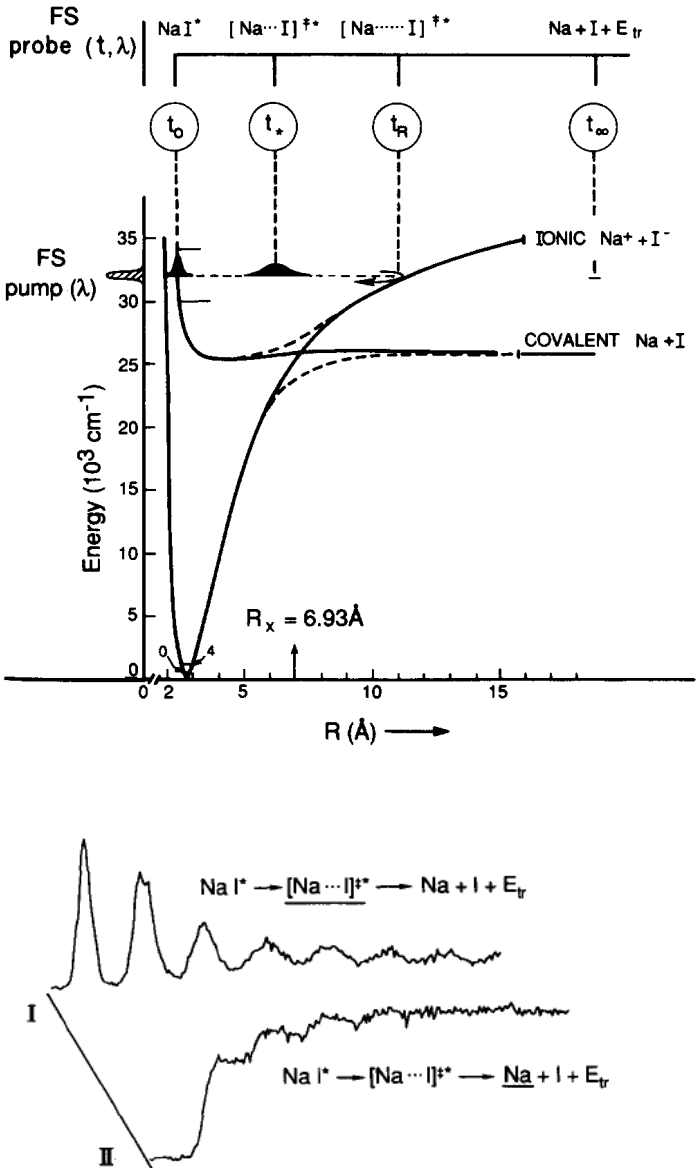

Figure 1.9 NaI potential energy curves (top) and LIF signal (bottom). The molecule is photoexcited to the upper potential energy curve and oscillates between the inner and outer turning points; at the avoided crossing there is a 10% probability the molecule will dissociate into neutral Na and I. The off resonance LIF wavelength probes the transition state (I), and the on resonance wavelength probes the dissociated Na atoms (II). Figure reprinted with permission from Figs. 1 and 2 in T. S. Rose, M. J. Rosker, and A. H. Zewail, Journal of Chemical Physics 88 (10), 6672 (1988). Copyright 1988, American Institute of Physics.

Time-resolved photoelectron spectroscopy

The methodology and application of time-resolved photoelectron spectroscopy (TRPES) has been reviewed, see for example Refs. 24-26. Photoexcitation of larger molecules leads to the population of a high density of vibronic (electronic and vibrational) levels that are coupled to many other electronic and vibrational states. This can be followed by radiationless decay to a lower state (IC or ISC) or by intramolecular vibrational redistribution (IVR). If the excited electronic state is well separated from all other electronic states, IVR will be the only possible relaxation path available.

Femtosecond time-resolved photoelectron spectroscopy has been exploited very successfully to observe ultrafast internal conversion in a number of polyatomic molecules. A classic example is S_2–S_1 IC in the linear polyene *all-trans* 2,4,6,8 decatetraene (DT).[27] The energy level scheme is presented in Fig. 1.10. The first optically allowed transition is to the S_2 (1^1B_u) state which is a singly excited configuration and correlates electronically with the D_0 (1^2B_g) ground electronic state of the cation. The S_1 (2^1A_g) state arises from a configuration interaction between singly and doubly excited configurations and correlates electronically with the D_1 (1^2A_u) first electronically excited state of the cation. In this experiment, a femtosecond pump laser is used to prepare the molecule in the vibrationless S_2 state. It then evolves into a vibrationally hot S_1 state by IC. A delayed femtosecond probe laser ionises the system and the photoelectron kinetic energy spectrum provides a measure of the S_1 and S_2 population.

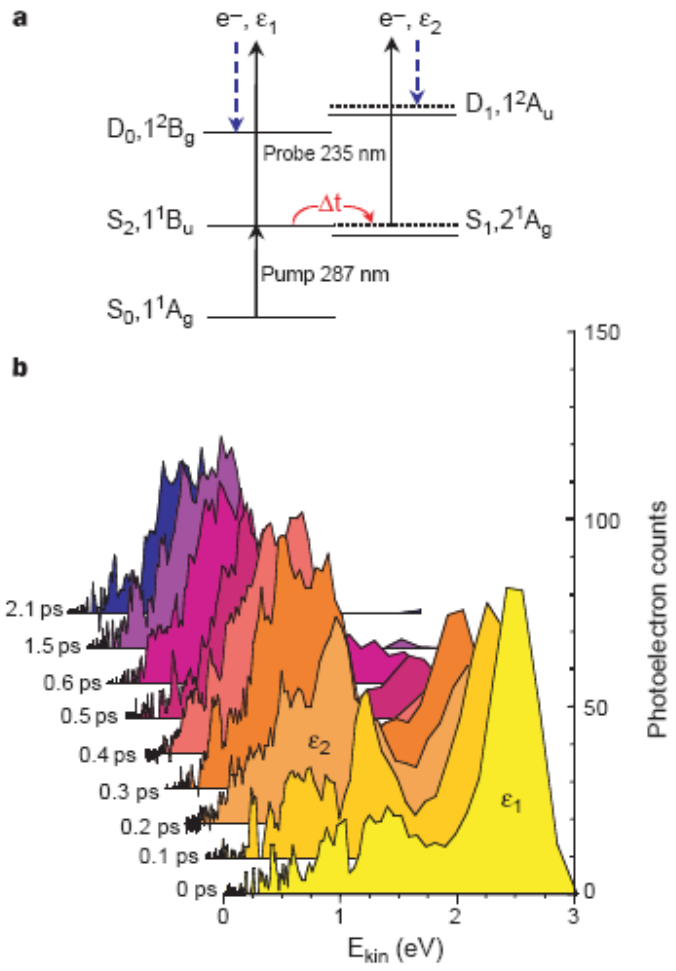

Figure 1.10 Pump-probe excitation scheme (a) and photoelectron kinetic energy as a function of delay (b) for *all-trans* 2,4,6,8 decatetraene. Internal conversion is observed through the change in kinetic energy of the photoelectrons from the ε_1 to ε_2 channel. Figure reprinted with permission from Macmillan Publishers Ltd: Nature, Fig. 2 in V. Blanchet, M. Z. Zgierski, T. Seideman *et al.*, Nature 401 (6748), 52 (1999), copyright 1999 http://www.nature.com/nature/index.html.

As a general guide for the unravelling of nonadiabatic dynamics in molecules using TRPES, Seel and Domcke categorised two general types of ionisation correlations.[28] Type I correlations are those in which two different electronic states involved in the crossing correlate with different cationic states, and Type II are those in which both of

the excited states correlate with the same cationic state. The correlation between the cation and the neutral is obtained from a Koopmans' theorem approximation in which the ionisation is assumed to be a single electron process, and the removal of a single electron from an orbital in the neutral results in a cation state with the same configuration. Type I and Type II ionisation correlation schemes are illustrated in Fig. 1.11.

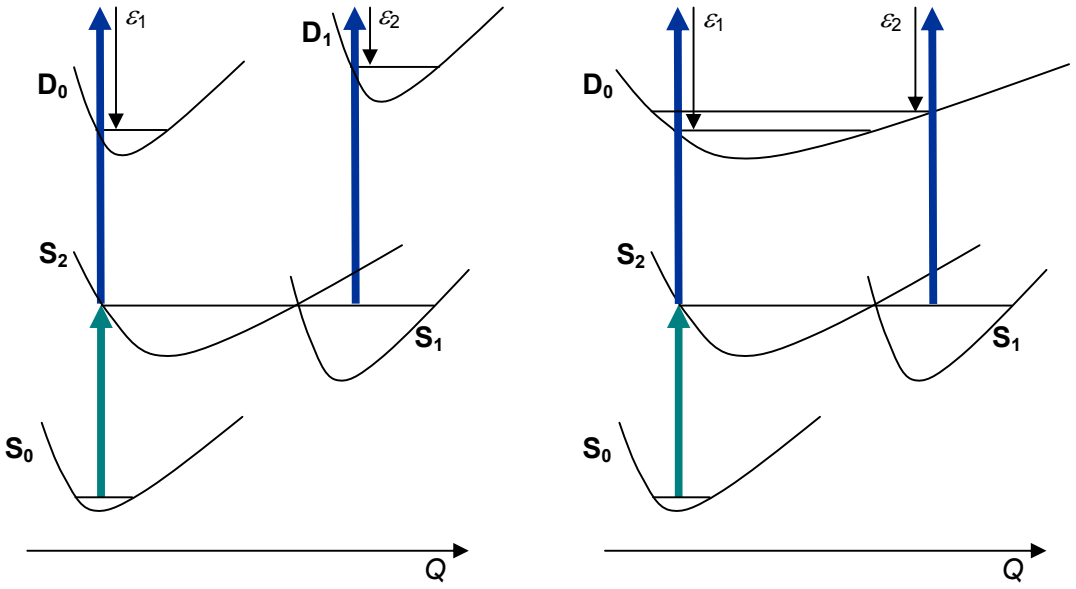

Figure 1.11 Schematic representation of Type I (left) and Type II (right) Koopmans' correlations in the time-resolved photoelectron spectroscopic observation of a non-adiabatic process. In Type I correlations, the two singlet excited states involved in the crossing, S_1 and S_2 correlate with two energetically distinct doublet cation states D_0 and D_1, and the resulting photoelectron bands, ε_1 and ε_2 are well separated. In the case of Type II correlation, the photoionisation of S_1 and S_2 is to the same ionic state D_0. For simplicity, a single nuclear coordinate, Q, is shown.

The decatetraene spectra illustrated in Fig. 1.10 above was interpreted as resulting from a Type I case, where the two different photoelectron bands resulting from two distinct ionisation pathways are clearly distinguished by their energies. In a Type II correlation system, although both the neutral excited states involved will ionise to the same species,

it may be possible to distinguish the ionisation *via* different intermediates by the different vibrational structure of the ionised species. The Franck-Condon rule dictates that the vibrational excitation is likely to be conserved on ionisation, and so if the excited state crosses to a lower electronic state and thereby increases its vibrational content, this should be mapped onto the ionised species as a lower energy photoelectron band. The implications of the two types of ionisation correlations have been discussed in more detail in the literature.[26]

Type I and Type II Koopmans' correlations are limiting cases, and in general the correlations in a photoionisation system may be more complex than either case. For example, more than one ionisation channel could be open to both the electronic states in a non-adiabatic crossing. However, the importance of knowledge of the ionisation correlations and energies for the interpretation of TRPES cannot be overestimated. In Chapter 4, this point is demonstrated by the analysis of time-resolved photoelectron spectra of styrene using the calculated cation state configurations and neutral-cation correlations that are reported in Chapter 3.

Time-resolved photoelectron spectroscopy (TRPES) has several key advantages over techniques such as LIF and time-resolved transient absorption, as discussed elsewhere.[25,29] TRPES can be used to probe any excited state, provided the ionising photon has sufficient energy, regardless of its optical activity. The changing photoelectron spectrum provides a picture of the excited state as it evolves. Imaging photoelectron spectrometers are now commonly used to record photoelectron energies, and these have the further advantage of allowing the measurement of angular momentum changes between the intermediate states. Indeed, femtosecond TRPEI (time-resolved photoelectron imaging) is now an established technique in its own right.[30] TRPES has also been combined with coincidence ion measurements to provide time-resolved molecular frame 3D dynamics of photodissociation reactions.[31] It has also been used to study intramolecular reactions such as tautomerisation.[32]

1.4 Coherent Control

In the broadest terms, coherent control can be described as the manipulation of molecular processes using the coherent properties of laser light. The first attempts to control molecular dynamics started soon after the invention of the laser, when its high intensity and narrow bandwidth were exploited to populate vibrational overtones in an effort to dissociate the bond associated with a specific vibrational mode. Unfortunately, these attempts failed because intramolecular vibrational energy redistribution occurred before the excitation energy reached the dissociation limit for the target bond. Today, laser control of molecular dynamics and chemical reactivity is a major research field, thanks to the development of ultrafast lasers.[33] Scientists working in many branches of chemistry and physics continue to push the boundaries of technical and theoretical expertise in order to attempt to achieve the long-cherished goal of harnessing the power of laser light to manipulate and understand chemical reactivity and dynamics.

Over the last two decades a number of coherent control schemes have been developed. Early methods were single-parameter schemes in which a single factor such as the phase difference between two laser frequencies,[34] or the time-difference between two pulses[35] was used to alter the favoured pathway for a reaction. In the frequency-domain, control over the population of a final quantum state is achieved by simultaneously accessing multiple independent excitation paths. The net excitation is a result of interference between the competing pathways, and manipulating the relative phases and amplitudes of these pathways changes the final state population, analogous to Young's double slit experiment. This methodology of coherent control was developed by Brumer and Shapiro.[36] Like the early mode-selective control attempts, Brumer-Shapiro coherent control theory does not require the use of ultrafast lasers. In this scheme, control is exerted over the population of a molecular eigenstate by manipulating phase differences between different pathways between the same final and initial states. Such a control scheme is very general, and can be applied to a variety of different multiphoton processes, such as stimulated Raman emission and two-photon absorption.

One of the first demonstrations of Brumer-Shapiro coherent control was carried out by the group of Robert Gordon.[34] In the experiment, they varied the phase of a three-photon versus a one-photon transition in HI to produce different ratios of HI^+ and I^+ reaction product channels. The difference in phase between the two transitions was created by passing the UV beam for the three-photon excitation and the VUV beam for the one-photon excitation through a hydrogen gas cell in which the two beam frequencies had differing refractive indices.

In the time-domain, the simplest control scheme employs pairs of optical pulses, as in a traditional pump-probe experiment, but instead of simply monitoring wave packet evolution, in some systems, controlling the timing of the probe pulse can select between two or more final states. This approach is a direct extension of the wave packet dynamics experiments such as the one described in Section 1.3. The related pump-dump approach was formalised by Tannor, Kosloff and Rice.[35] Their model is based on a ground state potential energy surface of a molecule *ABC* featuring a minimum separated from two product channels, say *AB* + *C* and *A* + *BC*, by saddle points. Above the ground state surface is an excited state surface with a minimum that is displaced from that of the ground state, and has rotated normal coordinates. The femtosecond pump pulse excites vertically from the ground state, forming a vibrational wave packet on the excited surface. The wave packet evolves on the excited state surface and at some later time is pumped back down to the ground state surface by the second 'dump' femtosecond pulse. If the wave packet on the excited surface takes the molecule to geometries corresponding to those in the product channels of the ground state, vertical transitions from these points will place the wave packet in a product channel of the ground state. The second laser pulse can be timed so that it causes de-excitation into a specific product channel. This control scheme is illustrated in Fig. 1.12.

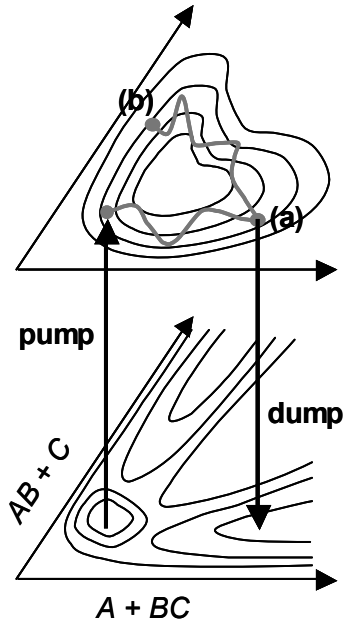

Figure 1.12 Schematic representation of pump-dump experiments. The pump-dump delay can be set to catch the wave packet at (a) or (b) to produce *A* + *BC* or *AB* + *C*, respectively.

The scheme illustrated by Fig.1.12 is valid for a very similar experiment in which the second photon pumps the wave packet to a more highly excited or even an ionic potential energy surface. The control exerted by the time delay between the two pulses in this type of experiment will be over the final eigenstates of the higher surface or the cation, respectively, in these cases. An early example of this type of control was carried out by Zewail to maximise the yield of XeI in the Xe + I_2 in a delayed two-photon absorption control scheme that was able to promote the reaction.[4] Time domain and frequency domain approaches to coherent control are in fact equivalent and in many ways overlap.[§] In the time domain picture, after the simple pump and timed-dump

[§] It has been shown that the Brumer-Shapiro and Tannor-Kosloff-Rice control mechanism are exactly equivalent.[37] An idea of this equivalence can be obtained by considering that in the Brumer-Shapiro frequency-domain mechanism, the combination of two or more laser fields in the absorption process necessarily produces some time dependence in the net laser field. There are a number of different ways to define coherent control (sometimes called 'phase control') and to classify coherent control experiments. For example, Dantus and co-workers classify linear intensity dependence control experiments separately from pump-dump control experiments[33]; some of the control mechanisms discussed forthwith in this chapter can be considered examples of the former type (see for example, the maximisation of the Na_2^+

experiment, the next step in complexity in a coherent control experiment involves changing the phase relationships between the eigenstates within a wave packet or changing the wave packet composition, and this can be achieved in a variety of ways.

Pulse trains

A train of two identical pulses can be created using a Michelson interferometer. The electric field in the time domain, $E(t)$ can be written,

$$E(t) = |E(t)|\exp[i\{\omega t - \phi(t)\}] + |E(t-t_0)|\exp[i\{\omega(t-t_0) - \phi(t-t_0)\}]. \qquad (1.20)$$

Identical pulse pairs may be used to carry out wave packet interferometry experiments. In such an experiment, two or more excited state wave packets are created and allowed to interfere with one another. A beautiful example of vibrational wave packet interferometry is an experiment performed by Stuart Rice, Graham Fleming and co-workers involving pairs of phase-locked vibrational wave packets in molecular iodine.[38] In these experiments, a first femtosecond pulse transfers population from the ground electronic state of the iodine molecule to the excited B-state creating a vibrational wave packet that evolves freely until the second femtosecond pulse transfers more population from the ground state of the iodine molecule to create a second, almost identical, vibrational wave packet in the excited state. When the two wave packets overlap spatially, they interfere and the interference is constructive or destructive, depending on the relative optical phase difference between the two femtosecond laser pulses, and on the time-dependent quantum mechanical phase difference between the two wave packets. The resultant interference dependent excited state population is then determined by measuring the total fluorescence signal from the excited state.

---

maximisation experiment by Gerber discussed on p. 45). However, both the linear intensity dependence control and pump-dump control experiments require specific phas(es) or delays of the ultrafast electric field puls(es) for the control mechanism to proceed. The delays between the ultrashort pulses in pump-dump experiments indicate the *molecular* phase dependence of the control mechanism; multiple pulse wave packet interferometry experiments (see p. 44) are slightly different in their control mechanism because when considered in the frequency domain, it can be shown that the time-delayed electric field replicas correspond to a frequency comb and therefore the control mechanism is not phase dependent.

Chirped pulses

As already discussed in Section 1.2, in a chirped laser pulse, the component frequencies are spread out in time, and the electric field can be written as,

$$E(t) = |E(t)| \exp\{i(\omega t - \phi'' t^2)\}. \quad (1.20)$$

A negatively chirped pulse (in which the instantaneous frequency *de*creases with time) can be used to step through the decreasing vibrational spacing in a diatomic molecule and thus enhance dissociation. Gustav Gerber and his co-workers have used chirped pulses to control the multiphoton ionisation of the sodium dimer, following from the experiments described in Section 1.3 and illustrated in Fig. 1.8. Negatively chirped ('down-chirped') pulses increased the population of the excited $2^1\Pi_g$ state, although the final Na_2^+ ($^2\Sigma_g^+$) ion population was enhanced by using a positively chirped ('up-chirped') pulse. The total excited $2^1\Pi_g$ state population is produced *via* a one-photon transition to the $A^1\Sigma_u^+$ state, upon which a wave packet motion is initiated. The difference in potentials between the $A^1\Sigma_u^+$ and $2^1\Pi_g$ states is such that the negatively chirped pulse is able to follow the outward motion of the $A^1\Sigma_u^+$ wave packet with the correct, decreasing, excitation energy for the second photon to excite to the next $2^1\Pi_g$, state. The mechanism by which the ion population is maximised with the positively chirped pulse is different. The Frank-Condon maxima for both of the two-photon transitions leading to the excited $2^1\Pi_g$ state correspond to redder parts of the pulse, so absorption of the redder parts of the positively chirped pulse allows the $2^1\Pi_g$ population to reach a maximum early with respect to the pulse duration. This means that the final ionising photon absorption is timed for the maximum in intensity of the same up-chirped pulse, and a maximum is seen in the ion yield as a result.[3]

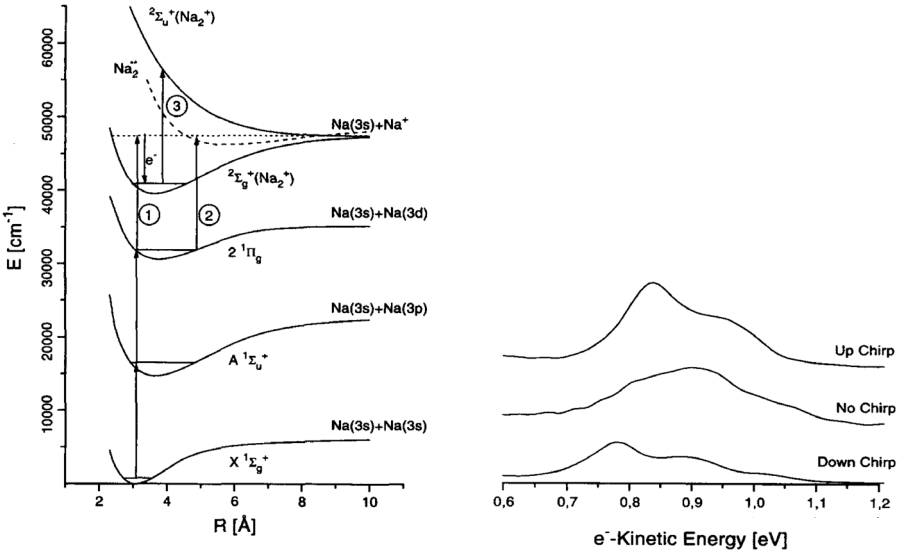

Figure 1.13 Potential energy curves for the Na_2 and Na_2^+ dimer with the possible processes that occur when Na_2 is irradiated with 618 nm fs radiation (left). Photon absorption *via* process 1 yields high energy photoelectrons (0.7-1.0 eV) and Na_2^+ ($^2\Sigma_g^+$). The measured photoelectron signal (right) shows that the up-chirped pulse yields significantly more of the Na_2^+ ($^2\Sigma_g^+$) product, because the redder part of the pulse is energetically more optimal for the first two one-photon absorption processes, and thus the population in the $^2\Pi_g$ state is maximised in time for maximum intensity of the laser pulse, producing a larger cation yield after ionisation by the third photon. Figure reprinted from Figs. 2 and 3 in A. Assion, T. Baumert, J. Helbing *et al.*, Chemical Physics Letters 259 (5-6), 488 (1996), with permission from Elsevier.

Programmable pulse shaping

Simple pulse shapes such as pulse trains and chirped pulses have proved valuable for coherent control experiments in small molecules. However, more complex pulse shapes are usually required to control the dynamics of larger molecules with more degrees of freedom. Commercially available pulse shaping instruments are now able to arbitrarily shape the phase and amplitude profiles of femtosecond laser pulses, allowing $\phi(t)$ and $|E(t)|$ to have almost any possible functional form. The most widely used commercial

pulse shaping devices are spatial light modulators (SLMs). An SLM is comprised of an array of liquid crystals whose birefringences can be modified individually using applied electric fields. Pulse shaping using SLMs requires the input pulse to be dispersed so that the different frequencies of the light can be addressed spatially by the SLM. The most common way of doing this is to place the SLM in the focal plane of a 4*f* zero-dispersion compressor. This is described in some detail in Chapter 2, where the design of an ultraviolet pulse shaping experiment is described.

With the incredible flexibility in phase and intensity profiles provided by SLM pulse shaping, the question arises – what is the best way to design a complex pulse to control the chemical products of a photochemical reaction? Optimal control theory, and other theoretical methods, have been developed to design *a priori* pulse shapes.[39] But the need for theory was cleverly circumvented by Judson and Rabitz who proposed using a learning algorithm in a closed loop within an experiment using the SLM variables as the optimisation parameters.[40] A basic genetic algorithm is outlined in Fig. 1.14. Since the conception of this experimental design, optimal control has been realized in a huge number of experiments including energy transfer processes in light harvesting bacteria[5] and *cis-trans* isomerisations.[6,7]

In most gas-phase femtochemistry experiments, laser beams are focussed at the intersection with a molecular beam, and for a typical 1 μJ, 100 fs pulse laser, with a wavelength centred at 250 nm, focused to a diameter of 50 μm by a 50 cm lens, the light intensity at the focus would be 10^{12} W cm^{-2}. Typically, multiphoton excitation and ionisation will occur when the intensity is $>>10^{13}$ W cm^{-2}, but just below this, in the perturbative regime, the electric field of the laser is weaker than the Coulomb electric field but is strong enough to perturb the electronic energy levels (the Stark effect). The first experimental demonstration of adaptive feedback control of photochemical dissociation, using automated pulse shaping and an evolutionary algorithm, was carried out using strong laser fields. Gustav Gerber and his co-workers employed intense shaped infrared laser pulses in a multiphoton ionisation scheme to control the branching

ratio of various photodissociation products of iron pentacarbonyl and dicarbonylchloro (η^5-cyclopentadienyl) iron.[8]

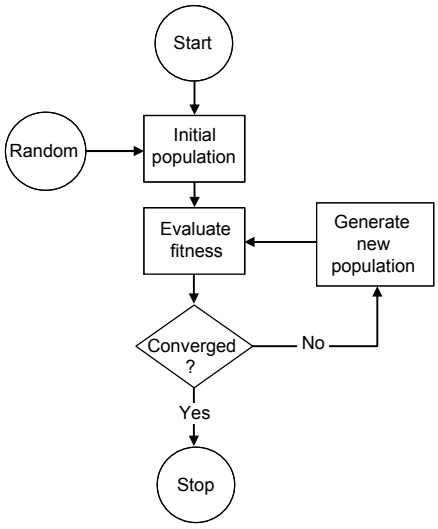

Figure 1.14 The outline of a genetic algorithm. Populations represent a set of initially random pulse shapes that will eventually converge to a single shape that is optimal for the target control process. Figure adapted from Ref. 41.

Unfortunately, it has generally proved difficult to unravel the control mechanisms from the rather complex pulse shapes obtained using these closed loop experiments. One of the exceptions is an experiment by Chantal Daniel and co-workers in which the photodissociation of the cyclopentadienyl (cp) manganese compound $cpMn(CO)_3$ was controlled. The authors of this study showed that the ratio of the parent ion yield to the daughter ion yield was increased using a two-colour multiphoton ionisation scheme analogous to their optimal control pulse: in the control pulse (centred at 800 nm) the first subpulse was bluer (~799 nm) and the second was redder (~800 nm). This suggested a two photon excitation followed by ionisation. The details of the excited state dynamics were then uncovered by electronic structure and quantum dynamics calculations on the excited potential energy surfaces of the molecule.

Strong field laser control is more flexible, in some ways, than weak field control, because a much larger number of states may be accessed due to Stark shifting of the field-free states. It is, however, less easy to model strong fields because of the difficulties in including all the competing processes such as ionisation and fragmentation that occur simultaneously the molecule. Progress has been made, however, and Levis and Rabitz have reviewed the field of closed-loop control with strong fields.[9]

An interesting example of a slightly different type of strong field femtosecond laser control is the creation of spatially aligned molecules. This technique can allow more precise dynamical information to be obtained from pump-probe experiment of, for example, femtosecond photodissociation.[42] Another example of a different molecular control technique involves using a non-resonant intense laser field that is not strong enough to dissociate or ionise the molecule, but instead controls a photochemical reaction by modifying the shapes of the potential energy surfaces involved in the photoreaction (the dynamic Stark effect). The non-resonant laser field effectively acts as a catalyst for the photochemical reaction. Albert Stolow and his colleagues employed such an approach to control the ratio of spin-orbit states of Br atoms produced during the photodissociation of IBr by using the strong non-resonant field to lower the adiabatic barrier at an avoided crossing on the excited potential energy surface.[43]

1.5 Summary

This chapter has set the scene for the projects that are described in Chapters 2, 3 and 4. In Chapter 2, the design of an ultraviolet pulse shaper and characterisation is described. The pulse shaper is suitable for use in a coherent control experiment similar to the optimal control experiments described in the previous section. The hope is, however, that the UV pulse shaper will be used in a slightly different control experiment: one in which the dynamics of an electronically excited molecule are steered towards or away from a certain target on the potential energy surface. Such a pathway to an excited state

target could be devised from knowledge of a theoretical reaction pathway, or from a detailed experimental knowledge of the time resolved dynamics of the photoexcited molecule. Chapters 3 and 4 are, respectively, theoretical and experimental studies that lay the groundwork for the development of models of the photophysics of the styrene molecule. Using knowledge of the photophysical and photochemical pathways in styrene, a photodynamic control mechanism might be designed, and this could be experimentally tested using the UV pulse shaper.

References

1 H. H. Fielding and A. D. G. Nunn, *Femtochemistry and the control of chemical reactivity*, in *Tutorials in molecular reaction dynamics,* edited by M. Brouard and C. Vallance (RSC, to be published 2010).

2 A. H. Zewail, in *Nobel Lectures, Chemistry 1996-2000*, edited by I Grenthe (World Scientific Co., Singapore, 2003).

3 A. Assion, T. Baumert, J. Helbing *et al.*, Chemical Physics Letters 259 (5-6), 488 (1996).

4 E. D. Potter, J. L. Herek, S. Pedersen *et al.*, Nature 355 (6355), 66 (1992).

5 J. L. Herek, W. Wohlleben, R. J. Cogdell *et al.*, Nature 417 (6888), 533 (2002).

6 G. Vogt, G. Krampert, P. Niklaus *et al.*, Physical Review Letters 94 (6) (2005).

7 V. I. Prokhorenko, A. M. Nagy, S. A. Waschuk *et al.*, Science 313 (5791), 1257 (2006).

8 A. Assion, T. Baumert, M. Bergt *et al.*, Science 282 (5390), 919 (1998).

9 R. J. Levis and H. A. Rabitz, Journal of Physical Chemistry A 106 (27), 6427 (2002).

10 M. Kasha, Discussions of the Faraday Society (9), 14 (1950).

11 C. J. Cramer, *Essentials of Computational Chemistry*, 2nd Edition ed. (Wiley, 2004).

12 J. Michl and V. Bonacic-Koutecky, *Electronic aspects of organic photochemistry*. (Wiley, 1990).

13 F. Bernardi, M. Olivucci, and M. A. Robb, Chemical Society Reviews 25 (5), 321 (1996).

14 M. Garavelli, Theoretical Chemistry Accounts 116 (1-3), 87 (2006).

15 N. Karasawa, K. Tada, and H. Ohmori, IEEE Photonics Technology Letters 19 (17-20), 1292 (2007).

16 Newport Corporation, The effect of Dispersion on Ultrashort Pulses, available at (http://www.newport.com/The-Effect-of-Dispersion-on-Ultrashort-Pulses/602091/1033/catalog.aspx).

17 R Trebino, *The musical score, the fundamental theorem of algebra, and the measurements of the shortest events ever created, FROG colloqium talk* (2006).

18 A. H. Zewail, *Femtochemistry—Ultrafast Dynamics of the Chemical Bond, Vols. I and II*. (World Scientific, New Jersey, Singapore, 1994).

19 G. Porter, in *Nobel Lectures, Chemistry 1963-1970* (Elsevier Publishing Company, Amsterdam, 1972).

20 R. G. W. Norrish, in *Nobel Lectures, Chemistry 1963-1970* (Elsevier Publishing Company, Amsterdam, 1972).

21 M. Dantus, M. J. Rosker, and A. H. Zewail, Journal of Chemical Physics 87 (4), 2395 (1987).

22 T. Baumert, M. Grosser, R. Thalweiser *et al.*, Physical Review Letters 67 (27), 3753 (1991).

23 T. S. Rose, M. J. Rosker, and A. H. Zewail, Journal of Chemical Physics 88 (10), 6672 (1988).

24 A. Stolow, A. E. Bragg, and D. M. Neumark, Chemical Reviews 104 (4), 1719 (2004).

25 A. Stolow, International Reviews in Physical Chemistry 22 (2), 377 (2003).

26 A. Stolow and J. G. Underwood, Advances in Chemical Physics, Vol 139 139, 497 (2008).

27 V. Blanchet, M. Z. Zgierski, T. Seideman *et al.*, Nature 401 (6748), 52 (1999).

28 M. Seel and W. Domcke, Chemical Physics 151 (1), 59 (1991); M. Seel and W. Domcke, Journal of Chemical Physics 95 (11), 7806 (1991).

29 A. Stolow, Annual Review of Physical Chemistry 54, 89 (2003).

30 T. Suzuki, Annual Review of Physical Chemistry 57, 555 (2006).

31 O. Gessner, A. M. D. Lee, J. P. Shaffer *et al.*, Science 311 (5758), 219 (2006).

32 S. Lochbrunner, T. Schultz, M. Schmitt *et al.*, Journal of Chemical Physics 114 (6), 2519 (2001).

33 M. Dantus and V. V. Lozovoy, Chemical Reviews 104 (4), 1813 (2004).

34 L. C. Zhu, V. Kleiman, X. N. Li *et al.*, Science 270 (5233), 77 (1995).

35 D. J. Tannor, R. Kosloff, and S. A. Rice, Journal of Chemical Physics 85 (10), 5805 (1986).

36 M. Shapiro and P. Brumer, Journal of Chemical Physics 84 (7), 4103 (1986).

37 M. Shapiro and P. Brumer, Journal of Chemical Physics 84 (1), 540 (1986).

38 N. F. Scherer, R. J. Carlson, A. Matro *et al.*, Journal of Chemical Physics 95 (3), 1487 (1991).

39 R. Chakrabarti and H. Rabitz, International Reviews in Physical Chemistry 26, 671 (2007).

40 R. S. Judson and H. Rabitz, Physical Review Letters 68 (10), 1500 (1992).

41 R. E. Carley, University of London, 2005.

42 J. G. Underwood, M. Spanner, M. Y. Ivanov *et al.*, Physical Review Letters 90 (22) (2003).

43 B. J. Sussman, D. Townsend, M. Y. Ivanov *et al.*, Science 314 (5797), 278 (2006).

Chapter 2

Femtosecond pulse shaping and characterisation in the ultraviolet

One of the central aims of this thesis was to use a pre-designed pulse shape for control of molecular dynamics, necessitating the shaping and measurement of femtosecond pulses at a wavelength in the deep ultraviolet. Specifically, the pulse shaper and characterisation scheme were designed so that they might be used in an experiment in which the optimisation goal is the maximisation of one of the photochemical paths from S_1 benzene, for which a central wavelength of 254 nm is necessary. Although a pre-designed pulse may have fairly simple structure, it was for the possibility of *arbitrary* pulse shaping in an optimal control experiment with a genetic algorithm (see Chapter 1, Section 1.4) that the pulse shaping method reported in this chapter was selected. The characterisation scheme needed to be able to measure the shape of *any* possible pulse that could be produced, in order to demonstrate the effectiveness of the shaping method and so that the measured shape might be analysed in terms of its possible photochemical activity. This chapter starts with an introduction to the generation, manipulation and characterisation of ultrafast laser pulses (Section 2.1). There follows a description of how ultrashort pulses were generated using commercial systems for UV pulse shaping and spectroscopy experiments (Section 2.2), which applies to the lasers used in experiments described in this chapter and those in Chapter 4. The design of the UV pulse shaping and characterisation experiment is described, with emphasis on the selection of an appropriate pulse characterisation scheme (Section 2.3). The final working design is summarised (Section 2.4), and some results from its testing are presented (Section 2.5). Finally, some possible future applications of the UV pulse shaping of the experiment for controlling photochemistry chemistry are outlined (Section 2.6). Parts of the work reported in this chapter were carried out in collaboration with Dorian Parker, and have already been reported in a research publication[1]; other sections of this chapter form part of a chapter in a book.[2]

2.1 An introduction to ultrafast lasers

Femtosecond laser light generation

Femtosecond laser technology is a research field in itself and there are many excellent reviews available, see for example Ref. 3. A laser cavity in its simplest form consists of a gain medium, and one mirror at each end of the cavity. The medium is 'pumped' in order to achieve a population inversion, *i.e.* an upper level is populated more than the ground state. Photons emitted by spontaneous emission then stimulate the emission of further photons – hence the word 'laser' which is an acronym for 'Light Amplification by Stimulated Emission of Radiation'. One of the cavity mirrors has a reflectivity <100% allowing radiation to leave the cavity. A cavity supports light frequencies, ν, for which the length of the cavity is an integer or half integer number of wavelengths; these frequencies span the cavity length by starting and ending with a node. They are called the longitudinal modes of the cavity, $\nu = nc/2L$, where L is the cavity length, c is the speed of light, and n is an integer. The number of longitudinal modes that exist in the laser cavity is determined by the spectral bandwidth of the laser transition.

To obtain femtosecond laser pulses, the different longitudinal modes that propagate in the laser cavity must be mode-locked so that they oscillate in phase with one another. If many modes are allowed to co-exist in the cavity and all their phases are aligned at one point, the result is a very small region of constructive interference that lasts for a few femtoseconds; the more modes there are, the shorter the resulting pulse, in accordance with the energy-time uncertainty principle. This principle may be used to determine the precise limiting value for the product of the spectral width, $\Delta\nu$, and time duration, Δt, known as the time-bandwidth product (TBWP). For a pulse with a Gaussian distribution of modes and Gaussian temporal intensity distribution, Eq. 1.6 becomes

$$\Delta\nu\Delta t \geq 0.441, \tag{2.2}$$

where the minimum time-bandwidth product is 0.441, if $\Delta\nu$ and Δt are defined as the full-widths at half maximum (FWHM). A Gaussian pulse is the most commonly modelled pulse shape produced by femtosecond oscillators. Ti-sapphire (titanium-doped

sapphire, Ti^{3+}:Al_2O_3) lasers are the most common laboratory femtosecond lasers and can have spectral bandwidths of around 150 nm (centred at 780 nm) that can support pulse durations ≥ 6 fs, which is the limit for a single cycle pulse in the near IR.

Mode-locking in a Ti-sapphire laser exploits the optical Kerr effect within the gain medium. The optical Kerr effect is the change in the refractive index of a medium induced by an intense incident electric field. The refractive index of the medium is $n = n_0 + n_2 I$, where n_0 is the linear refractive index, n_2 is the nonlinear refractive index, and I is the laser intensity; in Ti-sapphire at 800 nm, $n_0 = 1.76$ and $n_2 = 3.1 \times 10^{-16}$ cm^2 W^{-1}. The phase delay experienced by the propagating optical pulse is proportional to the refractive index,

$$\phi(\omega) = n(\omega)\omega L/c\,, \tag{2.3}$$

where ω is the angular frequency, $n(\omega)$ is the frequency-dependent refractive index, L is the length of the material and c is the speed of light in a vacuum. The spatial dependence of the intensity of the laser pulse, $I(x)$, induces a spatial dependence to the refractive index, $n(x) = n_0 + n_2 I(x)$, which produces a space-dependent phase delay,

$$\Delta\phi(x) = n_2 I(x)\omega L/c\,. \tag{2.4}$$

Most lasers, femtosecond or otherwise, produce beams with a Gaussian spatial intensity profile. The Gaussian beam experiences a variation in refractive index that is equivalent to a positive lens, which results in self-focussing of the laser pulse. Self-focussing provides the mechanism for mode-locking in femtosecond lasers. Placing an aperture around the waist of the focused beam in the laser cavity discriminates against unfocused continuous-wave (CW) laser light. Kerr-lens mode-locking does not happen spontaneously – it is usually initiated by vibrating one of the laser cavity mirrors to introduce a noise spike into the intensity profile of the radiation in the cavity, to trigger an intense pulse of photons. The shorter more intense pulses then induce a larger change in refractive index and are more strongly self-focussed than the low intensity CW light, and the stimulated emission becomes dominated by the short pulses with the aid of the aperture at the beam waist.

In the temporal domain, there is another consequence of the Kerr effect that is analogous to self-focusing. Equation 2.4 may re-written to describe the temporal variation in phase due to the, normally Gaussian, variation in temporal intensity, $I(t)$:

$$\Delta\phi(t) = n_2 I(t)\omega L/c \tag{2.5}$$

For a pulse propagating in an optical medium of length L, the accumulated phase results in instantaneous frequency (defined in Eq. 1.16) shifts,

$$\Delta\omega(t) = -n_2 \frac{dI(t)}{dt}\omega L/c\,, \tag{2.6}$$

whose sign depends on the slope of the Gaussian intensity profile and so give rise to new frequency components, redder and bluer at longer and shorter times respectively. This broadens the spectrum and therefore reduces the pulse duration, Δt. This phenomenon is called self-phase modulation (SPM) and is important in some femtosecond laser oscillators as a means of reducing the pulse duration.

As already stated, generally, the spatial profile of a laser pulse is Gaussian as a function of its transverse radial distance. Within this model, estimations of the beam waist and intensity at the focus of a lens can be obtained.[4] Determining the beam intensity is crucial for the interaction region of a spectroscopic experiment, so that an estimate of whether or not perturbative effects on the molecules are likely to occur.

Frequency conversion of a femtosecond oscillator from the standard, typically near IR, wavelength using nonlinear techniques is usually carried out after the output pulse energy has been amplified. Avoidance of self-phase modulation (Eq. 2.6) is an important consideration in high power <100 fs amplifiers. In order to amplify the short pulse without significant distortion of the phase, chirped pulse amplification is necessary. Using chirped pulse and regenerative amplifier technology it is possible to provide pulse energies of a few mJ at kHz repetition rates, corresponding to peak intensities in the TW cm^{-2} (1 TW = 10^{12} W) range.

Wavelength tuning of femtosecond pulses - non-linear optics

Non-linear optics plays a very important role in ultrafast optics. The polarisation response of materials to light is usually linear, but where the light is more intense, the material might fail to respond linearly, and there will be a distortion in the polarisation oscillation, corresponding to higher harmonics in the spectrum of the oscillation. The polarisation is given by

$$\mathbf{P} = \varepsilon_0 \left\{ \chi^{(1)}\mathbf{E} + \chi^{(2)}\mathbf{E}^2 + \chi^{(3)}\mathbf{E}^3 + \cdots \right\}, \tag{2.1}$$

where ε_0 is the permittivity of free space, and $\chi^{(i)}$, with i = 1,2,3…, the electric susceptibilities. For low light intensities, **P** is linear in the electric field **E**, whereas the higher order non-linear contributions become important with increasing intensity.

The optical Kerr effect, which has already been discussed, is an example of a third order nonlinearity. The second order nonlinearity, $\chi^{(2)}$, of non-centrosymmetric crystal materials is exploited in optical parametric amplifiers (OPAs). Signal beam photons, ω_s, and higher energy pump beam photons, ω_p, are combined in a nonlinear crystal where the pump photons are converted into an equal number of photons at the original pump frequency and at a new lower frequency called the idler frequency, ω_i. Thus energy is conserved and $\omega_p = \omega_s + \omega_i$. The signal and idler frequencies are determined by phase matching constraints $\mathbf{k}_p = \mathbf{k}_s + \mathbf{k}_i$, and can be tuned by rotating the optical axis of the crystal. These signal and idler frequencies then undergo further nonlinear optical mixing with the intense pump beam, followed by other $\chi^{(2)}$ processes: second-harmonic generation (SHG), third-harmonic generation (THG), or fourth-harmonic generation (FHG), to generate tuneable femtosecond pulses across the visible and ultraviolet regions of the spectrum. Three-wave non-linear processes (second-order non-linearities) can be divided into different types of processes, depending on the orientations of the polarising light fields. In Type I SHG, the two fundamental frequency photons have the same polarisations, and the resultant second harmonic is polarised perpendicular to the fundamental. In Type II SHG, the two fundamentals are mutually perpendicular, and the polarisation of the second harmonic is parallel to one of

them. The efficiency of all the types of non-linear processes depends on the birefringence properties of the crystal involved.

2.2 An ultrafast laser system for UV pulse shaping, spectroscopy and control

The femtosecond laser system consists of an oscillator, a chirped pulse regenerative amplifier, two optical parametric amplifiers and third and fourth harmonic generation boxes, as outlined in Fig. 2.1 below.

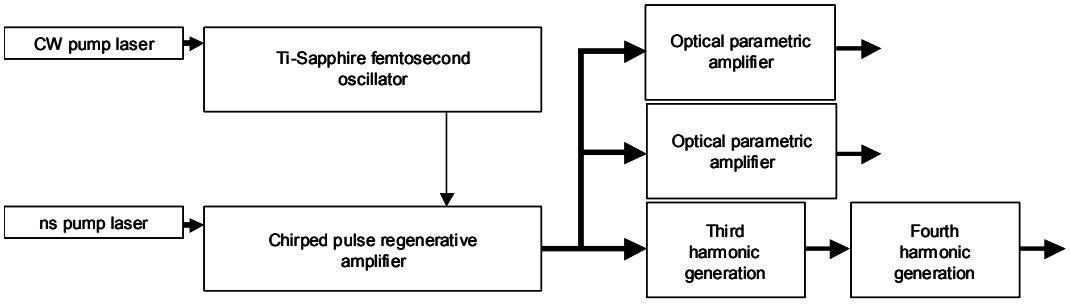

Figure 2.1 Block diagram for the femtosecond laser system. Femtosecond pulses at 785 nm, with power approximately 500 mW, are generated in the Ti-sapphire oscillator by Kerr-lens mode-locking; these are amplified by stretching, regenerative amplification, and then compression in the amplifier to a central wavelength of 795 nm and pulse energy of about 2.5 mJ. Wavelength conversion occurs in the optical parametric amplifier (OPA) to give pulses in the visible, UV or IR, or in the third and fourth harmonic generation boxes. Both the oscillator and amplifier are pumped by high power lasers.

Oscillator

The femtosecond pulse is generated in the Ti-sapphire oscillator. A diagram of the oscillator layout is given in Fig. 2.2. The Ti-sapphire crystal is pumped by a CW laser at 532 nm (Coherent Verdi). The lasing transition is optimal at 785 nm, and the cavity is bounded by the output coupler, M0/M1, (see Fig. 2.2) and the end mirror, M7; the

external cavity beam path *via* M8 and M9 is used during alignment only, to set the length of the cavity path with the mirrors M0/M1, M2, M3, M4, M5. After lasing is generated in the Ti-sapphire crystal, the prism pair BP1 and BP2 can be used to select the right amount of chirp compensation to mode-lock the pulse using the starter. A detector is used to send a time signal from the output pulses to the electronics box that controls the chirped pulse regenerative amplifier.

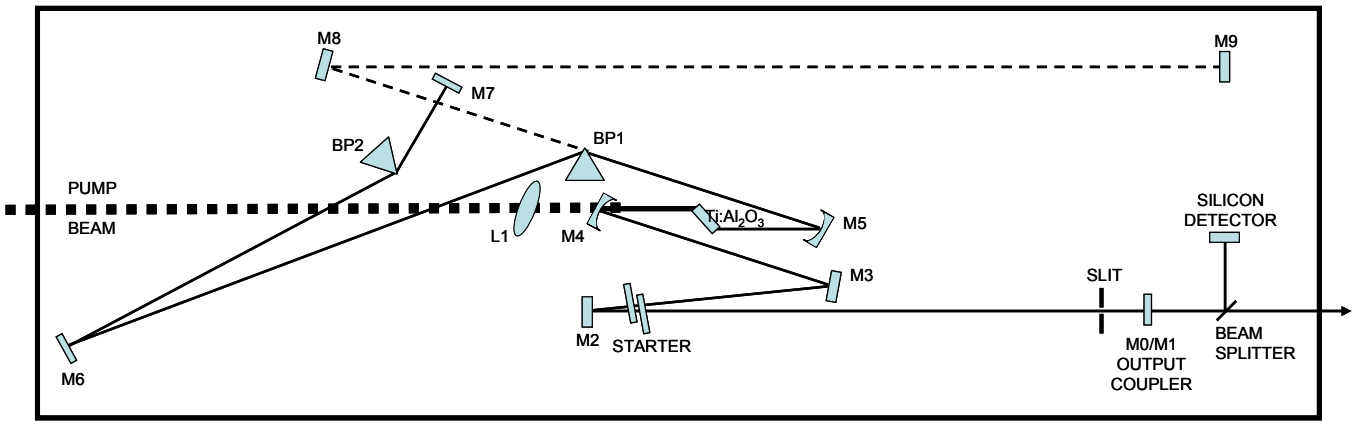

Figure 2.2 Ti-sapphire femtosecond oscillator (Coherent MIRA). Mirrors are labelled M0-M9, Brewster prisms are BP1 and BP2, L1 is a focussing lens, and Ti:Al_2O_3 is the Titanium-sapphire crystal. The pump beam (532 nm CW Verdi laser by Coherent) enters the cavity via L1, passing through M4, to reach the Ti:Al_2O_3 crystal where the laser emission at 785 nm occurs. The laser cavity is bounded by the mirror M7 and the partially reflecting mirror M0/M1. The prism pair BP1 and BP2 allow control of the chirp of the pulse. The starter introduces noise into the cavity to trigger the Kerr-lens mode-locking of the laser. The path defined by the dashed line is used for alignment purposes only, and is not part of the mode-locked beam path.

Chirped pulse regenerative amplifier

The approximately 500 mW 60 kHz frequency beam of pulses from the oscillator is injected into the amplifier (Coherent Legend) to coincide with the nanosecond pulse pump laser (solid-state, Q-switched, nanosecond Nd:YLF laser Coherent Evolution). The femtosecond seed first enters a stretcher. The stretcher comprises a diffraction grating and gold-coated mirror that are aligned to introduce a positive chirp to the laser

pulses. This lengthens the pulses temporally, reducing the peak power. These chirped pulses are then injected into the regenerative amplifier cavity by an optical switch, usually a Pockels cell, which is a voltage controlled waveplate, or Pockels cell and quarter waveplate combination to rotate the polarisation of the light. The optical switch is on for about 1 ns, allowing just one of the femtosecond pulses to pass through it, to or from the cavity. The active medium in the regenerative amplifier is another Ti-sapphire crystal that is pumped by the nanosecond laser. The chirped pulses make many round trips in the cavity before a second optical switch ejects the pulse into a compressor. In the compressor another diffraction grating and mirror set are aligned to introduce a negative chirp to compensate for the positive chirp introduced by the stretcher and to compensate for higher order phase errors introduced by the amplification process itself. The chirped pulse regenerative amplifier is shown in Fig. 2.3.

Wavelength tuning the amplified femtosecond pulses: OPAs and FHG

The amplified femtosecond pulse beam is converted to UV and visible wavelengths using a variety of non-linear three-wave mixing processes. Tuneable pulses are generated by OPAs (Coherent OperA) in the visible and UV regions of the spectrum in the visible, UV (up to 235 nm) and near IR (see Fig. 2.4). To obtain light at around 200 nm, the fourth harmonic of the amplified beam can be generated using the third-harmonic and fourth-harmonic boxes (custom-built by Coherent) as illustrated in Fig. 2.5.

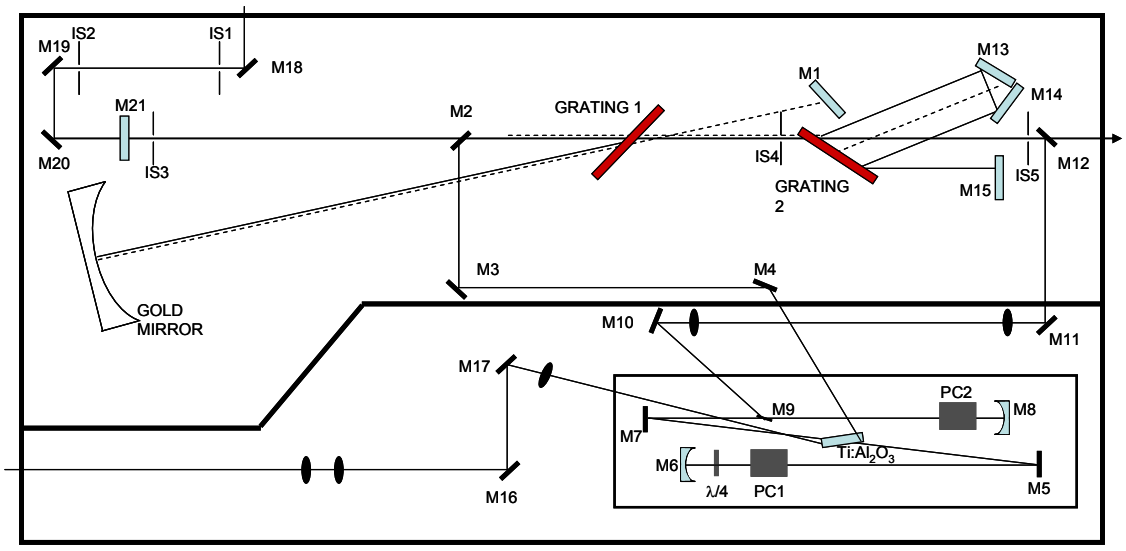

Figure 2.3 Chirped pulse regenerative amplifier (Coherent Legend). Mirrors are labelled M1-M21, Irises are IS1-IS5, Pockels cells are PC1 and PC2, the Titanium-saphire crystal is Ti:Al_2O_3 and the quarter waveplate is λ/4. The output of the femtosecond oscillator first enters a stretcher via M18, M19 and M20. The stretcher comprises a diffraction grating (Grating 1) and gold-coated mirror (Gold mirror), and mirror M1 that are aligned to introduce a positive chirp to the laser pulses. This lengthens the pulses temporally, reducing the peak power. These chirped pulses are then injected via M2 and M3 into the regenerative amplifier cavity (bounded by M6 and M8) by an optical switch, a Pockels cell (PC1) and quarter waveplate (λ/4) combination, to rotate the polarisation of the light. The optical switch is on for about 1 ns, allowing just one of the femtosecond pulses to pass through it into the cavity to the Brewster window at the crystal, which can selectively transmit the pulse depending on its polarisation. The active medium in the regenerative amplifier is another Ti-sapphire crystal that is usually pumped by a solid-state, Q-switched, Nd:YLF laser that enters the cavity via M16 and M17. The chirped pulses make many round trips in the cavity before a second optical switch (PC2) ejects the pulse into a compressor via M9, M10, M11 and M12. In the compressor, another diffraction grating (Grating 2) and mirror set (M13, M14 and M15) are aligned to introduce a negative chirp to compensate for the positive chirp introduced by the stretcher and, importantly, to compensate for higher order phase errors introduced by the amplification process itself.

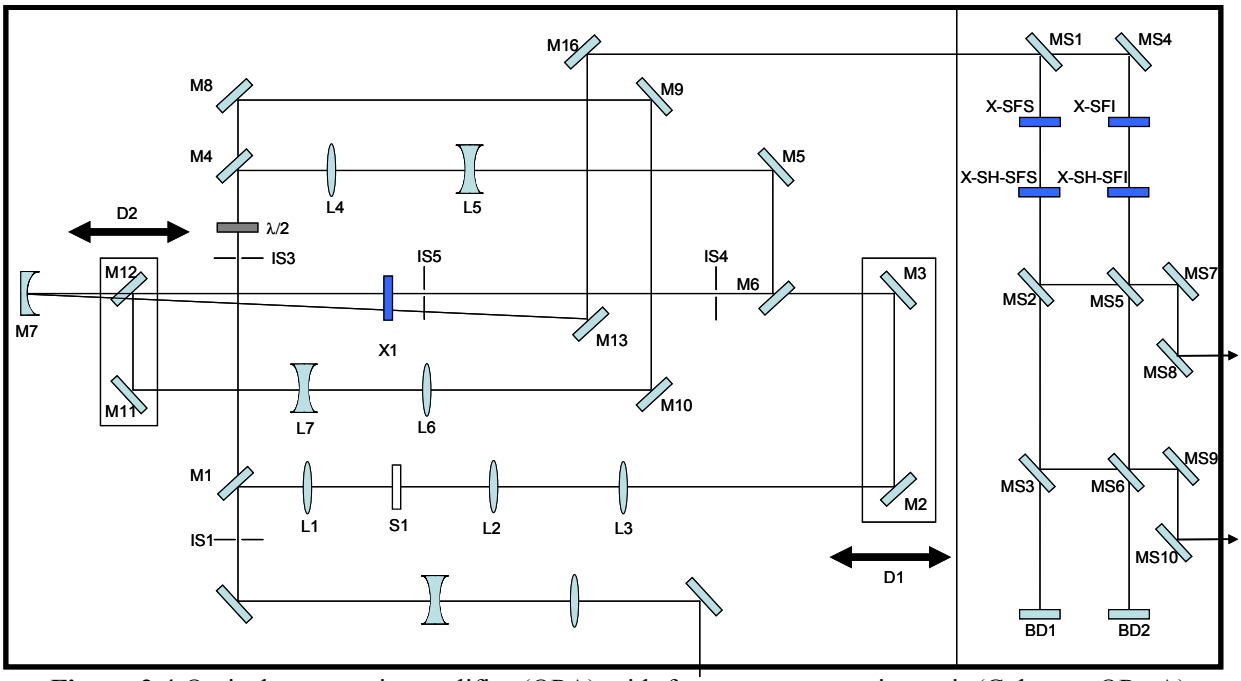

Figure 2.4 Optical parametric amplifier (OPA) with frequency conversion unit (Coherent OPerA). Mirrors are labelled M1-M16 and MS1-MS16, a ½-waveplate is labelled λ/2, beam-dumps are BD1 and BD2, Irises are IS1-IS4, lenses are L1-L4, and the nonlinear crystals are X-1 (OPG/OPA), X-SFS (sum-frequency of the OPG signal), X-SFI (sum-frequency of the OPG idler), X-SH-SFS (second harmonic of the sum-frequency of the OPG signal), X-SH-SFI (second harmonic of the sum-frequency of the OPG idler). The beam enters the OPA and is collimated before white light is generated in the quartz crystal labelled S1. The delay stage D1 allows the temporal position of the white light pulse to be fine-tuned with respect to the fundamental pulse with which it recombines on M6 before the OPA crystal X1 to create the optical parametric amplification (OPA) signal in the infrared. OPA is a nonlinear three-wave mixing phenomenon, and here the input infrared signal photons from the white light are combined with the pump beam (795 nm, *via* transmission through M1, then *via* M4, M5 and M6) in the OPA crystal where the pump photons are converted into more signal photons, as well as idler photons. Signal wavelength flexibility is possible by mixing the fundamental in X1 with any section of the broad bandwidth of white light. Selective mixing is achieved by phase matching *via* angle tuning the crystal. The OPA signal after X1 is reflected from M7 and then combined on M12 with another part of the fundamental beam and passed back through X1 in another stage of amplification of the OPA signal. The delay between the amplifier fundamental and the OPA signal is optimised using the delay D2. If a different wavelength range is desired, the OPA idler may be optimised instead of the signal. The amplified OPA signal (or idler) leaves the OPA *via* M13 and M16 and enters the frequency conversion unit where wavelengths in the visible and UV are created by sum-frequency mixing with the fundamental and/or second harmonic generation of the resulting signal.

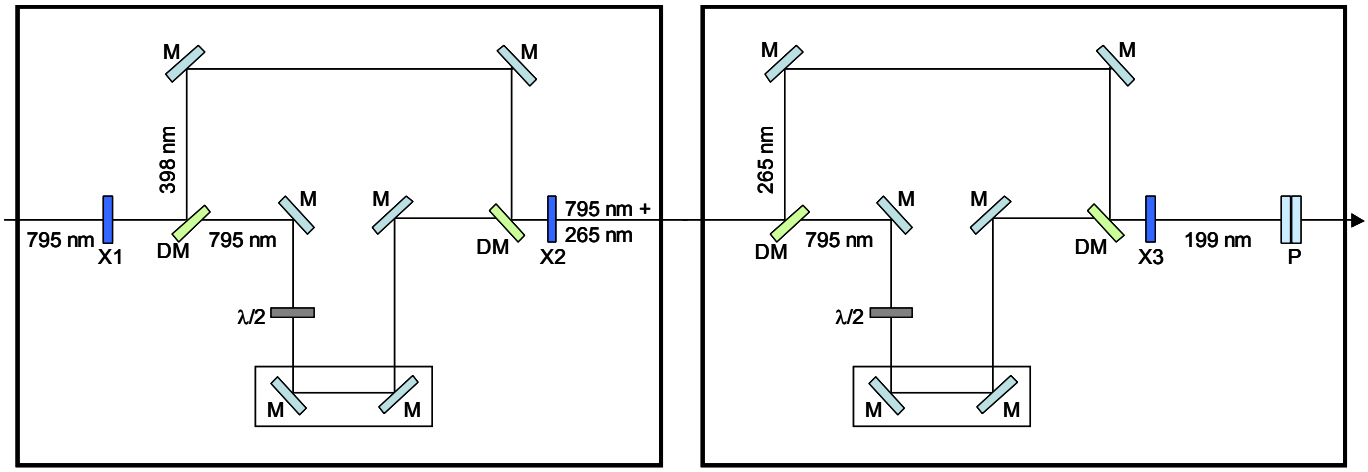

Figure 2.5 Third and fourth harmonic generation (Coherent THG and FHG) boxes. Mirrors are labelled M, dichroic mirrors are DM, crystals are X1-X3, half-waveplates are λ/2, and the P is a polariser. Approximately 0.6 mJ pulses from the amplifier are sent into the THG box. The beam is frequency doubled in the crystal X1 by second harmonic generation and the resulting beam is split into the fundamental and second harmonic by a dichroic mirror (DM). The fundamental is rotated by a ½ waveplate, and then the two beams are recombined on another dichroic mirror for sum-frequency mixing in the crystal X2 to get the third harmonic. The fundamental beam has an adjustable length so that the overlap in X2 may be optimised. The THG mixed with the fundamental is sent into the FHG box where the fourth harmonic is generated in a similar arrangement.

Pulse characterisation

Monitoring the quality of the output from these commercial laser systems was carried out in a variety of ways. The output beam from the amplifier may be monitored by a single-shot autocorrelator (Coherent SSA). The autocorrelation measurement gives an indication of the beam duration and quality, which can be used as feedback for alignment. As detailed in the section following this one, a part of the amplified beam was completely characterised using a commercial instrument as a reference for the pulse shaping experiment. The output from the OPA can be measured using autocorrelation or cross-correlation with a commercial autocorrelator or cross-correlator (both made by Coherent). For spectroscopic experiments, a more accurate measurement of the pump-

probe cross-correlation can be obtained by an *in situ* measurement in the molecular beam (see Chapter 4, Section 4.3). Visible light from the OPAs was used in the pulse shaping experiment described in the rest of this chapter. UV light from the OPAs and from the FHG box have been used in the time-resolved photoelectron imaging experiments described in Chapter 4.

2.3 Pulse shaping for a coherent control experiment

The general term for the manipulation of the phase of ultrashort pulses is "pulse shaping" and includes the alteration of the temporal positions of the frequencies and/or selectively reducing the intensities of the frequency components of the pulse. Systematic pulse shaping is usually achieved in a purpose built setup outside the laser cavity in a 4*f* optical arrangement using a commercial instrument called a spatial light modulator (SLM), set at the focal plane of the setup (see Fig. 2.6), where the bandwidth of the pulse is spatially dispersed transverse to the propagation direction of the light. The SLM is a pixelated array of liquid crystals aligned across the focal plane that act as variable retardance waveplates, such that each pixel is able to address a finite (small) range of frequencies and arbitrarily change its temporal position (or relative phase). If a dual array of SLMs is used, the intensity of the frequencies can also be altered, independently of the phase manipulation.

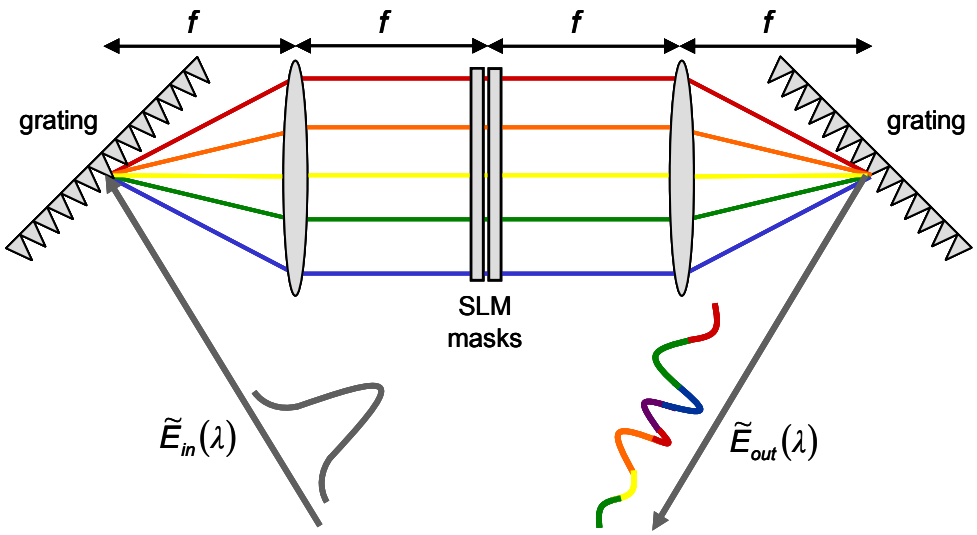

Figure 2.6 Schematic diagram of a 4*f* pulse shaper. The input, flat phase, light field is dispersed on a grating and then collimated after a distance, *f*, on a lens of focal length, *f*. After another distance *f*, the dispersion is collimated and the individual frequencies are simultaneously focussed the Fourier plane, where the dual masks of the SLM alter the phase and amplitude as a function of the spatially dispersed frequencies. The position occupied by the SLM is known as the Fourier plane. The SLM is a pixellated dual row of 640 variable retardance waveplates; each pair of waveplates addresses a different small range of frequencies. After refocusing the modulated field and combining on a second grating, the modulated light pulse leaves the shaper.

Pulse shaping techniques in the frequency domain for femtosecond pulses have enabled huge advances in the field of molecular coherent control. Shaped pulses have proved to be an effective tool for exercising control over the branching ratios in dissociation reactions.[5,6] Such control mechanisms have tended to rely on multi-photon excitations to access excited molecular states, together with simultaneous perturbations and re-arrangements of molecular bonds that occur *via* the AC Stark effect due to the intense electric field of the excitation laser. Weak field coherent control is an important complementary tool because under such conditions, insights into the nuclear dynamics on the unperturbed, field-free potential energy surfaces, during the process of a

photochemical reaction, may be obtained. Many organic molecules require shorter wavelength photons in the ultraviolet region of the spectrum to access the excited electronic states in a single-photon process. The possibility of steering excited state molecular dynamics of such species using tailored ultraviolet (UV) pulses is very exciting; however, at present there is a divergence between the capabilities of commercially available pulse shaping technology and the requirements of such weak field coherent control. The most common pulse shaping technologies are constrained to a wavelength range from the near infrared (IR) to the visible.

UV pulse shaping

Pulse shaping directly in the UV is possible using micromechanical mirrors[7]; however, this technique is still under development and is currently limited to smooth and low-amplitude phase shapes. The two predominant methods for producing shaped pulses both use programmable mask technologies: acousto-optic mask (AOM) devices and liquid crystal modulators, both shape in the Fourier domain within a 4*f* zero-dispersion compressor setup. Very recently, direct pulse shaping in the UV at 262 nm has been achieved using a fused-silica acousto-optic modulator (FS-AOM).[8] Acousto-optic programmable dispersive filters (AOPDFs) are a more recent development of AOM technology and operate directly on the beam, cutting out the difficulties of alignment but also losing the higher resolution possible within a 4*f* setup.[9]

Commercial spatial light modulators (SLMs) have very high resolution and may be employed to create highly complex pulse shapes. They do not usually operate effectively at UV wavelengths; however Hazu and co-workers have recently developed a novel UV-transparent liquid crystal SLM,[10] which is not yet commercially available. In an attempt to manipulate the phase and amplitude of UV light using commercially available SLMs, non-linear techniques such as sum frequency generation (SFG)[11] and second harmonic generation (SHG)[12] have been used to shift a shaped waveform to a higher carrier frequency in the UV—so called indirect UV pulse shaping.

Indirect pulse shaping has been demonstrated experimentally by several groups[10-14] and studied theoretically by Wang *et al.*[15] Most of these studies have focused on UV shaped pulse generation by sum frequency mixing or Type II second harmonic generation (SHG). In Type II SHG and SFG, the polarisations of the two light beams are mutually perpendicular, and one of the beams may be shaped and the other unshaped. Gerber and co-workers produced shaped UV pulses at the third harmonic of the output of a Ti–sapphire laser by using sum-frequency generation of shaped 800 nm pulses with a temporally stretched 400 nm pulse.[11] The 400 nm pulse was stretched to ensure complete temporal overlap with all parts of the shaped light. Schriever *et al*. have reported a similar indirect UV pulse shaping capability using the output of a non-collinear optical parametric amplifier (NOPA) in a pulse shaper followed by SFG with 775 nm beam to produce shaped light in the near UV at 344 nm, with some very short sub-pulse structures (19 fs).[14] Their method has the advantage of tuneability—the NOPA may be tuned so that pulses at a wide range of UV wavelengths may be generated. These SFG indirect shaping techniques have proved capable of producing highly structured pulses in the UV. The disadvantage of the method, and for indirect UV pulse shaping by Type II SHG, is that it is complicated by the necessity of mixing in a temporally stretched pulse to cover the time window of the shaped pulse: the result is a shaped UV pulse with an additional inherent chirp for which some compensation must be made. Although many successful coherent control experiments have been achieved using nonlinear mixing of the harmonics of the 800 nm Ti–sapphire fundamental, there exists a need for a fully tuneable deep UV pulse shaping capability for quantum molecular dynamics and control.

Type I SHG, in which two photons of the same polarisation are converted into a single photon of double the frequency, offers the simplest experimental arrangement for indirect pulse shaping. A pulse may be shaped in the infrared or visible region of the spectrum and then frequency doubled, simply by placing a correctly cut doubling crystal in the beam path, to reach the wavelength of interest. To the best of my knowledge, only one implementation of this indirect shaping method has been reported in the

literature: Hacker *et al.* were able to measure the spectra of shaped pulses at 400 nm that had been generated by SHG of a sinusoidal phase modulated 800 nm pulse.[12] The authors highlighted some key aspects of this conversion technique, namely that the preservation of the phase of the field in the SHG up-conversion process is dependent on the type of function on the phase of the input electric field. They also speculated that the phase profile of a sinusoidal phase shape is not preserved in the up-conversion process but were unable to measure the phase of the up-converted light. Owing to the simplicity and versatility of the experimental setup, the method selected to generate the shaped deep UV ultrafast pulses presented in this chapter, was to use a standard SLM setup to shape the visible output of one of the OPAs followed by Type I SHG. The effectiveness of a pulse shaping and Type I SHG setup, as pioneered by Hacker *et al.*, is demonstrated by the results in Section 2.6 in which the fully characterised shaped UV pulses are presented.

The design of the pulse shaper itself, operating in the visible, is described in Section 2.5. The chosen arrangement of mirrors, grating and SLM is only one of many arrangements that can be used. Cylindrical mirrors were chosen rather than lenses for focussing to avoid the chirp added to pulses by passing them through solid materials. In the folded-reflective mode, a mirror is placed directly behind the SLM, and the second 2*f* of the pulse shaper path is the same as the first except that it is slightly displaced out of the *f* plane. The near-Littrow folded-reflective geometry was chosen due to the low level of chromatic aberrations induced compared with other arrangements.[16] This design was recommended by Monmayrant and Chatel, because of its simplicity of alignment albeit at a slight cost to efficiency.[17] The line-spacing of the grating was used to determine the necessary focal distance required for the convex mirrors in order to achieve adequate dispersion of the light at the Fourier plane of the SLM. The focal length is chosen so that a total of four times the FWHM of the bandwidth of the visible pulse, which has a measured bandwidth corresponding to 40 fs at the transform limit, is focussed over the entire length of the SLM. This results in a wavelength-to-pixel ratio of 0.08 nm. The resolution of the shaper is not limited by this wavelength-to-pixel ratio but by the spot

size of the focus at the SLM, which using Gaussian optics can be calculated to be in inverse proportion to the original spot-size of the beam before the SLM. In this experiment, the resolution of the shaper is about 0.1 nm, with an error associated with the measurement by eye of the spot-size of the input beam.

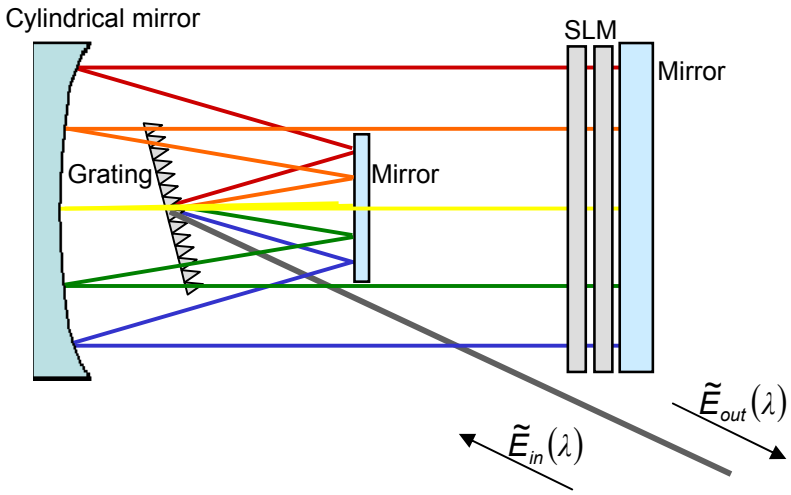

Figure 2.7 Illustration of folded near-Littrow geometry 4*f* shaper. The laser enters and exits the pulse shaper *via* the same mirrors and grating, hence only 2*f* is shown. Compare this with Fig. 2.6, which is an arrangement rarely seen in a laboratory due to the unwanted chirp gained by passing a femtosecond beam through a lens.

The phase and amplitude of the output pulse are dependent on the sum and difference between the retardances of each of the two SLM arrays, and so the phase and amplitude of the pulse may be independently shaped. The output electric field, E_{out}, can be derived using Jones matrix formalism and is written as,

$$E_{out} = \begin{pmatrix} E_x \\ E_y \end{pmatrix} = \exp\left(i\left[\Delta\phi_1 + \Delta\phi_2\right]/2\right)\begin{pmatrix} \cos\left(\left[\Delta\phi_1 - \Delta\phi_2\right]/2\right) \\ 0 \end{pmatrix}, \tag{2.7}$$

where E_x and E_y refer to the components of the electric field vector in the x and y directions respectively for light propagating in the z direction, and $\Delta\phi_1$, and $\Delta\phi_2$ are the phase retardance of each of the two SLM arrays[18]; the resultant electric field is plane polarised. This relation allows simple programmes to be written to convert the desired

phase, $[\Delta\phi_1 + \Delta\phi_2]/2$, and amplitude, $\cos([\Delta\phi_1 - \Delta\phi_2]/2)$, of a pulse into the wavelength-dependent retardances of the two SLM arrays $\Delta\phi_1$ and $\Delta\phi_2$.

2.4 Design of characterisation for the UV pulse shaper experiment

Pulse characterisation background

The spectral profile of an ultrashort laser pulse can be measured using a spectrometer. The spectral bandwidth can be related to the minimum pulse duration by the time-bandwidth product (Eq. 2.2) to indicate the approximate duration of an ultrashort laser pulse, if the laser system generating the pulse is ideal. Usually, numerous optical elements are involved in the production of pulses at the desired wavelength, and this causes distortions in the phase of the pulse that need to be removed using feedback from a measurement of the true pulse duration. Autocorrelation of the pulse using a second harmonic generation crystal is the simplest method by which an indication of the true pulse duration may be obtained. In an SHG autocorrelation measurement, the pulse is overlapped with a delayed replica of itself (produced by a beamsplitter and an optical delay line) in a nonlinear crystal and a signal will be detected at twice the frequency of the input pulse frequency (due to the second term in Eq. 2.1). The magnitude of the signal is proportional to the amount of temporal overlap of the two pulses, and hence the resulting measure of SHG intensity as a function of time will be similar in length to that of the input pulses. For a Gaussian pulse the autocorrelation intensity signal has a FWHM that is $\sqrt{2}$ times the input electric field pulse duration. A cross-correlation measurement may be recorded similarly by recording the second order nonlinear signal produced as a function of delay between a reference and an unknown pulse in a nonlinear crystal. Alternatively, a useful method of measuring the cross-correlation of two pulses used in a two-colour pump-probe experiment is to characterise them in a molecular sample, similar to the one upon which the pump-probe experiments will be carried out. For example, a two-colour photoionisation experiment may be adapted so that a molecule may be non-resonantly ionised using the two photons of the two-colour

experiment, giving the cross-correlation from the electron or ion yield measured as a function of delay. In some cases, further characterisation of the laser pulse is desirable. Complete characterisation is the term given to the measurement of the intensity and phase of the electric field, as a function of either time or frequency. Methods of complete characterisation are based on spectral interferometry (the SPIDER method),[19] spectrogram measurement (FROG),[20] and the multiphoton intrapulse interference phase scan (MIIPS) method, in which the diagnostic tool is SHG intensity measured as a function of reference phases added by a pulse shaper.[21]

SPIDER

Spectral phase interferometry for direct electric field reconstruction (SPIDER) was invented in 1998 by Ian Walmsley and co-workers.[22] Spectral (or temporal) phase is not a directly measurable quantity, but in the SPIDER technique the relative spectral phase of the laser pulse, $\phi(\omega)$, is encoded onto a spectral intensity quantity. SPIDER is a self-referencing method, and hence previously characterised pulses are not required in order to characterise an unknown ultrafast laser electric field using this measurement. SPIDER as an optical technique is a form of spectral interferometry; an illustration of the method is given in Fig. 2.8.

The methodology of SPIDER and spectral interferometry has been reviewed,[19,23] and what follows is based on those accounts. A spectrometer measures the spectral intensity of the light incident upon it, $S(\omega)$, that is, the time-averaged product of the spectral electric field, $\widetilde{E}(\omega)$, and its complex conjugate,

$$S(\omega) = \left\langle \widetilde{E}(\omega) \cdot \widetilde{E}(\omega)^* \right\rangle_T . \tag{2.8}$$

The time-average is over a time, *T*, that is very long compared to the duration of the laser pulse. If $\widetilde{E}(\omega)$ is the sum of two pulse replicas that are separated by a frequency, Ω, and a time, τ, Eq. 2.8 reduces to a spectral interferogram of the form

$$S(\omega) = \left|\widetilde{E}(\omega)\right|^2 + \left|\widetilde{E}(\omega-\Omega)\right|^2 + \left|\widetilde{E}(\omega)\right|\left|\widetilde{E}(\omega-\Omega)\right| \exp\{\pm i[\phi(\omega) - \phi(\omega-\Omega) - \tau\omega]\}. \tag{2.9}$$

The first two terms are filtered out by Fourier transform; then after Fourier transform back to the frequency domain, and calibration of the time delay, τ, the phase can be extracted algebraically from the third term on the right-hand side of Eq. 2.9, $\phi(\omega)-\phi(\omega-\Omega)$. Reconstruction of the phase across the spectrum of the pulse is then achieved by concatenation of these phase differences. The phase, in combination with a measurement of the spectrum of the pulse completely characterises the pulse.

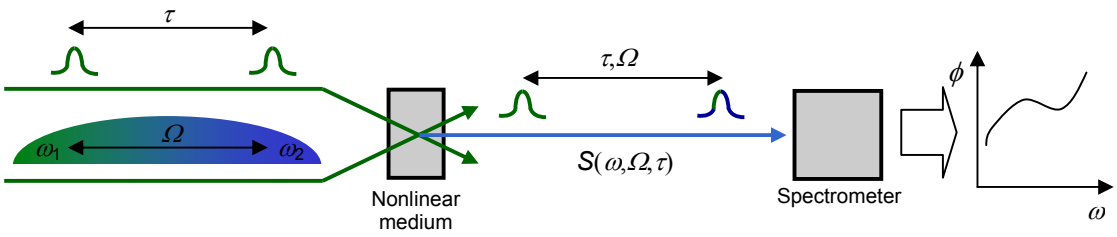

Figure 2.8 Schematic illustration of a SPIDER experiment. Two replicas of the pulse, separated by a time delay, τ, are mixed in a non-linear medium with another pulse that is strongly chirped. The result is a pair of pulses that are frequency sheared by an amount, Ω, as well as separated by τ. The interference between these two pulses, $S(\omega,\Omega,\tau)$, is measured in a spectrometer, and the spectral phase is retrieved from this by a simple algebraic method after filtering and calibration of the interferogram spectrum.

FROG

Frequency-resolved optical gating (FROG) is an older technique than SPIDER and was invented by Rick Trebino and Dan Kane in 1993.[24] FROG was the first measurement technique to fully characterise ultrashort pulses and since its invention the methodology has been developed and adapted in many directions for a range of different applications including that of coherent control of molecular photochemistry.[25] A recent book by Trebino compiles much of the research published thus far in the field of FROG measurement, together with much discussion of practical implementation issues such as sampling rates, energy thresholds and sensitivity,[20] which has facilitated much of the discussion in this section.

In considering the methodology by which FROG measures an ultrashort laser pulse, we will return to the intuitive picture of an ultrashort pulse discussed in Chapter 1, Section 1.2, that of the intensity in an ultrashort pulse being distributed across a finite range of frequencies and a range of times. Within such a picture, the obvious way to measure the pulse, is to build up a 2D plot of intensity versus time and frequency by sampling the pulse with a time gate and recording the spectrum of (frequency-resolving) each time-gated slice of the pulse. To time-gate an event, a comparably short event must be used, and as ultrashort pulses are several orders of magnitude shorter than the fastest electronics, the only way to time-gate the pulse is to use another femtosecond pulse or the pulse itself. This is the basis of Kane and Trebino's original self-referencing FROG method, where the uncharacterised laser pulse is used to gate itself by overlapping two replicas of the pulse in an instantaneously responding (usually a second harmonic generation (SHG) crystal) with a time delay, τ, between the two pulses. Under these conditions, an SHG signal measured as a function of the delay between two pulse replicas, has an electric field, $E_{sig}(t,\tau)$, proportional to the product of the two electric fields, $E(t)$ and $E(t-\tau)$:

$$E_{sig}(t,\tau) \propto E(t)E(t-\tau). \tag{2.10}$$

The measurement of the intensity of $E_{sig}(t,\tau)$ as a function of τ is the autocorrelation of the laser pulse, a quantity that has been used for many decades as an approximate indication of the duration of a pulse and its structure. Due to the symmetrising, and also the smearing-out, of $\left|E_{sig}(t,\tau)\right|^2$ over $\pm\tau$, the intensity autocorrelation cannot really measure ultrashort pulse structure with any certainty, unless the pulse is known to be transform limited. Measurement of $\left|E_{sig}\right|^2$ as a function of frequency as well as delay, τ gives a FROG trace. Thus, an important experimental definition of FROG is that it is simply the recording of the spectrum of the intensity autocorrelation of the laser pulse. Hence, the experimental setup of a FROG is that of an autocorrelator with a grating spectrometer in place of a photodiode. The experimental setup for FROG measurement is illustrated in Fig. 2.9.

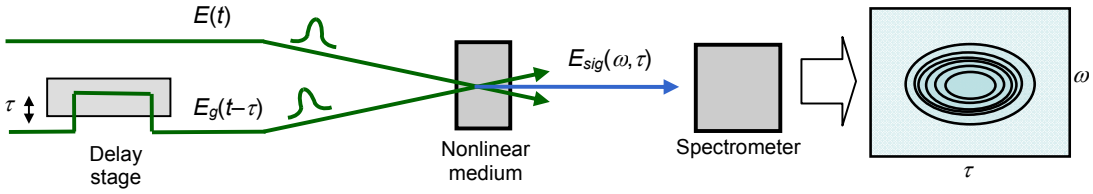

Figure 2.9 Schematic diagram of a FROG experiment. An unknown pulse enters the FROG and is split by a beam splitter. One of the split beams is delayed with respect to the other by τ before the two beams are focussed into the nonlinear crystal. The crystal acts as an instantaneously responding non-linear medium that emits a photon with a central frequency that is the sum of the central frequencies of the two input beams overlapped in it (shown in green). The signal field from the SHG crystal (in blue) is dispersed and measured as function of frequency. The measurement is repeated iteratively for different values of the delay τ, across the duration of the pulse, to obtain the FROG trace (spectrogram) as function of delay and frequency. Although this is an illustration only, the experimental arrangement is quite simple, and requires very few extra optical elements than the ones shown here, in contrast to the SPIDER experiment shown in Fig. 2.8.

Mathematically the FROG trace, $I_{FROG}(\omega,\tau)$, measured as a function of delay, τ, and angular frequency, ω, is defined as the square modulus of the Fourier transform of the time-domain SHG signal field, $E_{sig}(t,\tau)$,

$$I_{FROG}(\omega,\tau) \equiv \left| \int_{-\infty}^{\infty} E_{sig}(t,\tau) \exp(-i\omega t)\, dt \right|^2 \tag{2.11}$$

$$\cong \left| \int_{-\infty}^{\infty} E(t) E(t-\tau) \exp(-i\omega t)\, dt \right|^2 \tag{2.12}$$

Unlike SPIDER, this is not a direct measurement of the phase of a pulse, but instead measures a quantity known as the FROG trace and defined above, in Eq. 2.11. The FROG trace, as has already been discussed, provides a great deal of qualitative information about the pulse. It is also possible to use the FROG trace to obtain an analytic expression for the waveform, either in the time domain, Eq. 1.9, or the frequency domain, Eq. 1.10, using a specialised FROG algorithm.

The FROG algorithm is an iterative algorithm that essentially finds an electric field that is a fit to the FROG trace. By inspecting Eq. 2.12, it can be seen that the phase information is encoded in the product of the delayed electric field replicas, $E(t)E(t-\tau)$, and it is in fact the case that the FROG algorithm retrieves a unique electric field for the trace. By substituting the Fourier transform with respect to τ of the signal field, $E_{sig}(t,\tau) = \int_{-\infty}^{\infty} \widehat{E}_{sig}(t,\Omega)\exp(-i\Omega\tau)\,d\Omega$ into the definition of the FROG trace, Eq. 2.11, we obtain

$$I_{FROG}(\omega,\tau) \equiv \left| \int_{-\infty}^{\infty}\int_{-\infty}^{\infty} \widehat{E}_{sig}(t,\Omega)\exp(-i\Omega\tau - i\omega t)\,d\Omega\,dt \right|^2 . \tag{2.13}$$

Inversion of Eq. 2.13 to find $\widehat{E}_{sig}(t,\Omega)$ is a 2D phase retrieval problem, to which a unique solution exists.[20] Once this is solved, $E_{sig}(t,\tau)$ is easily found by Fourier transforming $\widehat{E}_{sig}(t,\Omega)$ with respect to Ω and then, by setting τ to zero, $E(t)E(0)$ is given. This is simply the desired electric field solution, $E(t)$, multiplied by an amplitude and an absolute phase factor, both of which can be neglected, since the absolute phase, as already discussed is of no importance, and the absolute electric field amplitude is also of little importance.

The existence of a unique solution to a 2D phase retrieval problem such as the inversion of Eq. 2.13 is because of the failure of the fundamental theorem of algebra for polynomials of more than one variable.[20] Obtaining the time dependent electric field, $E(t)$, from the spectrum, $S(\omega)$, by inversion of

$$S(\omega) \equiv \left| \int_{-\infty}^{\infty} E(t)\exp(-i\omega t)\;dt \right|^2 , \tag{2.14}$$

is the 1D phase retrieval problem and it is well-known to be impossible: many different electric fields may be constructed from the same spectral intensity in combination with a variety of spectral phases. The details of the FROG algorithm are quite complex, what has been described above is a brief outline of its basis, rather than a description of the algorithm itself. Even when written in the most compact form, the FROG algorithm can be slow for the complicated FROG traces produced by highly shaped pulses. Faster FROG algorithms are now available commercially.

UV pulse characterisation

As well as the requirement to characterise an arbitrarily shaped UV pulse, an additional challenge to the pulse characterisation scheme was that the pulse produced after doubling the shaped UV beam would be very weak. Its energy was estimated conservatively at about 1 μJ.

The main reason why a SPIDER-based method is preferable to the more conventional FROG based techniques for retrieving shaped pulse electric fields is that SPIDERs provide a more direct measurement of the phase of the pulse, and the algorithm used to retrieve the phase from the experimental interferogram consists only of filtering and algebraic manipulation. Thus, the SPIDER algorithm is fast and SPIDERs can be used to provide real-time phase retrieval.[26] Also, the amount of data needed for a SPIDER measurement is much smaller than that needed for a FROG measurement – one spectrum for SPIDER compared with a set of many spectra for FROG. At the time of designing this experiment, to my knowledge, SPIDER methods had not yet been implemented as a coherent control pulse diagnostic. So, in collaboration with members of the Walmsley group at Oxford University, the development of a method of this type for use as a pulse shaping diagnostic for coherent control was undertaken as it was expected to be a of interest as a novel application of this optical metrology technique.

SPIDER-based pulse characterisation solutions

There are two main reasons why the SPIDER method alone cannot be used to characterise a long pulse train. Firstly, SPIDER is essentially a measurement of the spectral phase, $\phi(\omega)$, and we must know in advance that $\phi(\omega)$ will be a smooth function without any fast variations; if it its not, then the phase may not be sampled often enough to correctly reconstruct the phase, as the discontinuities or fast oscillations in $\phi(\omega)$ will be missed. The sampling interval cannot be arbitrarily reduced in an attempt to try to eliminate the possibility of under sampling because in the SPIDER experiment, the sampling interval is the spectral shear between the unknown pulse replicas, Ω, which is produced by overlap with chirped pulse (see Fig. 2.8). The second

reason that SPIDER is inappropriate for measuring pulse trains also has to do with the fact that in SPIDER, spectral phase differences across sections of the pulse are measured, and then concatenated together to give the entire spectral phase structure. If the spectral intensity of the pulse goes to zero at any point, and this is likely if the pulse shape is actually a complex train of pulses, no information about a phase differences blinked to such a point will be given (see Eq. 2.9, where the third term on the right will fall to zero) and the concatenation of the phase will fail. A solution to both of these problems is found by using a SPIDER to measure a reference pulse, whose spectral phase and intensity is known in advance to be well-behaved, and then carrying out a spectral interferometry (SI) experiment to recover the phase of the shaped pulse from the phase differences between the reference pulse and the shaped unknown pulse. As already mentioned, SI is the method from which SPIDER was developed. An interferogram from the interference between the two electric fields, $\widetilde{E}_{ref}(\omega) = \left|\widetilde{E}_{ref}(\omega)\right| \exp\left[i\phi_{ref}(\omega)\right]$ and $\widetilde{E}_{unk}(\omega) = \left|\widetilde{E}_{unk}(\omega)\right| \exp\left[i\phi_{unk}(\omega)\right]$, is measured, and has the form

$$S(\omega) = \left|E_{ref}(\omega)\right|^2 + \left|\widetilde{E}_{unk}(\omega)\right|^2 + \left|\widetilde{E}_{ref}(\omega)\right|\left|\widetilde{E}_{unk}(\omega)\right| \exp\left\{\pm i\left[\phi_{ref}(\omega) - \phi_{unk}(\omega) - \omega\tau\right]\right\}. \quad (2.15)$$

The reference electric field phase, $\phi_{ref}(\omega)$, is known in advance, so the phase of the unknown electric field, $\phi_{unk}(\omega)$, is given exactly, after calibration of τ, and a Fourier transform and filter technique analogous to the one used for SPIDER. Crucially, unlike SPIDER, no concatenation is required, and hence the SI method would solve the problem of the failure of the SPIDER method to reconstruct the phase of a pulse with spectral intensity zeroes. A SPIDER, or a zero additional phase (ZAP) SPIDER,[27] could be used characterise the phase of a reference unshaped pulse, $\phi_{ref}(\omega)$, which could then be used to reconstruct the phase of the unknown shaped pulse, $\phi_{unk}(\omega)$, by interfering the two pulses. The zero additional phase (ZAP) SPIDER[27] is very similar to a basic SPIDER, except that the chirped pulse used to create the spectral shear, rather than the unknown pulse, is split and time-delayed, thereby removing a small additional phase introduced by the beam splitter into one of the unknown pulse replicas. In the SPIDER measurement of the reference pulse, as for all SPIDER measurements, the phase would be sampled at intervals separated by Ω and then averaged between the measured points

to give a continuous function. The averaging of the measured phase data for the reference unshaped pulse is reasonable, given the fact that it is known in advance that spectral phase function should be nearly linear, or at least continuous and smooth. Such averaging would not be appropriate for the spectral phase function of the arbitrarily shaped laser pulse because of the danger of under sampling with too large a spectral shear. The SI component of the proposed combined measurement experiment means that the phase of the shaped pulse can be sampled with a resolution limited only by the resolution of the spectrometer in which its interference with the reference pulse is detected. The cross-referencing method therefore allows the phase of the shaped pulse to be measured with higher resolution than a simple SPIDER experiment, as well as preventing any failure of the phase retrieval algorithm due to possible zeroes in the spectral intensity.

The interferogram produced by the spectral interferometry part of this possible cross-referencing characterisation scheme, $\widetilde{S}(\omega)$ in Eq. 2.15, yields the phase difference, $\phi_{ref}(\omega)-\phi_{unk}(\omega)+\tau\omega$, after the Fourier transform, application of a filter, $D(t+\tau)$ (usually a fourth-order super Gaussian, an exponential function of the fourth power of a variable), and inverse Fourier transform are applied to the interferogram:

$$\phi_{ref}(\omega)-\phi_{unk}(\omega)+\tau\omega=\mathrm{Im}\left[\ln\left(\frac{\left[FT\left\{D(t+\tau)\widetilde{S}(t)\right\}\right]}{\left|\widetilde{E}_{ref}(\omega)\right|\left|\widetilde{E}_{unk}(\omega)\right|}\right)\right]. \tag{2.16}$$

$\phi_{unk}(\omega)$, then, can be obtained directly after calibrating for the delay, τ, between the two pulses and subtracting the phase of the reference pulse, $\phi_{ref}(\omega)$, obtained from the SPIDER measurement. $\phi_{unk}(\omega)$ and the spectral amplitude, $\left|\widetilde{E}_{unk}(\omega)\right|$ (which can be extracted from the real part of the right-hand side of Eq. 2.16, above, and the known value of $\left|\widetilde{E}_{ref}(\omega)\right|$), specify the spectral electric field envelope of the shaped pulse; Fourier transforming gives the temporal analytic electric field envelope, $E_{unk}(t)$, in terms of the temporal phase, $\phi_{unk}(t)$, of the pulse and its temporal amplitude, $\left|E_{unk}(t)\right|$.

$$E_{unk}(t)=\left|E_{unk}(t)\right|\exp\left[i\phi_{unk}(t)\right] \tag{2.17}$$

For cases where the pulse to be characterised is weak, the homodyne optical technique (HOT) SPIDER technique is a higher sensitivity measurement that can be used in place of a conventional SPIDER measurement. In a HOT SPIDER experiment, a more intense laser pulse, the homodyne pulse, is interfered separately with each of the frequency-sheared replicas,[28] which are delayed by τ' from the homodyne pulse, $\widetilde{E}_H(\omega) = \left|\widetilde{E}_H(\omega)\right| \exp\left[i\phi_H(\omega)\right]$. The homodyne pulse acts to increase the intensity of the interferogram and thus raise the interference fringes above the level of background signal in the spectrometer measurement. The analytic form of the two measured interferograms is

$$S_{H,1}(\omega) = \left|\widetilde{E}_H(\omega)\right|^2 + \left|\widetilde{E}(\omega)\right|^2 + \left|\widetilde{E}_H(\omega)\right|\left|\widetilde{E}(\omega)\right| \exp\left\{\pm i\left[\phi_H(\omega) - \phi(\omega) - \tau'\omega\right]\right\} \tag{2.18}$$

$$S_{H,2}(\omega) = \left|\widetilde{E}_H(\omega)\right|^2 + \left|\widetilde{E}(\omega-\Omega)\right|^2 + \left|\widetilde{E}_H(\omega)\right|\left|\widetilde{E}(\omega-\Omega)\right| \exp\left\{\pm i\left[\phi_H(\omega) - \phi(\omega-\Omega) - \tau'\omega\right]\right\} \tag{2.19}$$

For each of $S_{H,1}(\omega)$ and $S_{H,2}(\omega)$, the positive interference term is isolated *via* the same Fourier transform and filter method used in the standard SPIDER technique. Because the delay between the homodyne pulse and the replica is kept at a constant value of τ' for each of the pair of interferogram measurements, the difference between the arguments of Eqs. (2.18) and (2.19) is the phase difference between the sheared pulses, and calibration of τ' is not required to give the phase difference term:

$$\phi(\omega) - \phi(\omega-\Omega) = \mathrm{Im}\left[\ln\left(\frac{\left[FT\left\{D(t+\tau)\widetilde{S}_{H,1}(t)\right\}\right]\left|\widetilde{E}(\omega-\Omega)\right|}{\left[FT\left\{D(t+\tau)\widetilde{S}_{H,2}(t)\right\}\right]\left|\widetilde{E}(\omega)\right|}\right)\right]. \tag{2.20}$$

In order for HOT SPIDER phase characterisation to be possible, the homodyne pulse must have bandwidth of significant intensity encompassing the bandwidth of both of the two sheared replicas. The relative phase is concatenated from the extracted phase difference as for the standard SPIDER technique. The HOT variant of the SPIDER technique is advisable for the characterisation of the reference pulse because, in order for optimum interference in the SI experiment, the reference pulse must be centred at the same ~254 nm wavelength as the shaped pulse and therefore it will be fairly weak. The output energy of the OPA at 254 nm is always low, ~5 μJ; the input to the pulse shaper could be frequency-doubled and used as the reference pulse. In HOT SPIDER, the

spectrally sheared pair are not interfered together, are not therefore produced simultaneously, so the technique has a further experimental advantage in that, like the ZAP SPIDER method, the additional phase error associated with use of a beam splitter is avoided.

Implementation of a SPIDER and SI characterisation scheme

As for all SPIDER measurements, the spectral shear in a HOT SPIDER measurement, Ω, is effected by non-linear mixing of each of the unknown pulse replicas with different temporal portions of a strongly chirped auxiliary pulse. In general, a pulse, often though not exclusively of a similar frequency to the unknown pulse, is chirped and then temporally and spatially overlapped in a non-linear crystal with the two time-separated replicas of the input pulse. If the chirp is of sufficient magnitude and the pulses delayed sufficiently, the entirety of the duration of the unknown pulse is mixed with a quasi-monochromatic section of the chirped pulse and the non-linear mixing produces a perfect spectral shear between the pulses. The first SPIDER experiments used frequency up-conversion, i.e. SFG or SHG, as the non-linear mixing process, but a difference-frequency generation (DFG) SPIDER has been reported in the literature,[29] and this would be appropriate for the measurement of the 254 nm pulses produced by the laser system of the coherent control experiment. The light used to create the chirped pulse in such a setup will be from the chirped pulse amplifier, with a central wavelength of 795 nm and a pulse duration of 35 fs. These pulses would be stretched with a dispersive glass block or pair of gratings and mixed in a DFG crystal to produce the spectrally sheared pair, S_1 and S_2, at around 373 nm wavelength.

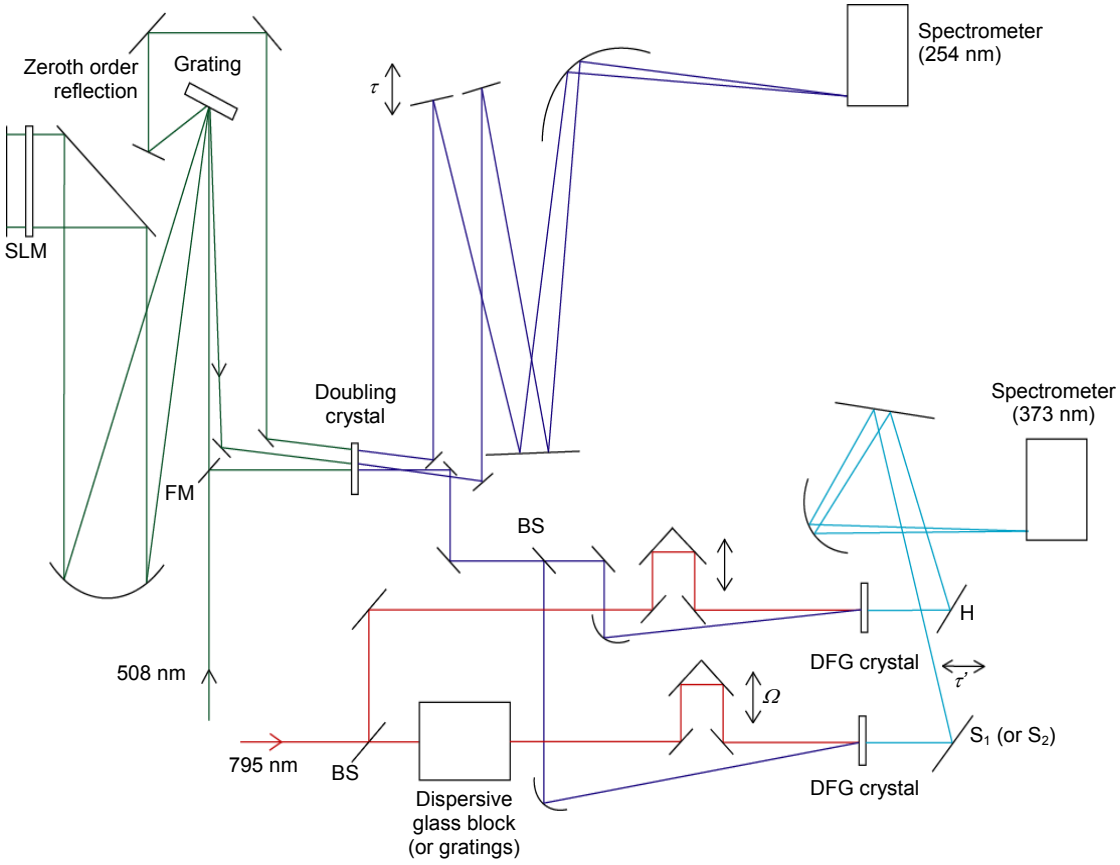

Figure 2.10 Proposed possible SPIDER and spectral interferometry characterisation scheme, including the pulse shaper. The colours of the rays indicate the approximate relative frequencies of the light; the beam splitter is labelled BS, and the flip mirror is labelled FM. In the HOT DFG SPIDER part of the experiment (bottom right hand corner of the figure), the homodyne pulse, H, is created at the same time as one of the sheared pulses (S_1 or S_2) in adjacent difference frequency generation (DFG) crystals; a delay, τ', is then introduced before interfering them in a spectrometer. These two pulses are created by DFG with the unshaped ~254 nm beam from the doubled pulse shaper input, and chirped (S_1, S_2) and unchirped (H) 795 nm beams; H, S_1 and S_2 are all of approximately 373 nm wavelength. The delay labelled Ω is adjusted before the second of the HOT SPIDER interferograms is recorded. The shaped pulse characterisation requires the flip mirror to be removed so that the light enters the pulse shaper. For the shaped and reference pulse interferogram measurement, the output and the zeroth order reflection from the pulse shaper (both ~508 nm) are doubled *via* different paths in the doubling crystal before introducing a delay, τ, between them and interfering them in the 254 nm spectrometer.

For a HOT SPIDER, the temporal portion of the chirped pulse that is mixed with the input pulse could be made to differ between the two interferogram measurements by changing the path length of the chirped pulse before it reaches the crystal; the homodyne pulse, H, could be produced by direct down conversion of the input 254 nm pulse with an unchirped 795 nm pulse; H would then have considerably higher intensity than either of the pair of sheared pulses and therefore its spectral bandwidth would encompass the measurable spectral bandwidth of both of the sheared pulses. A proposed setup for a pulse characterisation experiment along these lines, is shown in Fig. 2.10 with the pulse shaping optics, and described in the caption.

Resolution problems with a SPIDER and SI characterisation scheme

One major problem prevented the implementation of a SPIDER with spectral interferometry cross-referencing characterisation scheme such like that in Fig. 2.10 above. An estimate of the shaping window from the resolution of the pulse shaper is about 10 ps: this is the maximum duration of a pulse produced by the frequency domain pulse shaper in the coherent control experiment without distortions. In a spectral interferometry experiment, the two pulses (reference and unknown) are separated by a delay, τ, before being interfered. The delay allows the time domain filtering of the interference signal at $t = \pm\tau$ (which contains the phase information) from the rest of the inteferogram at signal $t = 0$. Thus, in order to filter the interference signal containing the phase information, the time delay must be greater than the maximum duration of the pulse, $\tau > 10$ ps, where τ is the shaping window derived from the frequency dispersion on the pulse shaper and the energy-time uncertainty principle. However, if τ is of this order of magnitude, the fringes produced in the spectral domain, separated by $\Delta\omega = 2\pi/\tau$, occur at intervals of 0.02 nm or less for a spectrum centred at 254 nm. The all-important phase difference information is encoded into these fringes, and so the spectrometer used for the spectral interferometry would require a resolution of at least 0.01 nm to sample at the Nyqist limit and resolve the spectra fringes.[19] Commercial grating spectrometers are not produced with such high resolution, and so the only solution would be to use a home-built Fourier transform spectrometer, which would

significantly add to the technical difficulties involved in the pulse characterisation project. For this reason, other non-SPIDER based characterisation methods were examined as possibilities for the UV shaped pulses.

FROG-based UV pulse characterisation solutions

Experimentally, a FROG measurement is a measurement of the spectrum of the autocorrelation function of a pulse. Autocorrelation can be performed in either single-shot or multi-shot mode. In multi-shot mode, the path difference between the beam replica is adjusted step-wise over the duration of the pulse and a measurement is recorded at each step (as in Fig. 2.9, but with a photodiode in place of the spectrometer). In single-shot mode, the geometries of the pair of beams are arranged so that in the nonlinear crystal, the temporal overlap is mapped onto one dimension of the crystal and thus the entire autocorrelation is recorded in a single step using an imaging detector.

The single-shot autocorrelation method therefore is advantageous in terms of a reduction in data collection time, and has also been applied to the FROG method, by spectrally dispersing an SHG signal in a dimension orthogonal to the dimension of the temporal overlap mapping. This single-shot SHG FROG method was spawned by the standard multi-shot SHG FROG, as illustrated in Fig. 2.9 and has been named the GRating-Eliminated No-nonsense Observation of Ultrafast Incident Laser Light *E*-fields (GRENOUILLE), so called because a thick SHG crystal is used to disperse the light directly onto and imaging camera without the use of a grating spectrometer.[30] The GRENOUILLE has been commercially developed and marketed by Swamp Optics for use on lasers in the visible and IR regions of the spectrum. It is shown schematically in Fig. 2.11.

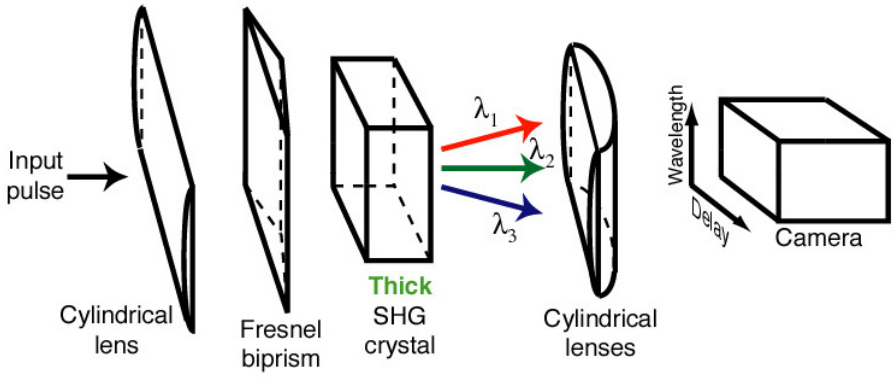

Figure 2.11 GRENOUILLE. Cylindrical lens and Fresnel biprism act to respectively line-focus and split the beam before it enters the SHG crystal. The thick crystal spectrally disperses the second harmonic in the direction orthogonal to the line focus to yield a 2D image of the FROG trace at the detector. Figure copied from Ref. 31.

The most commonly used FROG non-linear medium, second harmonic generation crystals, are not, however, appropriate for recording either the autocorrelation or the FROG trace of a pulse at 254 nm because there are no crystals suitable for doubling light of this wavelength. Autocorrelation and/or FROG traces can be generated using a variety of non-linear effects apart from SHG; some or all of which can be operated in single- or multi-shot mode. Many FROG measurements using different non-linear effects have been reported in the literature, each of these having their own advantages and disadvantages that make them suitable for specific applications. Such of the FROG methods that have been applied to UV pulse measurement are described below and issues such as sensitivity, ability to measure complex pulse train shapes, ease of setup and operation and the possibility of adaptation to different central wavelengths (so that the light from the pulse shaper, before doubling may also be measured, as a secondary experiment) are discussed in each case.

DFG XFROG and GRENOUILLE

This FROG-based combined method is not a standard self-referencing FROG technique but a cross-referencing method analogous to the cross-referencing spectral

interferometry pulse characterisation scheme design described already. A reference pulse at 795 nm, from the amplifier, would be characterised using a commercial GRENOUILLLE (as shown in Fig. 2.11) and commercial FROG trace retrieval algorithm and then used as a gate function in a difference-frequency generation (DFG) frequency resolved cross-correlation measurement (XFROG) trace measurement centred at around 373 nm. The layout of a cross-correlation experiment would be similar to that shown for a FROG in Fig. 2.9; the SHG crystal is replaced by a DFG crystal and the pulse on the variable delay-line is the gate function pulse at centred at 795 nm which is mixed with the shaped pulse centred at 254 nm. Also, to prevent chirping of the beam by passing through glass, the focussing optics must be spherical mirrors rather than lenses. DFG XFROG has been used to measure pulses of 400 nm wavelength by Linden *et al*. in a simple multi-shot experiment.[32] DFG crystals for use with 795 nm and 254 nm light are commercially available. Single-shot DFG XFROG has not yet been developed. Although easier to operate, it could prove unhelpful to adapt DFG XFROG to single-shot mode for the present experiment because in single-shot mode the total duration of the unknown pulse (train) corresponds to one of the dimensions of the DFG crystal, and the pulse train duration for the photochemical control experiment is as yet unknown. One drawback of using the XFROG method is that if the reference pulse is shorter than any delay between well-separated pulses in the unknown pulse train, the phase difference between the pulses cannot be retrieved, rendering the measurement attempt technically incomplete. In the proposed experiment, the reference 795 nm laser pulse has a temporal FWHM of 35 fs at the transform limit. The 795 nm light that will be used as a reference electric field, $E_{ref}(t-\tau)$, will be more than ten times as intense as the unknown pulse, increasing the magnitude of the difference-frequency generation non-linear signal field:

$$E_{sig}^{\mathrm{DFG}}(t,\tau) \propto E(t)E_{ref}^{*}(t-\tau). \tag{2.21}$$

Thus, the measurement of very weak pulses is possible using the DFG XFROG method. The XFROG method also has another benefit over SHG FROG. The SHG process symmetrises a FROG trace with respect to delay, τ, just as an SHG autocorrelation will be symmetric, whereas an XFROG trace is not symmetrised. The XFROG phase

retrieval algorithm is a simplified version of the FROG algorithm and commercial versions are available.

PG FROG

Polarisation-gate FROG (PG FROG) was one of the first FROG measurements, and in contrast to SHG FROG, it was invented as a single-shot measurement.[33] A PG FROG measurement was reported in the literature three years later by Michelmann *et al.* of 248 nm femtosecond UV light.[34] Polarisation gate is a third order non-linear effect. The input unknown light pulse is passed through a polariser and then divided into two. One of the replica pulses is then passed through a quarter waveplate, rotating its polarisation by 45° before it is focussed, along with the other replica, into a suitable Kerr medium (usually fused silica). The two beams are aligned so that the temporal overlap is mapped onto a dimension of the nonlinear medium, as described for the GRENOUILLE. At the PG medium, the probe beam (the beam not rotated by 45°) induces a birefringence in the crystal, which in turn induces a polarisation rotation of the probe beam, the degree of which is proportional to the intensity of the pump beam. Thus the light induced in the direction orthogonal to the initial polarisation is proportional to the product of the intensity of the pump beam and the amplitude of the probe beam. This orthogonally polarised light is detected after the Kerr medium by passing the probe beam through a polariser before focusing into a spectrometer with the spectral plane perpendicular to the plane of temporal overlap. The central frequency of the measured light is the same as the incident light, and so there is no need for the purchase of different optics for different wavelengths, as is often the case in nonlinear experiments. The PG FROG relies on a third order nonlinear effect and is thus a much less sensitive measurement than SHG FROG. The signal electric field produced by the medium and frequency resolved to give the PG FROG trace is given by:

$$E_{sig}^{PG}(t,\tau) \propto E(t)\left|E(t-\tau)\right|^2 . \tag{2.22}$$

The lower energy limit for measurement of pulses by PG FROG is 100 nJ,[20] which is a factor of ten lower than the pulse train that is the probable outcome of the shaped and doubled light from the coherent control experiment (~1 μJ). As a disadvantage of the

method, use of polarisers in the PG FROG setup introduces error in the measurement due to chirping of the beam by the polariser glass, and also on the beam splitter. Slightly more optics are involved in the PG FROG setup than in the DFG XFROG setup, although it is reportedly easy to align because of automatic phase-matching in the PG nonlinear process.[35] Adaptation of this setup to different wavelengths could involve the use of a different Kerr medium as well as different mirrors.

SD and TG FROG techniques

Self-diffraction (SD) FROG has been developed in multi-shot mode for use at 266 nm[36]; in this experiment, the beam was split by spatially dividing the beam with the edge of a mirror, instead of using a conventional beam splitter and thus introducing chirp. Sensitivity is about 1 μJ for SD FROG; this is the lower limit of the shaped and doubled light in the pulse shaping experiment, and so would not be the best choice for the characterisation scheme for the coherent control experiment. Transient grating (TG) FROG involves a complicated optical setup, most suitable for use *in situ* in a transient grating spectroscopic experiment, in which the correct optical alignment is already in place.[37] It is understood that a TG FROG is in development for commercial use for pulses in the UV by Swamp Optics, but unfortunately it will not be quite sensitive enough for the coherent control experiment.[17,38]

TADPOLE: FROG and spectral interferometry

A paper has been published on the combined use of a FROG reference pulse characterisation with the spectral interferometry for complete characterisation of a weak pulse; the method was named temporal analysis, by dispersing a pair of light *E*-fields (TADPOLE).[39] This has the extra advantages of using a linear (interferometric) technique to measure the unknown pulse and so it is sensitive to a very weak pulse and potentially very useful for the measurement of shaped UV pulses. However, in the present case, for the coherent control setup, the possibility of using spectral interferometry has already been eliminated because of the difficulty with the very high resolution spectrometer necessitated by the possibility of a 10 ps duration that could be

produced by the optimisation of the pulse shape in the SLM shaper with a genetic algorithm.

Resolution in FROG measurements

From the above discussions, it is clear that the best solution for the pulse characterisation project within the coherent control experiment is the DFG XFROG and GRENOUILLE; the proposed design for this experiment is shown the next section of this chapter. This is the most versatile solution, allowing the possibility of measurement of different pulse wavelengths with the minimum of difficulty. Use of the DFG XFROG + GRENOUILLE method could enable the measurement both of the shaped but undoubled light (at 508 nm) and the measurement of shaped and doubled light of a different central UV wavelength (for the control of a different molecular system) with the minimum of experimental rearrangement, using another nonlinear crystal. One issue remains to be discussed with regard to FROG measurements: sampling and resolution. This is an important issue to consider because it was this that made the development of a SPIDER based method impracticable. As stated in the literature, sampling issues in FROG measurements are complicated,[20] but this does not seem to have limited the complexity or duration and bandwidth of pulse traces measured using various FROG techniques.[40,41] There are examples in the literature of experiments in which FROG has been used to study quite complex picosecond duration pulses, and the SHG signal was simply dispersed and imaged onto a CCD camera to record the spectrum.[40] The fact that the FROG measurement is two-dimensional means that the pulse is effectively oversampled, and therefore the resolution in either the delay or the frequency axis of the FROG trace can be less than for that required in a SPIDER-type experiment for the same pulse. In comparison to the HOT SPIDER and SI experiment as summarised in Fig. 2.10, the number of optics required by a DFG XFROG experiment is much less, and hence the amount of alignment required to operate the experiment is also reduced.

2.5 UV pulse shaping and characterisation experimental arrangement

The experimental setup is shown in Fig. 2.12 for the production and characterisation of UV shaped pulses. The laser system was described in Section 2.2, and was used in this experiment as follows. Light pulses of 35 fs duration were produced at a 1 kHz repetition rate with central wavelength of 795 nm and 2.5 mJ per pulse (Coherent Legend regenerative amplifier seeded by a Coherent Mira Ti–sapphire oscillator). 1 mJ was used to pump a commercial OPA, and 0.5 mJ was sent to a beam line for the pulse characterisation setup. The sum frequency generation of the signal beam from the OPA, which operates at 508 nm for this work but is tuneable throughout the visible spectrum, has a spectral full width half maximum (FWHM) of 9.5 nm, a temporal FWHM of 80 fs and a pulse energy of 30 μJ, and was sent into a home-built pulse shaper device. The pulse shaper consists of a dual array 640 pixel SLM (CRI-640-VN-D) that is placed in the Fourier plane of a 4*f* zero-dispersion compressor setup and modulates the phase and amplitude of the femtosecond pulse. The optical layout was folded, and the SLM was operated in reflective mode. The shaped visible pulse was subsequently frequency doubled in a 100 μm BBO crystal to give 100 fs pulses centred at 254 nm with a bandwidth of 1 nm (for an unshaped pulse). Some bandwidth was lost in the SHG process, due to the non-negligible crystal thickness: the measured bandwidth of an unshaped pulse was reduced by a factor of 0.6 compared to the bandwidth calculated for SHG of the same pulse in a very thin crystal.

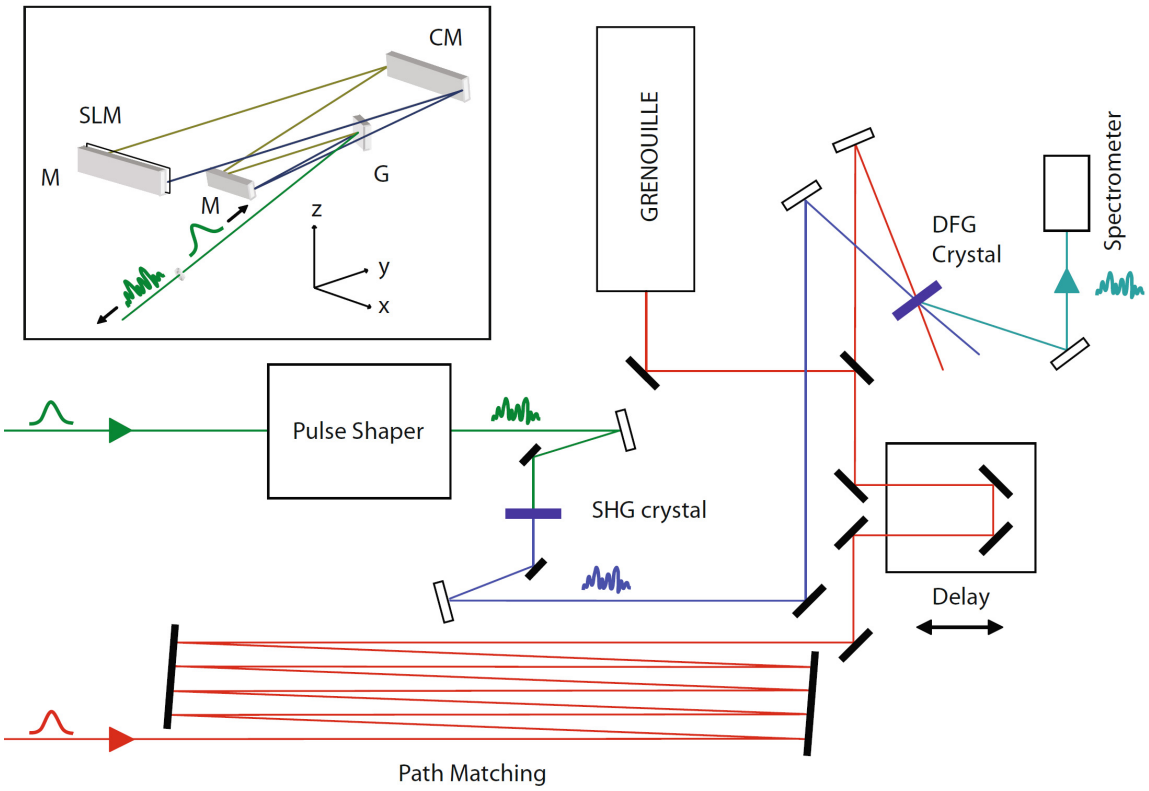

Figure 2.12 Experimental setup for the generation and characterisation of shaped UV pulses at 254 nm. The optical path length is described in detail in the text. All *thick black rectangles* represent mirrors, *open rectangles* spherical mirrors and *dark blue rectangles* non-linear crystals. Inset pulse shaper setup: A folded double-pass 4*f* zero-dispersion compressor setup is used in reflective mode. The back reflected beam is reflected slightly downwards to separate it from the incoming beam. (SLM = liquid crystal spatial light modulator, G = grating, M= mirror, CM = cylindrical mirror). Figure reprinted from Ref. 1.

The pulse shaper (Fig. 2.12, inset) is arranged as follows. First, the visible femtosecond pulse is diffracted using a 2400 lines/mm holographic grating at a near Littrow angle onto a folding mirror. The spatially dispersed beam is folded upwards over the grating by a folding mirror (FM) to a cylindrical focusing mirror (CM) with a focal length f = 560 mm whereupon the dispersed light is collimated and directed horizontally towards the SLM. Each of the 640 pixels is 98 µm wide with an inter-pixel spacing of 2 µm and

modulates a frequency component of width of approximately 0.08 nm. Approximately the central quarter of the SLM is filled with the FWHM of the spectral intensity of the pulse, so the full SLM addresses four FWHMs of the pulse. The position of each wavelength on the array of pixels had to be precisely calibrated. This was carried out using a slit placed in front of a pixel with known index, and measuring the spectrum of the light transmitted through the slit. After the pulse is modulated, it is reflected back through the SLM by a mirror. This results in the phase and amplitude of the input pulse being modulated twice by the SLM; a factor that was accounted for in calibration of the retardance of the pixels as a function of the programmed applied voltages. The back reflecting mirror is angled slightly downwards so that the beam can be picked off further down its path. The throughput efficiency in the visible region of the spectrum of the shaper was approximately ~50% with this setup, and produced unshaped pulses of about 15 μJ. The shaped visible pulse is subsequently focused into a 100 μm thick BBO crystal with spherical mirrors. Conversion efficiency is dependent on the pulse shape with maximum energy for an unshaped pulse of 2 μJ in the UV, which exceeds the demands of weak-field gas phase 1-photon excitation experiments in most organic molecules.

Each optical component of the pulse shaper was aligned sequentially, in the horizontal plane, by measuring the spatial position of the central wavelength, in this case 508 nm, which was passed through a slit placed on a central line of the setup. Change of the wavelength of the shaped UV pulses to 243 nm can be achieved easily by tuning the central wavelength from the OPA to 486 nm. With a change in wavelength, the only alterations to the shaping setup that are required are a slight adjustment to the grating angle to match the cylindrical mirrors and alteration of the BBO crystal angle to maximise the output signal.

The SLM was controlled with a series of programs (using LabView 8) that altered the phase of the incoming visible light to specific functions of wavelength. The frequency-doubled resulting shaped UV pulses were characterised using a home-built XFROG

setup. To find the temporal overlap between the shaped and unshaped pulses in the XFROG approximately, the two beams were directed together into a molecular beam chamber and the overlap determined from the photoelectron count as a function of delay. It was found that approximately 7 m of extra path length was required in the unshaped IR pulse (795 nm, approximately 1 μJ), as shown in Fig. 2.12. The shaped UV pulse and unshaped IR pulse were then focused into a difference frequency generation (DFG) crystal (BBO, 20 μm, purchased from APE), and the DFG signal was focused into the fibre optic of a spectrometer. During each trace measurement, the temporal overlap between the IR and the UV pulse was scanned through the UV pulse and the DFG spectrum was recorded every 10 fs. A Labview program connected the controller for the spectrometer with that for the delay stage (PI MikroMove) to automatically move the stage and record spectra. The IR pulse was characterised completely using a commercial GRENOUILLE (Swamp Optics UPM 8–20) and pulse characterisation software (Mesaphotonics VideoFrog version 6.0), and thus acts as a reference pulse. An example electric field from the GRENOUILLE measurement is given in Fig. 2.13. The DFG spectrogram and the measured electric field of the reference pulse were used as input for an XFROG inversion algorithm (Femtosoft Technologies FROG3) to retrieve the electric field of the UV shaped pulses. The thinness of the DFG crystal rendered unnecessary the correction of the FROG traces by convolution of the reference and shaped pulse spectra. The FROG errors, a measure of the accuracy of the phase retrieval process used in the FROG algorithm, were 2 % or less for all the electric field retrievals displayed in the next section.

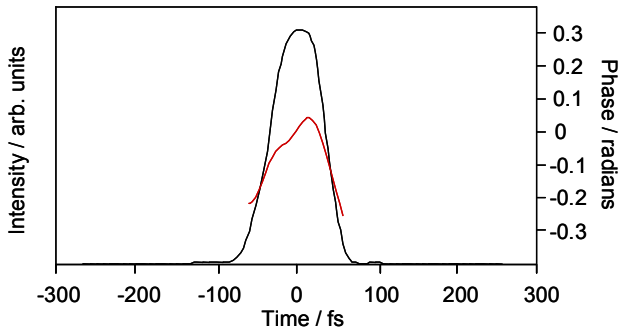

Figure 2.13 Example of a temporal electric field intensity (*black*) and phase (*red*) of the reference pulse at 795 nm, as measured by the GRENOUILLE retrieved by the VideoFrog software. This retrieval shows a small positive chirp in the pulse.

2.6 Results from the UV pulse shaper

To illustrate the capability of the pulse shaping setup, several useful phase modulations generating pulse trains at varying times and wavelengths have been measured and are presented here. Here, both XFROG[32] traces (spectrograms) of the up-converted pulses, and the analytic descriptions of the electric fields of the shaped UV laser pulses, which were obtained from electric field retrievals, are presented. For weak field coherent control experiments, the types of pulse shapes that might be necessary are trains of pulses with the same wavelength but carefully timed to cause optimal constructive or destructive interference or trains of different wavelengths to excite different modes at well-defined time intervals.

Pulse replicas in the time domain can be produced by applying a π phase 'comb' to the pulse in the frequency domain, this is achieved by producing alternating groups of pixels with 0 and π phase, respectively. Fig. 2.14 shows four such pulse replicas with pulse separations, τ, of (a) 530 fs, (b) 760 fs, (c) 1600 fs and (d) 2230 fs produced by comb spoke widths of 21, 15, 7 and 5 SLM pixels, respectively. The raw XFROG traces can be seen in the bottom row of Fig. 2.14, above them is the time-domain electric field

intensity (black) and phase (red) and at the top of the figure, the spectral electric field intensity (black) and phase (red).

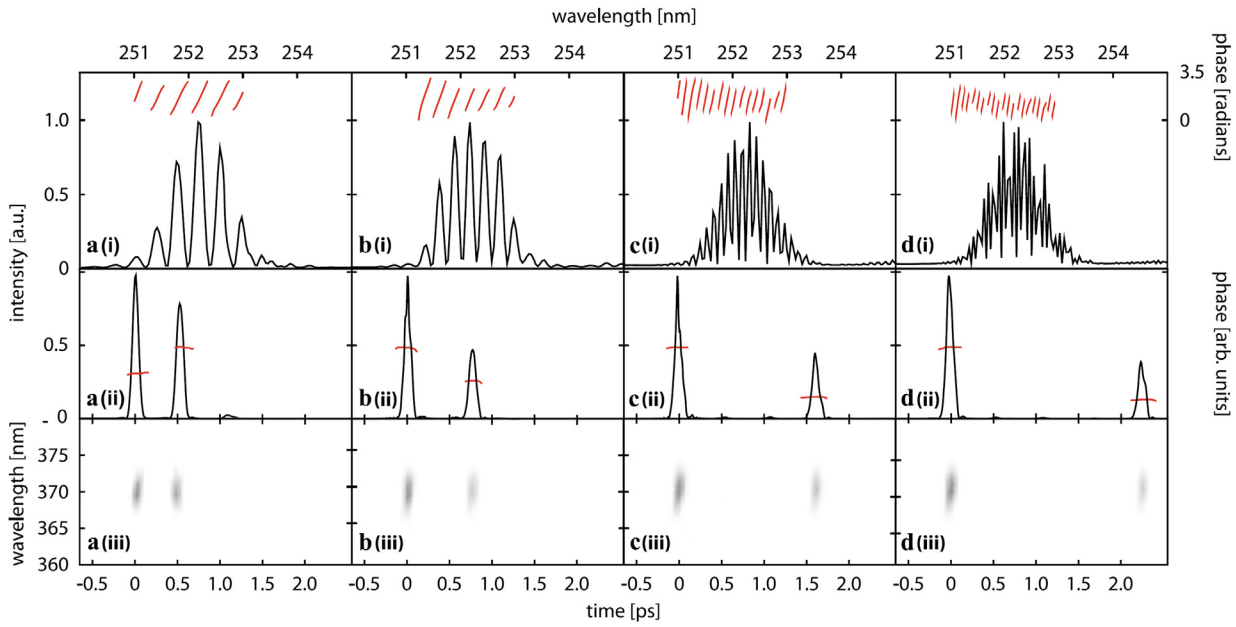

Figure 2.14 Pairs of pulses in the time domain generated from combs of alternating 0 and π phase. Each figure shows a raw XFROG trace (iii), the reconstructed temporal electric field intensity of the UV pulse (*black*) and phase (*red*) (ii) and reconstructed spectral intensity (*black*) and phase (*red*) (i) of the UV pulse. Figure reprinted from Ref. 1.

The applied comb phase function creates holes in the spectrum, due to interference, at the points where the phase changes abruptly, and the overall result is a squared-comb spectrum. In the frequency domain this corresponds to a set of pulse replicas composed of two main central peaks and outer satellite peaks, all equally spaced. In the case of SHG Type I and assuming a thin crystal, hence also assuming phase matching over the complete bandwidth and a non-depleted fundamental electric field, E_f, the second harmonic field, E_{SHG}, is given by[12]

$$E_{SHG}(t) \propto E_f^2(t). \tag{2.23}$$

In the frequency domain the electric field is convoluted with itself to give the up-converted field:

$$E_{SHG}(\omega_{SHG}) \propto \int E_f(\omega_f) E_f(\omega_{SHG} - \omega_f) d\omega_f . \quad (2.24)$$

Thus, it is trivial to predict the effect of doubling on the pulse shapes using either Eq. 2.23 or Eq. 2.24. The spectral square comb in the visible is smoothed by the doubling process (Eq. 2.24), and so the set of pulse replicas in the UV becomes a pulse pair, with the smaller outer pulses reduced to less than 5% of the intensity of the main pulses. In some of this data, the outer smaller satellite peaks may be seen. For example, in Fig. 2.14a (ii) a sub-pulse at 1.1 ps, is clearly visible. The measured pulse separation times, τ, allow us to calibrate the wavelengths on the spatial light modulator (SLM) pixels using the uncertainty principle relationship, $\tau = 1/P$, where P is the width of the programmed comb spoke on the SLM, in units of frequency, so that the comb widths on the SLM are 1.62, 1.13, 0.54 and 0.39 nm across the comb spokes for Fig. 2.14a–d, respectively. This effect is illustrated in Fig. 2.15, and provides an accurate measurement of the angular dispersion in the pulse shaper. Other points to note are that the temporal phase is flat, and the temporal duration of each of the replicas is similar. The difference in intensity between the two subpulses is due to the contribution of the small amount of dead space between the pixels to the pulse formed from the pixel programmed to 0 phase. The decreasing ratio of the heights of the two pulses with increasing comb width is also explained as a pixellation effect. The retrieved spectral phase is linear over each of the "teeth" in the spectral comb. This is predicted by Eq. 2.24, from which it can be seen that the convolution of the spectral electric field produces a new field with a phase that is independent of the SLM modulation, because the modulation factor $e^{i\pi}$ is a real number.

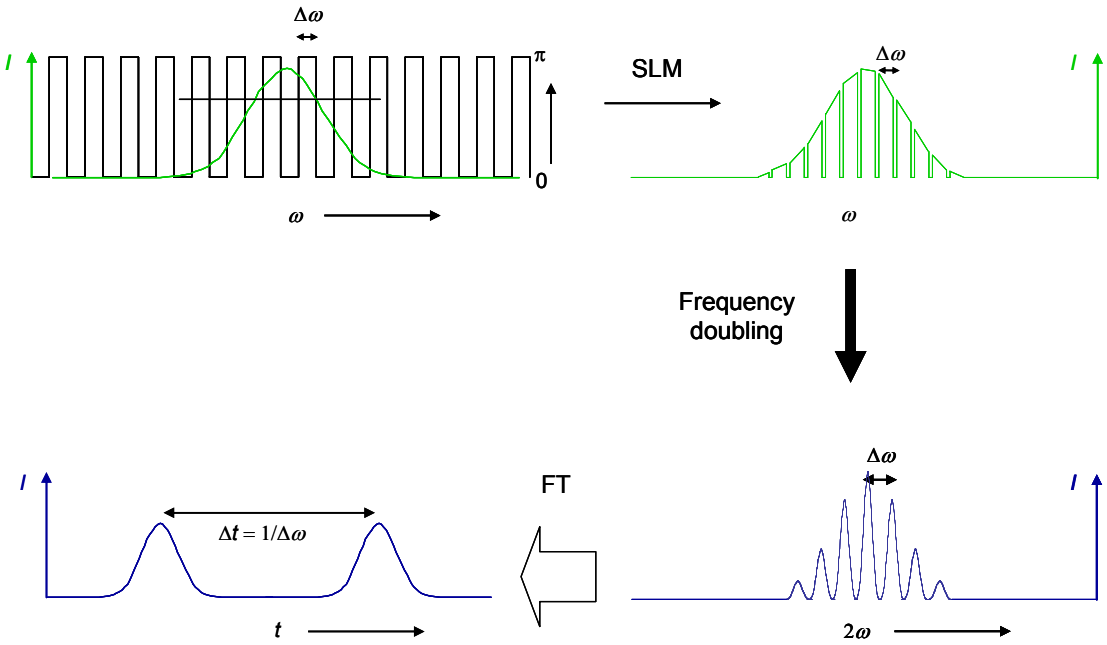

Figure 2.15 Illustration of the effect of a π phase comb on the visible and UV pulses. Clockwise from top left: the Gaussian input pulse has a flat phase to which is added a phase comb with adjacent sets of pixels set to zero or π; this creates destructive interference between the adjacent frequencies with 0 and π phases; frequency doubling of the pulse creates almost sinusoidal frequency fringes; the Fourier transform of this is a pair of pulses with a separation time that is the reciprocal of the frequency comb width as originally added to the visible pulse.

In another scheme (Fig. 2.16), a pair of pulses were created, each with a different central frequency, by applying a triangular phase mask to the SLM (Fig. 2.16a). The results are shown in Fig. 2.16b–d. The raw XFROG traces can be seen in Fig. 2.16d, the time-domain electric field intensity (black) and phase (red) are in Fig. 2.16b, and the spectral electric field intensity (black) and phase (red) are in Fig. 2.16c. The temporal separation of the pulses is determined by the difference in the group delays, τ_{group}, of the two pulses, which is defined by the difference in slopes of the two applied linear spectral phases ($\tau_{group} = -d\phi(\omega)/d\omega$, as in Eq. 1.15). The two peaks are separated by 650 fs in the time domain (Fig. 2.16b). The pulse at 650 fs has a central wavelength of 253.6 nm and is separated from the larger peak at 254.6 nm by 1 nm (Fig. 2.16c). The retrieved electric fields of these two pulses are also shown in Fig. 2.16. The retrieved spectral

phase shows a clear change in slope at the central frequency of the spectrum, 254 nm, as programmed on the pulse shaper at the fundamental frequency, 508 nm. The frequency doubling process was most efficient at a slightly off-centred wavelength, around 254.6 nm, and thus the retrieved temporal intensity profile shows a bias towards the sub-pulse at this wavelength. This means that the up-converted spectrum is centred at 254.6 nm, and the retrieval algorithm has centred the retrieved electric field at the central wavelength and time of the stronger sub-pulse in the trace. Hence the slope of one of the spectral phases in the retrieved electric field is flat, corresponding to zero time delay, and one of the temporal phases of the two sub-pulses is flat, corresponding to zero wavelength shift from the new centre wavelength, 254.6 nm; thus, the spectral and temporal phases of the other sub-pulse show increases in the magnitude of the slope (larger group delay and spectral shifts, respectively), as would be expected. The time separation of the two pulses is predicted to be 665 fs, as calculated from the SLM phase mask function and the measured spectral dispersion. This is 15 fs greater than the observed experimental value, a discrepancy that is well within the error of the experiment.

The effect of SHG has been modelled using the thin crystal approximation (Eq. 2.23) after first Fourier transforming a model electric field consisting of a Gaussian amplitude and the phase applied to the SLM. After a second Fourier transform back to the frequency domain, the electric field $E_{SHG}(\omega_{SHG})$ is given. This is plotted in Fig. 2.17 for the "triangular" phase that was applied to the SLM to give the experimental data in Fig. 2.16.

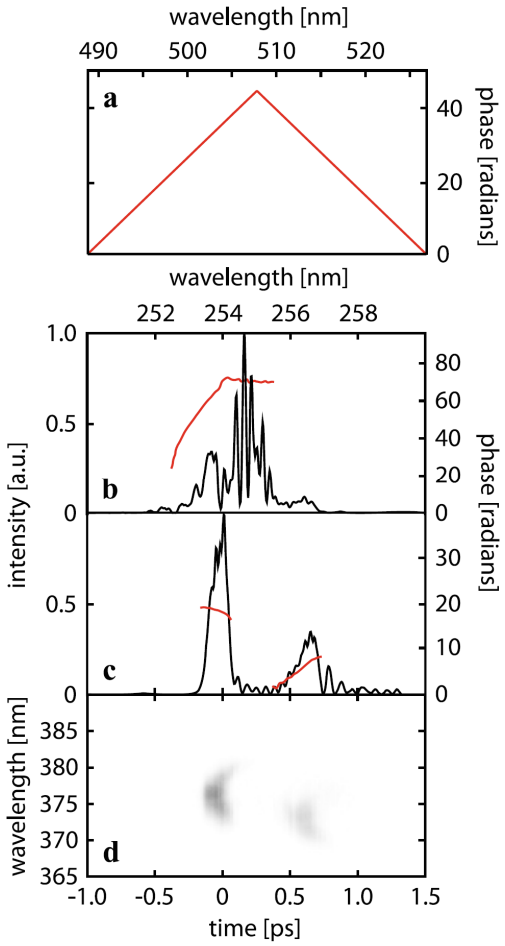

Figure 2.16 Pairs of pulses with different central wavelengths generated from a triangular phase mask. (**a**) "Triangular" phase mask applied by the SLM in the visible. (**b**) Spectral intensity (*black*) and phase (*red*) showing the central wavelengths of the UV pulses. (**c**) Time-domain electric field intensity (*black*) and phase (*red*) of the UV pulse showing two distinct sub-pulses. (**d**) Raw XFROG trace. Figure reprinted from Ref. 1.

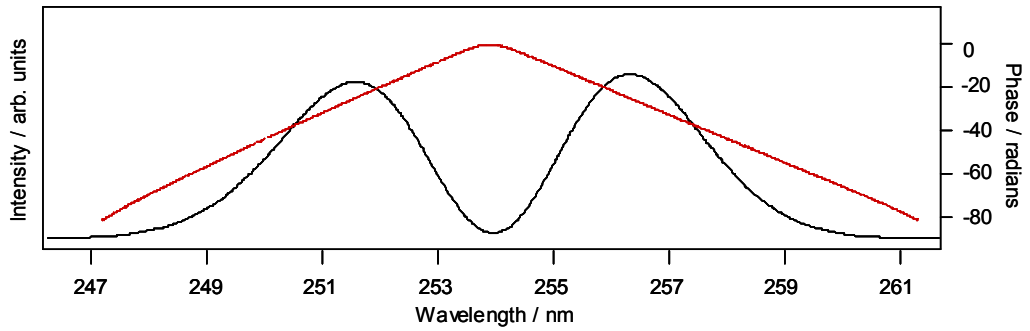

Figure 2.17 Model spectral electric field intensity (*black*) and phase (*red*) calculated using the thin crystal approximation (see text for details).

At first glance, a comparison of the spectral intensities in Fig. 2.17 and Fig. 2.16b does not show very good agreement. There is, however, a definite dip in intensity in the experimental retrieved spectrum at 254 nm. As already mentioned, the phase in Fig. 2.17 shows good qualitative agreement with the experiment in that the pulse separation time is well-predicted. Also, the FROG trace clearly shows the spectral separation of the two peaks (Fig. 2.16d), and so the irregularities in the shape of the retrieved spectral intensity from the experiment in Fig. 2.16b may be caused by the effect of the retrieval algorithm on the fairly high level of noise in the FROG trace.

In the final pulse shape scheme, shown in Fig. 2.18, a sine wave phase function is applied to the SLM, of amplitude 4 radians, and with 34 oscillations across the 640 pixels. The number of oscillations of the sine wave applied to the phase mask defines the temporal separation of the peaks in the pulse train produced. The amplitude of the phase modulation determines the relative heights of the pulse-train peaks. Here five pulses at −610, 0, 610 (very faint), 1220 and 1830 fs are produced, as shown in Fig. 2.18. The raw XFROG traces are shown in Fig. 2.18c, above them is the time-domain electric field intensity (black) and phase (red) and at the top of the figure, in Fig. 2.18a, the spectral electric field intensity (black) and phase (red), in Fig. 2.18b. In the time domain each peak has a Gaussian profile with a flat phase over each peak. The spectral

phase shows a regular oscillatory structure with several large jumps most likely due to the non-zero spectral intensity.

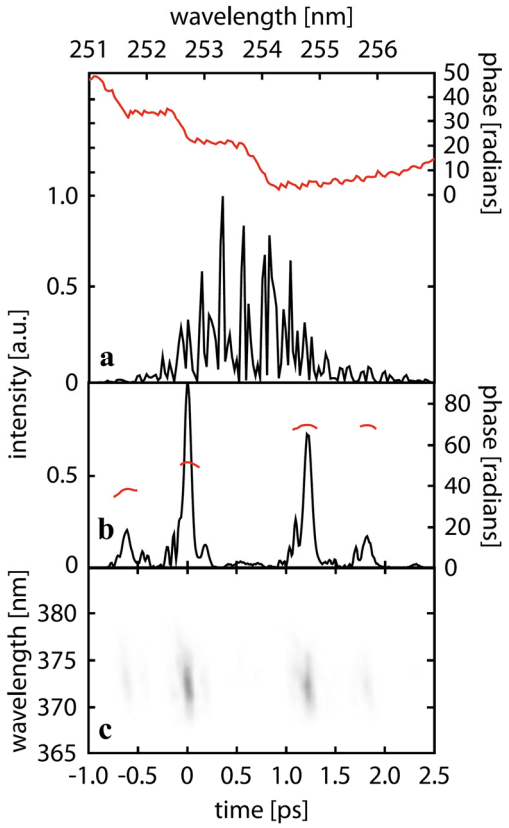

Figure 2.18 Pulse trains in the time domain generated from a sinusoidal phase mask. (**a**) The spectral phase (*red*) and intensity (*black*) of UV pulse. (**b**) Temporal electric field intensity (*black*) and phase (*red*) of the UV pulse. (**c**) Raw XFROG trace. Figure reprinted from Ref. 1.

Fig. 2.19 shows a model SHG temporal intensity for a fundamental with a starting Gaussian spectral amplitude and a spectral phase as programmed on the SLM for the data in Fig. 2.18. The model data was obtained as for Fig. 2.17, using the thin crystal approximation (Eq. 2.23). Figs. 2.18b and 2.19 show good agreement. As observed experimentally, the model temporal phase is flat over each of the pulses in the train.

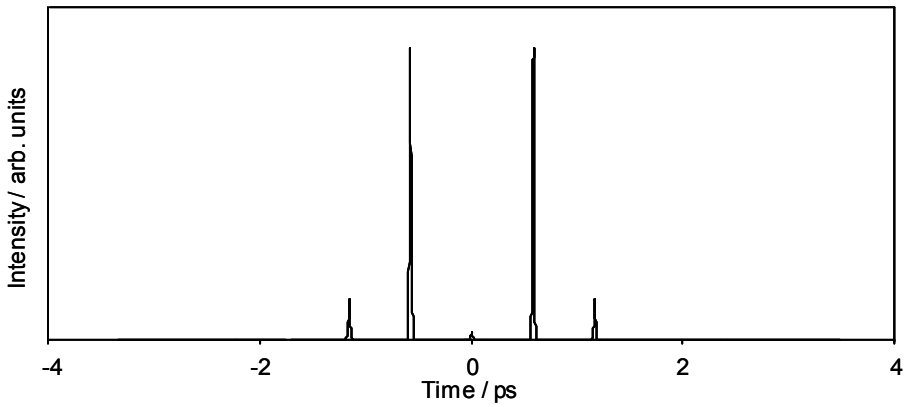

Figure 2.19 Model temporal SHG intensity for a fundamental pulse with a sinusoidal phase the same as the experimental data shown in Fig. 2.18. The thin crystal approximation was used to obtain these model data.

2.7 Further work

The results presented in Section 2.6 demonstrate that shaped light in the deep UV may be generated effectively by frequency doubling the output of a folded 4*f* spatial light modulator (SLM) setup. Using the output of an optical parametric amplifier (OPA) as input for a pulse shaper allows the central frequency of the shaped UV pulse to be tuned, which is potentially useful for coherent control experiments, where the photon energies are of significance as well as their relative phases and amplitudes. In such experiments, the details of the pulse shapes required are not always *a priori* knowledge, but often require feedback from an experiment and hence the utility of flexible SLM pulse shaping. The results presented in this chapter were several pulse shapes produced in the UV with varying pulse separations and central frequencies. Interestingly, the full characterisations and retrieved cross-correlation frequency-resolved optical gating (XFROG) traces highlight that phase information is being transferred through the Type I second harmonic generation (SHG) process for some of the pulse shapes shown here. To investigate this effect further, XFROG traces of the beam in the visible, before the SHG process, as well as afterwards, would directly record the effect of up-conversion on the spectral phase within a Type I SHG process. Although it has not been shown here,

the experimental setup could easily be adapted by adding a genetic algorithm with feedback from the spectrogram to achieve the exact pulse shape desired irrespective of phase distortions in the input pulse or those caused by alignment. The closely spaced pairs (or longer sequences) of pulses centred at different central wavelengths could prove a valuable tool for controlling the nuclear dynamics of the excited electronic states of photochemical species.

In Chapter 4, time-resolved photoelectron spectroscopy of the styrene molecule is described, and in Chapter 3 the means to carry out quantum chemical calculations on the excited potential energy surfaces of styrene is investigated. An obvious application of the work in this chapter would be to use the pulse shaper to control the photodynamics of styrene, using a pulse shape such as the one shown in Fig. 2.16. In a pulse shape of this type, the frequencies and times of the individual subpulses could be selected from knowledge of the potential energy surface of styrene obtained from electronic structure calculations. Alternatively, the pulse shaper could be used to control the photochemistry of styrene by a method like one of the classic optimal coherent control experiments: the optimisation of the pulse shape on the SLM would be carried out in a closed-loop with feedback from a photoelectron imaging spectrometer to allow the genetic algorithm, or evolutionary strategy to reach the optimum pulse shape. This experiment could also require considerable theoretical input, however, because determining a suitable feedback signal from the photoelectron spectra would require a very precise understanding of the photoelectron spectra as a function of time.

The time required to record an XFROG trace is on the order of minutes, and is dependent on the complexity and duration of the pulse. For many applications, the low resulting pulse energy associated with this UV shaping method would be a drawback. However, our goal is to carry out a weak-field control experiment, in which the pulse energy need be sufficient only to excite a molecule from the ground electronic state. One issue that has not been studied here is that of spatio-temporal coupling in the pulse shaper device. In a precisely-aligned pulse shaper with an input beam that is not at all

spatially chirped, there should be very little spatial distortion of the pulse. Indeed, the folded near-Littrow arrangement was chosen to minimise chromatic aberrations from the cylindrical mirrors. In this experiment, the amount of spatial chirp on the input visible pulse from the OPA is unknown, and the number of optics and the path distances in the OPAs is quite large, and so it is likely that some spatial chirp is present in the pulse before it enters the pulse shaper; this is not an issue that would have affected the results of other UV pulse shaping experiments, most of which involved shaping directly the output of an amplifier[11,12,14] rather than an OPA. The quality of the OPA output undoubtedly affected the present results to some extent, but as already discussed, the difference between the model and experimental results in most cases is small.

References

1 Figures 1-4 and excerpts with kind permission from Springer Science+Business Media: D. S. N. Parker, A. D. G. Nunn, R. S. Minns *et al.*, Applied Physics B-Lasers and Optics 94 (2), 181 (2009), copyright Springer-Verlag 2008.

2 H. H. Fielding and A. D. G. Nunn, *Femtochemistry and the control of chemical reactivity*, in *Tutorials in molecular reaction dynamics*, edited by M. Brouard and C. Vallance (RSC, to be published 2010).

3 P. M. W. French, Reports on Progress in Physics 58 (2), 169 (1995).

4 E. Hecht, *Optics* (Pearson Education, 4th Edition, 2003).

5 A. Assion, T. Baumert, M. Bergt *et al.*, Science 282 (5390), 919 (1998).

6 R. J. Levis, G. M. Menkir, and H. Rabitz, Science 292 (5517), 709 (2001).

7 M. Hacker, G. Stobrawa, R. Sauerbrey *et al.*, Applied Physics B-Lasers and Optics 76 (6), 711 (2003).

8 B. J. Pearson and T. C. Weinacht, Optics Express 15, 4385 (2007).

9 A. Monmayrant, A. Arbouet, B. Girard *et al.*, Applied Physics B-Lasers and Optics 81 (2-3), 177 (2005); F. Verluise, V. Laude, Z. Cheng *et al.*, Optics Letters 25 (8), 575 (2000); A. M. Weiner, Review of Scientific Instruments 71 (5), 1929 (2000).

10 K. Hazu, T. Sekikawa, and M. Yamashita, Optics Letters 32 (22), 3318 (2007).

11 P. Nuernberger, G. Vogt, R. Selle *et al.*, Applied Physics B-Lasers and Optics 88 (4), 519 (2007).

12 M. Hacker, R. Netz, M. Roth *et al.*, Applied Physics B-Lasers and Optics 73 (3), 273 (2001).

13 M. Hacker, T. Feurer, R. Sauerbrey *et al.*, Journal of the Optical Society of America B-Optical Physics 18 (6), 866 (2001); S. Shimizu, Y. Nabekawa, M. Obara *et al.*, Optics Express 13 (17), 6345 (2005).

14 C. Schriever, S. Lochbrunner, M. Optiz *et al.*, Optics Letters 31 (4), 543 (2006).

15 H. F. Wang and A. M. Weiner, IEEE Journal of Quantum Electronics 40 (7), 937 (2004).

16 A. Monmayrant, S. Weber, and B. Chatel, Journal of Physics B, (to be published).

17 A. Monmayrant, and B. Chatel, Private communication (2006).

18 J. Vaughan, *Ultrafast Pulse Shaping* in *Ultrafast Optics Textbook*, edited by R. Trebino and J. Squier (2008), available at http://www.physics.gatech.edu/frog/ultratext.html.

19 C. Iaconis and I. A. Walmsley, IEEE Journal of Quantum Electronics 35 (4), 501 (1999).

20 R. Trebino, *Frequency-resolved Optical Gating: The Measurement of Ultrashort Laser* (Kluwer Academic Publishers, 2000).

21 V. V. Lozovoy, I. Pastirk, and M. Dantus, Optics Letters 29 (7), 775 (2004).

22 C. Iaconis and I. A. Walmsley, Optics Letters 23 (10), 792 (1998).

23 I. A. Walmsley, in *Few-Cycle Laser Pulse Generation and Its Applications* (2004), Vol. 95, pp. 265.

24 D. J. Kane and R. Trebino, IEEE Journal of Quantum Electronics 29 (2), 571 (1993).

25 J. L. Herek, W. Wohlleben, R. J. Cogdell *et al.*, Nature 417 (6888), 533 (2002); S. H. Lee, K. H. Jung, J. H. Sung *et al.*, Journal of Chemical Physics 117 (21), 9858 (2002); S. Vajda, P. Rosendo-Francisco, C. Kaposta *et al.*, presented at the 10th

International Symposium on Small Particles and Inorganic Clusters (ISSPIC 10), Atlanta, Georgia, 2000 (unpublished).

26 C. Dorrer, Optics Letters 24 (21), 1532 (1999).

27 P. Baum, S. Lochbrunner, and E. Riedle, Optics Letters 29 (2), 210 (2004).

28 C. Dorrer, P. Londero, and I. A. Walmsley, Optics Letters 26 (19), 1510 (2001).

29 P. Londero, M. E. Anderson, C. Radzewicz *et al.*, Journal of Modern Optics 50 (2), 179 (2003).

30 P. O'Shea, S. Akturk, M. Kimmel *et al.*, Applied Physics B-Lasers and Optics 79 (6), 683 (2004).

31 R Trebino, Private communication (2006).

32 S. Linden, J. Kuhl, and H. Giessen, Optics Letters 24 (8), 569 (1999).

33 D. J. Kane and R. Trebino, Optics Letters 18 (10), 823 (1993).

34 K. Michelmann, T. Feurer, R. Fernsler *et al.*, Applied Physics B-Lasers and Optics 63 (5), 485 (1996).

35 R. Trebino, K. W. DeLong, D. N. Fittinghoff *et al.*, Review of Scientific Instruments 68 (9), 3277 (1997).

36 S. Backus, J. Peatross, Z. Zeek *et al.*, Optics Letters 21 (9), 665 (1996).

37 J. N. Sweetser, D. N. Fittinghoff, and R. Trebino, Optics Letters 22 (8), 519 (1997).

38 D. Lee, S. Akturk, P. Gabolde *et al.*, Optics Express 15 (2), 760 (2007).

39 D. N. Fittinghoff, J. L. Bowie, J. N. Sweetser *et al.*, Optics Letters 21 (12), 884 (1996).

40 J. M. Dudley, S. F. Boussen, D. M. J. Cameron *et al.*, Applied Optics 38 (15), 3308 (1999).

41 J. M. Dudley, M. D. Thomson, F. Gutty *et al.*, Electronics Letters 35 (23), 2042 (1999); F. Gutty, S. Pitois, P. Grelu *et al.*, Optics Letters 24 (20), 1389 (1999).

Chapter 3

Electronic structure modelling of the singlet states of styrene in the Franck-Condon region

This chapter is an investigation of the character of the excited electronic states of the styrene molecule in the Franck-Condon region. It is hoped that the calculations presented in this chapter will provide a basis for the further investigation of other parts of the excited potential energy surfaces of styrene, with a view to understanding the dynamics of photoexcited styrene in experiments such as the time-resolved photoelectron spectroscopy experiment presented in Chapter 4. With this aim in view, the lowest three singlet excited states have been studied using *ab initio* electronic structure methods for which analytical gradients are available, to try to find a theoretical methodology that results in a balanced description of the three states. This chapter begins with a review of the literature on the electronic spectroscopy and theoretical electronic structure of styrene, in Section 3.1. This is followed by a description of some general methods of calculation of excited state electronic structure in Section 3.2. The *ab initio* approach chosen to study the electronic structure of S_1, S_2 and S_3 styrene in this work is explained in Section 3.3, and the results presented and discussed in Section 3.4. In Section 3.5, approximate Koopmans' correlations between the excited states and the electronic states of the cation are analysed using TDDFT calculations; the purpose of this is to aid the assignment of energy bands in the time-resolved photoelectron spectra that are presented in Chapter 4 of this thesis. Some conclusions about the calculations performed in this chapter are given in Section 3.6. Parts of this chapter and Chapter 4 are currently being edited for publication.[1]

3.1 The electronic and vibronic spectroscopy of styrene in the literature

The electronic spectroscopy of styrene has been studied by many methods. The molecule is small enough to be a good test case for fairly high-level *ab initio* calculations. Styrene is a model for aromatic alkene isomerisation because it is the simplest system involving coupling between ethene and benzene states. It is also a prototype for the more complex photophysics and photoisomerisation of stilbene. Although the band origins and much vibrational structure of the first two electronic states are well known, there remains some dispute over the character of the S_2 and higher electronic states. In what follows, an outline of the current knowledge of styrene, both from spectroscopy and theory in the literature, is given.

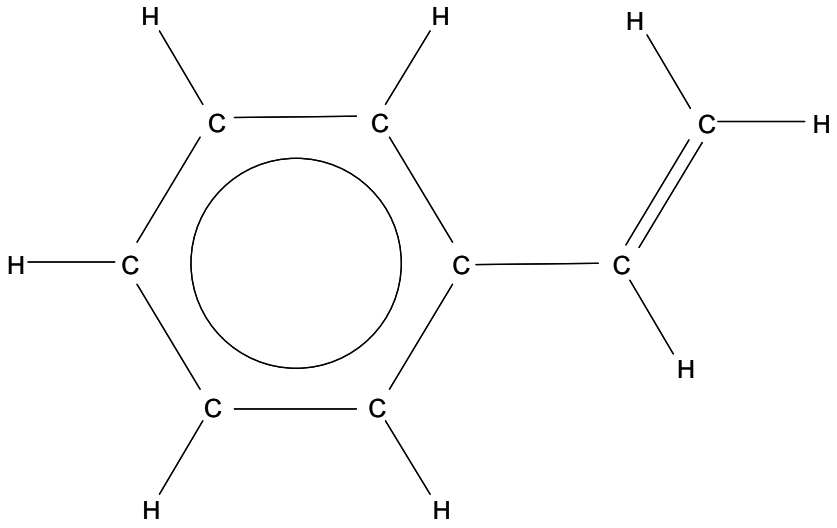

Figure 3.1 Styrene (not to scale).

Vertical excitations in the Franck-Condon region and vibronic structure

Styrene, C_8H_8, see Fig. 3.1, is a substituted benzene and has been studied as such,[2-4] with its spectroscopy and electronic structure viewed as a perturbation of that of benzene. At the other extreme, some theoretical studies of the electronic spectroscopy of styrene, and the closely related molecule stilbene, have resulted in a description of their excited states

that is based on those of the ethylene molecule.[5] Whilst it is certain that the electronic states of styrene are not exactly the same as those of either benzene or ethylene, some of its electronic states may bear close resemblance to states of these individual components.

The valence excited electronic states of benzene can be described by excitations between the π and π* molecular orbitals (MOs) produced by Hückel theory. The form of the MOs is well known: there are a doubly-degenerate pair of e_{1u} orbitals that form the highest occupied molecular orbitals (HOMOs) and another pair that are the lowest unoccupied molecular orbitals (LUMOs) with e_{2g} symmetry, in the D_{6h} point group. The excited electronic states that result from the one-photon excitations between the HOMOs and LUMOs are of symmetries B_{1u}, B_{2u}, and E_{1u}, singlets and triplets. Transitions to the $^1B_{1u}$ and $^1B_{2u}$ states are formally forbidden, but allowed by vibronic coupling. The lowest energy state is a $^1B_{2u}$ state, followed by a $^1B_{1u}$ and finally, a bright $^1E_{1u}$ state. These states in benzene itself and also in molecules that are benzene derivatives are often labelled using Platt notation, in which the electronic states arise from a particle on a ring model for the electrons.[6] In this notation, the lowest state is the ^1L_b, followed by the ^1L_a state and then the $^1B_{a,b}$ states. L corresponds to a total angular momentum of $2n + 2$, where $n = 1$ for a benzene ring, and B to an angular momentum of 1. The subscripts a and b refer to the polarisation pattern relative to the ground state around the ring for that state: a is polarised alternately on each of the carbon centres, and b is polarised alternately between the centres. In ethylene, the excited electronic states are often labelled using Mulliken notation.[7] The ground state is labelled N, and the first excited singlet state, arising from a single excitation between the $2p$ π orbitals, has symmetry label B_{1u} and Mulliken label V. The higher excited singlet state is a doubly excited state, consisting of a full π* orbital and an empty π orbital. In the minimum valence only basis set model, both the first and second excited singlet states of ethylene have ionic valence bond character: they are the positive and negative combinations of the two valence bond structures that have both electrons localised on an individual p orbital on one of each of the carbon atoms. Rydberg-type excitations beyond the valence MOs

also feature in the electronic spectrum of ethylene,[8] as for many other organic molecules, but the oscillator strengths for transitions to Rydberg states are always small.

The gas-phase ultraviolet absorption spectrum of styrene in the region up to about 7 eV consists of three main bands. A spectrum recorded by Philis *et al.*[9] is reproduced in Fig. 3.2. Historically, there was some debate over the electronic state origin of the second band, with most early studies assuming that it contained contributions from the excitations to both S_2 and S_3.[10,11] However, due to the good agreement with high level *ab initio* calculations, it is now generally accepted that the first two bands arise from the two lowest singlet electronic states, S_1 and S_2 respectively, as labelled in Fig. 3.2 and that these two states both arise from excitations within the valence π and π^* molecular orbitals.[12,13]

S_1 vertical state

All of the recent theoretical and experimental studies are in agreement over the character of the first excited singlet in styrene: the state is basically localised on the benzene ring and correlates with the S_1 state in benzene. In valence bond (VB) terms, this state is predicted to be covalent.[2] The low intensity of the first absorption band supports this prediction. Experimentally, the transition to the origin of this state has been determined as 4.31 eV by high resolution absorption spectroscopy.[14] There have been a considerable number of published studies on the vibrational structure of the first excited state of styrene, both experimental[15-19] and theoretical[20,21] all of which analyse the excited state vibrations in terms of modes with similar frequencies in the ground state. Many vibronic features have been unambiguously assigned, including fundamentals, combination bands and hot bands, which can be compared with those of the ground state measured *via* single vibrational level fluorescence.[17,18] Some mixing of modes upon excitation to the S_1 state was observed as Duschinsky mixing,[18] an important effect for low symmetry molecules such as styrene (C_s point group) where there are a large number of vibrations of the same symmetry species that can mix.[22] Franck-Condon

simulations together with electronic structure modelling of the S_1 minimum reproduces almost all of the vibrational structure and the earlier experimental assignments.[21]

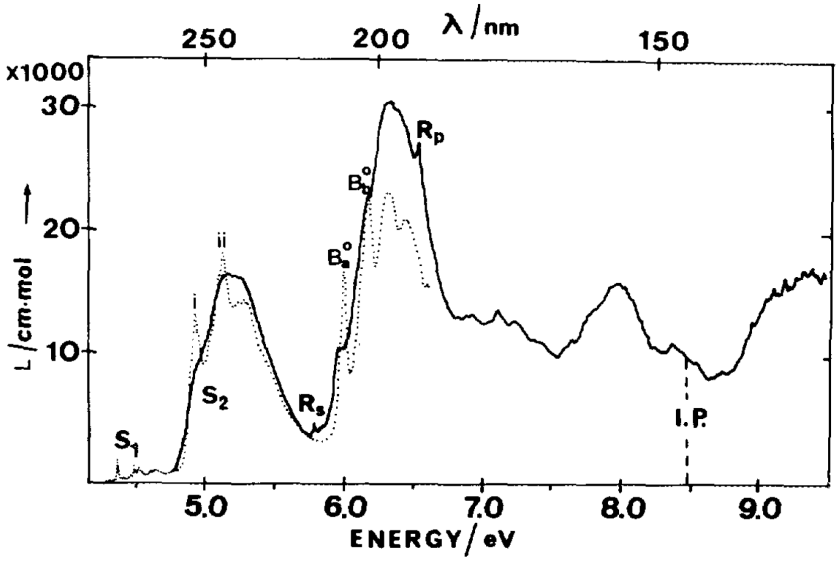

Figure 3.2 Room temperature absorption spectrum of styrene in the gas phase (solid line), and scaled absorption spectrum of argon matrix isolated styrene (dotted line). Three main peaks are of interest, centred at about 280 nm (4.43 eV), 238 nm (5.21 eV) and 196 nm (6.37 eV). Figure reprinted from J. G. Philis, A. Ioannidou, and A. A. Christodoulides, Journal of Molecular Spectroscopy 174 (1), 51 (1995), copyright 1995 and as referenced therein, from K. Kesper, N. Münzel, W. Pietzuch *et al.*, Journal of Molecular Structure: THEOCHEM 200, 675 (1989), copyright 1989, with permission from Elsevier

S_2 vertical state

The electronic character of the S_2 state is less well established than that of the S_1 state, and much less detail is known about its vibrational structure. Jet-cooled UV absorption by Leopold *et al.* established the origin of the state at 4.88 eV above the origin of the ground state.[23] In the same study, two vibrational progressions were observed in this state, corresponding to modes with frequencies 1577 cm^{-1} and 248 cm^{-1}. Initially the 1577 cm^{-1} mode was assigned to the ethylenic stretch; however, after further investigations this mode was assigned to υ_9' which is a mixture of carbon-carbon

stretches in the ring and on the ethylenic bond.[24,25] The 248 cm^{-1} band was assigned to the υ'_{29} mode, an in-plane delocalised bend mixture. On the basis of a later resonance Raman study, it was suggested that these assignments in S_2 could be altered to include some other modes in place of the progression in υ'_{29}.[11]

An early CASSCF theoretical treatment of styrene by Bearpark *et al.* concluded that the second excited singlet state is a covalent state in which the component ethylenic and benzenic parts are both triplet spin coupled. The same study found that the third excited state was ionic. Recent CASSCF, CASPT2 and SAC-CI *ab initio* electronic structure theoretical studies have been published that conclude that the second singlet state is described approximately by a single transition between a HOMO and a LUMO that resemble those of the ground state wavefunction, where the LUMO is antibonding with respect to the HOMO on both the benzene and the ethylene components of the molecule.[12,13,26] The identification of the principal vibrational progression in the S_2 state as arising from a normal mode with significant ethylenic and benzenic character is in agreement with the electronic structure suggested by Bearpark *et al*. However, one of the recent studies, significant oscillator strengths are also calculated for this state, and the state energy is demonstrated to be highly dependent on the degree of correlation energy included in the calculation,[12] both of which lead to the conclusion that this state is an ionic VB state, in contrast to the study of Bearpark *et al.* The conclusion of Amatatsu is that this state resembles the ionic *V* state of ethylene.[26] The differences in the theoretical results of the CASSCF study and the more highly correlated methods are not unexpected because the energy of ionic states is well-known to be highly dependent on the level of dynamic correlation in the theoretical method.

S_3 vertical state

Identification of the states contributing to the third band is not yet conclusive, and has received less attention than the S_1 or S_2 states. It has been suggested that more than one electronic state may be present in the absorption intensity of this band. In their CASPT2 study, Molina *et al.* located two valence excitations in the energy region of the third

band, at 6.19 and 6.30 eV vertical excitation energy, both with significant oscillator strength.[12] These states were labelled adiabatically, according to their results, as S_5 and S_6, and they predict the S_3 (Rydberg 3s) and S_4 states at 5.85 eV and 6.09 eV as having very little oscillator strength.

Rydberg states

Rydberg excitations, that is excitations to states not described by the valence orbitals, by nature have very small absorption coefficients. However, in some molecules the Rydberg states play a crucial role in photochemistry. Excitations to $n = 3$ Rydberg states have been reported in the UV absorption spectrum of styrene and in REMPI spectra by Philis *et al.*[9] The position of these states agrees quite well with the recent theoretical work by Molina *et al.*,[12] which predicts a 3s Rydberg state at 5.85 eV, close to the assignment of a small peak in the absorption spectrum by Philis *et al.* at 5.799 eV, labelled in Fig. 3.2 as R_s. The assignment of this state is tentative because further REMPI experiments were not able to detect it.[27] These REMPI experiments were able to locate the three 3*p* Rydberg states at 6.259, 6.456 and 6.528 eV, and they were assigned to the $3p_y$, $3p_x$ and $3p_z$ states respectively, using the theoretical results of Molina *et al.* as a guide; lower limits for the lifetimes of these states estimated from the bandwidths were 91 fs, 38 fs and 165 fs respectively.[9,27] The $3p_z$ state is marked R_p on Fig. 3.2.

Theoretical studies of the singlet states

In the publication by Bearpark *et al.*, the authors reported that they were able to order the states according to their VB character from their MCSCF theory results.[2] At this level of theory, the S_1 state was identified as benzene-localised, essentially equivalent to the S_1 state in benzene, the S_2 state they identified as a mixture of excited benzene and excited ethylene, and the S_3 state was identified as an ethylene localised zwitterionic state. These VB structures are shown in Fig. 3.3. Vertical excitation energies of 4.76, 6.49 and 7.35 eV were obtained for the S_1, S_2 and S_3 states respectively, calculated at the CASSCF(8,8)/6-31G* level, with the active space consisting of all the π valence orbitals

and electrons. However, the authors also state that another calculation using diffuse functions in the basis set (using 6-31+G*) makes the S_2 and S_3 ionic state almost degenerate, and they predict that with more dynamic correlation included in the calculation method, the covalent S_2 and the ionic S_3 states would probably be reversed in their energy ordering. As already discussed, the ionic character of the state adiabatically labelled S_2 in the Franck-Condon region seems to have been observed in subsequent calculations by several other groups,[12,13,28] Although Amatatsu states explicitly that the S_2 state is ethylenic,[29] this is not fully justified by the spectroscopic evidence, for example, as already mentioned, Hemley *et al.*[25] identified that a highly active mode in S_2 is as a mixture of ethylene and benzene ring C=C stretches (as well as smaller bend components).

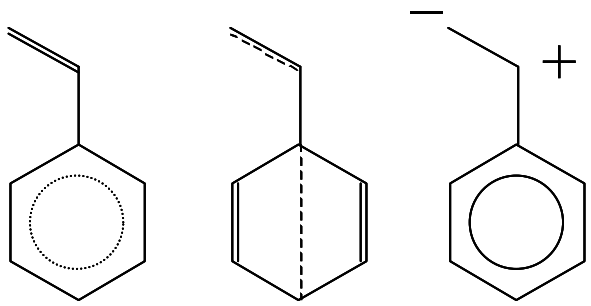

Figure 3.3 The electronic structures of styrene in the Franck-Condon region as determined by Bearpark *et al.*[2] From left to right: S_1, S_2 and S_3. S_1 is an excitation localised to benzene, S_2 is singlet-coupled triplet Dewar benzene and triplet ethylene, and S_3 has an ionic ethylene VB structure. Singlet coupling is indicated by solid lines and triplet coupling by dashed lines.

The recent theoretical results using highly correlated methods[12,13] provide a benchmark by which the electronic structure methods used for the results presented in this thesis may be tested. The energies obtained in these studies for the S_1 and S_2 states agree well with the experimental state origin energies at 4.31 and 4.88 eV. However, there remains some debate over the character of the S_2 state, and the applicability or otherwise of the

VB structures for S_2 and S_3, as shown in Fig.3.3, needs clarifying. In the following sections, some background about electronic structure methods will be described with a view to finding a method based on *ab initio* theory to describe the differential dynamic correlation in the excited singlet states of styrene.

3.2 Electronic structure theory methods for excited states

Separation of the nuclear and electronic motion using the Born-Oppenheimer approximation simplifies the problem of solving the molecular wavefunction. The electronic Schrödinger equation at fixed values of the nuclear geometry may be calculated to generate potential energy surfaces (see Chapter 1, Section 1.1). The many branches of the field of electronic structure theory are all devoted to the determination of the electronic wavefunction. Hartree-Fock self-consistent field (HF-SCF) theory is now a standard method by which ground state wavefunctions and associated observables may be calculated for small and medium sized molecules, using variation theory to optimise the wavefunction. For larger molecules and for the solid state, density functional theory has become a standard technique for calculating ground state wavefunction observables. These single determinantal ground state methods are not suitable for calculating the energies of excited electronic states of molecules, because the generally high degree of correlation associated with these states is neglected. Density functional theory (DFT) was originally formulated by Hohenberg and Kohn. The principle upon which DFT is based is that the electron density uniquely determines the properties of the ground state wavefunction. Thus, finding the wavefunction itself, a function of all the electronic coordinates, is not required to determine the energy of the ground state, the electron density, a function only of three spatial coordinates, is required. Calculation of a DFT wavefunction using Kohn-Sham self-consistent field theory using a standardised exchange-correlation functional is an often used method for calculating ground state energies.[30]

Electron correlation

The energy associated with exchange correlation is accounted for in the HF model in an averaged way: in a Slater determinant wavefunction, two electrons of the same spin are not allowed to occupy the same space, because of the Pauli principle. But this correction is only an averaged correction and does not account at all for the Coulomb correlation energy. In HF theory, using the orbital approximation, the electrostatic repulsion is modelled classically; each electron is modelled as being repelled by the field corresponding to the average positions of all the other electrons. In reality, the electrons' motions are correlated, *i.e.*, their movement is such that the actual interelectronic Coulombic repulsion at any moment is less than that calculated by modelling the repulsion of averaged electron positions (the exchange energy will vary concurrently, but the magnitude of this exchange energy is always significantly less than that of the Coulomb integral). Hence the wavefunction calculated using HF theory has a higher energy than the true wavefunction, even if the calculation is carried out at the basis-set limit. Generally, the correlation energy for a wavefunction is defined as the difference between the energy at the Hartree-Fock limit and the actual energy.

Correlation is usually sub-divided into two main types: dynamic correlation and non-dynamic (static) correlation. A description of dynamic correlation follows what has been described in the paragraph above. It is rooted in the dynamic behaviour of the electrons, hence the name. Non-dynamic correlation results from the degeneracy or near degeneracy of two or more molecular orbitals in the wavefunctions that have equal partial probability of occupation in the real wavefunction, but only one of which will be included in the single Slater determinant wavefunction of HF theory. Calculation of non-dynamic correlation energy is particularly important for estimating the wavefunctions and energies of excited states of organic molecules like benzene in which the frontier orbitals are degenerate.

Estimation of the dynamic correlation energy associated with a HF wavefunction is often computed using a perturbation theory based method that treats the correlation

energy as a small perturbation on the HF energy. Møller-Plesset perturbation theory is commonly used to the second order (MP2) correction to improve the energy of the HF wavefunction. The ground state DFT method is the starting point for families of excited state calculation methods. For small-to-medium sized molecules such as styrene, the time-dependent density functional theory (TDDFT) provides a computationally cheap method by which to calculate excited electronic states.

Configuration interaction

Ab initio methods for calculating excited states build on the HF wavefunction using configuration interaction (CI), where the wavefunction is a linear combination of Slater determinants corresponding to different configurations of occupied molecular orbitals. The CI family of methods can be used to account for both dynamic and non-dynamic correlation, depending on how it is applied. The wavefunction is expanded as a linear combination of Slater determinants

$$\Psi_{\mathrm{CI}} = c_0\Psi_{\mathrm{SD}} + c_1\Psi_{\mathrm{SD},1} + c_2\Psi_{\mathrm{SD},2} + \cdots, \tag{3.1}$$

where Ψ_{SD} is the ground state Slater determinant resulting from the SCF process and the $\Psi_{\mathrm{SD},n}$ are Slater determinants made from the SCF orbitals with occupations that correspond to excited electron configurations; these determinants are often called configuration state functions (CSFs). The determinants are weighted by the CI coefficients, c_n. Optimisation of the CI coefficients is carried out to obtain the final wavefunction, and higher roots of the CI matrix correspond to excited states.

Full CI corresponds to the use of all possible Slater determinants in the CI expansion of the wavefunction. For a molecule of more than a few atoms, with a substantially large basis set, full CI calculations are prohibitively expensive. Hence, approximations to the full CI wavefunction have been developed as electronic structure calculation methods to include some correlation energy into the energy expectation value of the wavefunction. CI singles (CIS) calculations are those in which the expansion is over the determinants that correspond to all the singly excited configurations; CISD or CID are those in which the expansion is over the determinants that correspond to all the doubly and singly or

doubly excited configurations. The doubly excited determinants are especially important for lowering the energy of the wavefunction as they are able to correctly describe the dynamic correlation of electron spin-pairs. CI singles (CIS) is sometimes used as a first approximation method for excited states, but results are often not satisfactory because the orbitals used in the CI expansion are optimised for the ground state.

Basis sets

As for Hartree-Fock calculations, good CI calculations are dependent on basis sets that are large and flexible enough for the target wavefunction. There are a few standardised basis sets that are in common use. Basis sets labelled STO-*N*G are designed to approximate Slater-type orbitals with linear combinations of *N* functions that have Gaussian radial dependence. The STO-*N*G basis sets are termed minimal basis sets because they include only a single composite function for each core and valence atomic orbital on each of the nuclei. Multiple basis functions for each AO are more common, and in particular, the split-valence Pople basis sets, where the valence AOs are represented with more basis functions than the core AOs. Pople split valence basis sets are often written *X*-*YZ*G, where *X* is the number of primitive Gaussians that are combined to make a single basis function for the core AOs, *YZ* implies that the valence AOs are represented by two basis functions, one of which is comprised of *Y* primitive Gaussians, and the other composed of *Z* primitive Gaussians. These split valence basis sets are usually augmented by the addition of functions with higher angular momentum to allow for polarisation effects: a basis set written *X*-*YZ*G* implies that the split valence has been augmented by six *d*-orbital-type functions on all nuclei except hydrogen and helium. Augmentation of the split valence basis set by diffuse functions is often used, and indicated by a + sign, as in the *X*-*YZ*+G, basis set, which included diffuse functions for all nuclei except those of hydrogen and helium.

Larger basis sets produce SCF wavefunctions that are variationally better than those produced by smaller basis sets. Obviously the use of very large basis sets is not possible

for the optimisation of the wavefunction of larger molecules. However, in some cases, it can be shown that convergence of the energy of the wavefunction can be reached with respect to the size of the basis set. This convergence with respect to basis set size is called the Hartree-Fock limit. Correlation consistent basis sets, developed by Dunning, and atomic natural orbital (ANO) basis sets have been developed using electron correlation methods.

In principle, the exact, non-relativistic energy for the wavefunction may be obtained with full CI and with a basis set that corresponds to the Hartree-Fock limit, but only for the very smallest of molecules is it possible to optimise the energy of this wavefunction. Fig. 3.4 illustrates the joint dependence of the wavefunction accuracy on the basis set and the amount of CSFs in the CI expansion.

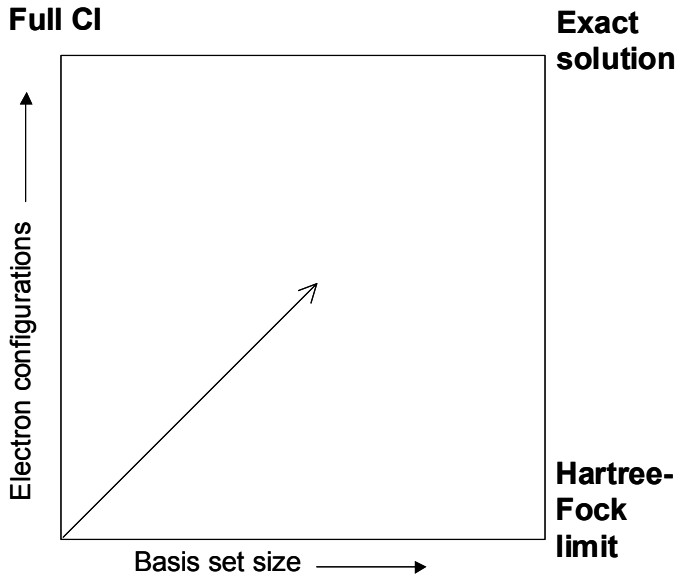

Figure 3.4 Schematic representation of successive approximations to the exact wavefunction, known as a Pople Square. Increasing the number of configurations and the basis set size are both necessary to lower the energy and aim towards the true energy given by the exact solution of the non-relativistic time-independent Schrödinger equation.

CASSCF and RASSCF

Multi-configurational self-consistent field (MCSCF) calculations offer an improvement on CIS and similar CI methods by allowing the simultaneous optimisation of the both the MO coefficients and at the CI coefficients, for a selection of CI determinants that form the wavefunction. Complete active space self-consistent field (CASSCF) is the most commonly-used form of MCSCF. It allows for the optimisation of the orbitals and CI coefficients for a subset of CSFs that are defined as all possible excitations within a set of MOs that are pre-selected; usually these MOs are the highest occupied and lowest unoccupied SCF MOs. A CASSCF calculation is described as having an active space of n orbitals, and a number active electrons, m, and the calculation is labelled CASSCF(m,n). The number of singlet configurations, N, in a CASSCF calculation is given by

$$N = \frac{n!(n+1)!}{\left(\frac{m}{2}\right)!\left(\frac{m}{2}+1\right)!\left(n-\frac{m}{2}\right)!\left(n-\frac{m}{2}+1\right)!}. \tag{3.2}$$

Although CASSCF calculations are usually not able to calculate much of the dynamic correlation energy of a wavefunction, they are often used to successfully describe the non-dynamic correlation that is a common feature of the excited states of many molecules. Simultaneous occupation of more than one of a degenerate pair of MOs is only possible using multi-configurational wavefunctions. Hence CASSCF calculations are often used in the modelling of the electronic spectroscopy of molecules, as the important differences in the non-dynamic correlation between the excited states and the ground states may be obtained. As the dynamic correlation is often approximately the same for the ground and excited states, reasonable estimations of the excitation energies may be obtained with CASSCF calculations of the ground and excited states of molecules. As for all CI calculations, the energy for the nth excited state is the energy of the nth root of the CI secular equations in CASSCF.

For even a small molecule such as styrene, attempts to include dynamic correlation in the wavefunction by expansion of the active space in a CASSCF calculation is not a

practical possibility due to the size of the CI expansion. Instead, more precise estimation of the excitation energy may be obtained using a CASPT2 calculation, which involves carrying out a CASSCF optimisation of the wavefunction, followed by an MP2 calculation to retrieve the dynamic correlation energy. Alternatively, a multi-reference configuration interaction (MRCI) calculation, which uses the multi-configurational wavefunction as a reference for expansion of the wavefunction into a linear combination of further singly, or singly and doubly, excited CSFs, may be carried out. Another method by which the energy of the wavefunction may be lowered is to use restricted active space self-consistent field (RASSCF) to include a limited number of higher excitations in the multi-configurational wavefunction as well as those in the CASSCF active space. The allowed CSFs in a general RASSCF calculation are shown schematically in Fig. 3.5.

The RASSCF excitation space comprises three active spaces: the CAS 1 space, from which a limited number of electron excitations are allowed; the CAS 2 space, which is equivalent to the active space in a CASSCF calculation in that all possible excitations are allowed; and the CAS 3 space in which a certain number of occupations are allowed. A RASSCF wavefunction is labelled by six parameters, m, n, a, b, c, d: the total number of active electrons in all three active spaces, m, and the number of orbitals in the three active spaces, n; the number of holes allowed in the RAS 1 space is a and the number of orbitals in the RAS 1 space is b**;** the number of occupations allowed in the RAS 3 space is c and the number of orbitals in the RAS 3 space is d.

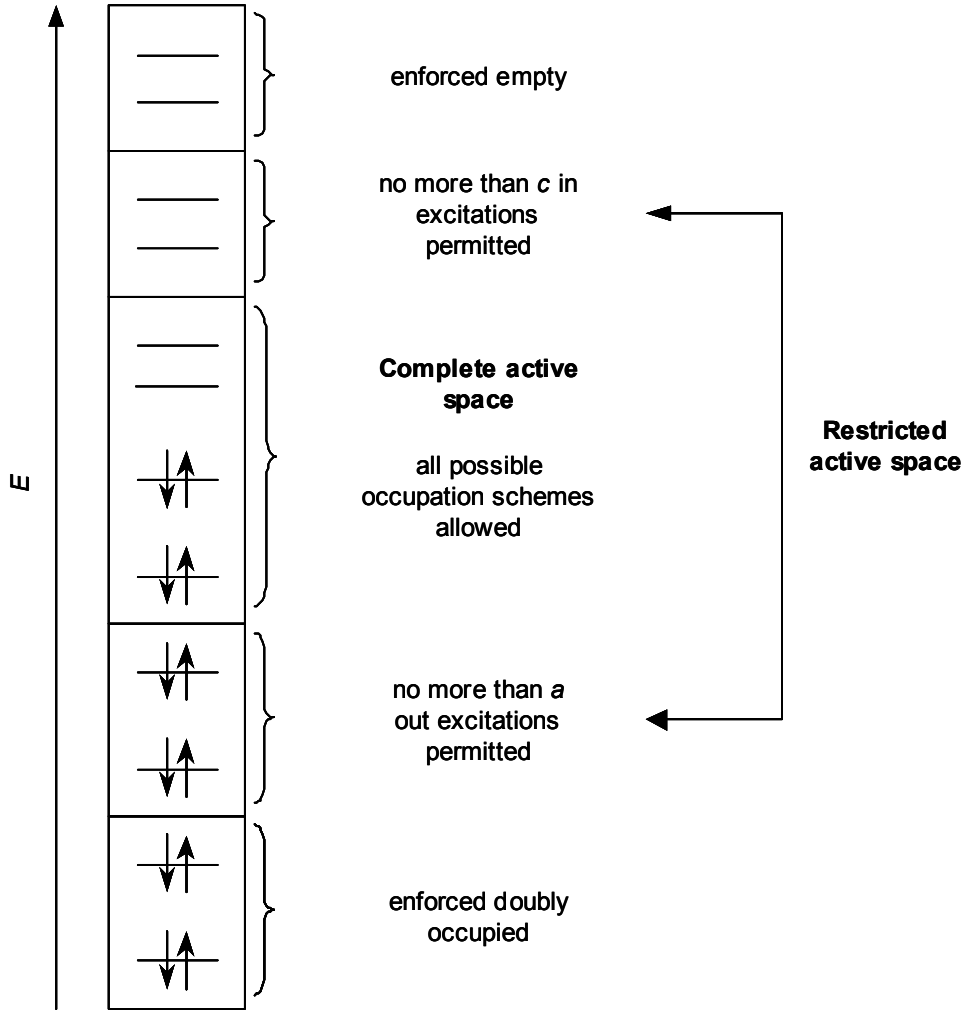

Figure 3.5 Schematic representation of the RASSCF method.

RASSCF and CASSCF calculations provide a flexible method for the calculation of excited states. They cannot be used as a black-box method, however. Selection of an active space that will yield realistic results requires some knowledge of the molecule and its excited states, either from preliminary calculations or from chemical knowledge acquired through experiment or qualitative theoretical models. To calculate several electronic states in a single optimisation of the wavefunction, one would need to include in the active space all the orbitals into which one would excite the electrons, for that set of states, within the single electron excitation formalism. State-averaging may be carried out if calculating the energy of two or more excited states at the same time, using

the same orbitals, to ensure othogonality of the CI roots. In a state-averaged calculation, the CI matrix is optimised such that the energy expectation values for all the roots of interest are minimised simultaneously. The resulting orbitals and CI coefficients are not optimal for any of the states, but are the optimal solution for a weighted average of all the states of interest.

Highly accurate *ab initio* excited state calculations require the inclusion of a large number of configurations in the wavefunction, and thus these calculations can be very expensive, or, as already stated, some knowledge of the states is required in advance in order to select an appropriate but not over-sized active space(s) in the wavefunction. Hence, for larger molecules, the use of non-wavefunction based methods such as TDDFT is sometimes desirable. TDDFT consists of finding the poles in an expression for the frequency dependent polarisability of the electronic wavefunction.[30] The black-box approach of TDDFT means that, so long as a suitable functional is selected, a computationally cheap calculation of all the excited states of a specific multiplicity for a molecule can be obtained with no prior knowledge of the states in question. Results are often quite close to experimental values, though they are not usually as precise as those from fully-correlated *ab initio* methods such as CASPT2 and MRCI. The HCTH functional, amongst others, has been found to reproduce excited state properties better than the B3LYP functional often used in ground state DFT calculations.[31,32]

3.3 Methods of characterising the excited electronic states of styrene

CASSCF and RASSCF *ab initio* electronic structure theory methods were chosen for this study of the excited states of styrene because geometry optimisations for minima transition states and conical intersections of relevance to photodynamics, may be carried out using the analytical gradients that are available with these methods. Analytical gradients are not yet available for more highly correlated methods such as CASPT2. Use of a full π active space in a CASSCF calculation allows for the retrieval of the non-

dynamic correlation energy for the excited state wavefunctions, as carried out by Bearpark *et al*.[2] A CASPT2 calculation based on such a π active space wavefunction would then calculate the majority of the dynamic correlation associated with these states, as reported by Molina *et al*.[12] In this chapter, an approach is described for the calculation of some of the dynamic correlation for the excited states within the CASSCF/RASSCF family of calculations. As has been discussed in Section 3.1, the VB character of the singlet excited states of styrene varies significantly between the first three states, and with it the dynamic correlation energy varies too. Calculation of the energy of a state that arises from mainly ionic VB structures (see Fig 3.3) will result in a value significantly less close to the true energy than that for a covalent excited state in the same manifold if the calculation is set up with an active space consisting of the π MOs; this is because the larger dynamic correlation energy of the ionic state wavefunction is not described by a valence 2*p* π active space. Thus, the aim of these calculations is to calculate the differential dynamic correlation of the S_1, S_2 and S_3 states to produce a balanced representation of this region of the excited singlet electronic structure, adding a specific basis function and including particular orbitals in the active space to try to achieve this without too much computational cost.

Increasing the active space of the CASSCF calculation to include specific virtual orbitals that are important for correlation in states that are dominated by ionic VB structures is one way in which differential correlation of the excited states may be treated. This has been demonstrated by Roos and co-workers, who studied benzene and other small molecules with an enlarged active space consisting of the π valence MOs as well as lower occupied, and some virtual orbitals.[33] In a similar method, Boggio-Pasqua *et al.*[34] used RASSCF to study butadiene, using an active space consisting of all excitations allowed within a CAS space of the 2*p* π and 3*p* π MOs, and also allowing single σ excitations. A new one-electron basis set designed to describe ionic excited states was also used in this study. These kinds of methods allow an approach towards excited state energies that may be obtained using a CASPT2 calculation.

The method adopted in the present work follows closely that of Boggio-Pasqua *et al*., using the same extra basis functions, combined with a standard 6-31G* basis set, and is denoted 6-31G* + 3*p*. The 3*p* basis functions on carbon build extra nodes into the wavefunction, which helps to keep the electrons apart, as is required for an ionic state wavefunction, where the charge builds up separately on carbon centres in the molecule. The larger size of styrene dictates that the exact active space selected for butadiene must be truncated. Two families of RASSCF excitation schemes were adopted in these calculations. First, a double active space is approximated by *x* excitations in the RAS 3 space, which consists of the 3*p* π orbitals, the RAS 1 space is not used, and the RAS2 space contains the valence 2*p* π MOs. This wavefunction is denoted CASSCF(8,16,RASSCF(0,0,$\boldsymbol{x}$,8)), and values of $\boldsymbol{x} = 1\text{-}4$ were used. The second excitation scheme adopted was CASSCF(24,32,RASSCF($\boldsymbol{y}$,8,1,16)), with $\boldsymbol{y} = 1$ and $\boldsymbol{y} = 2$. In this latter excitation scheme, the RAS 2 space remained the 2*p* π MOs, but the RAS 3 space includes 8 σ* orbitals, as well as the 3*p* π MOs, and the RAS 1 space consists of 8 σ MOs. The 3*p* π and σ orbitals were obtained by generating oscillator orbitals as originally defined by Boys[35] from localisations of the 2*p* π valence MOs, implemented in a development version of Gaussian.[36] In these calculations, the target orbitals were the 2*p* orbitals from the π active space, and a set of 3*p* oscillator orbitals were selected from of the series of oscillator orbitals that were generated for each target by minimisation of the sum of the squares of the vector distance expectation values between electron pairs in the localised target orbitals and the oscillator orbitals series. The selection of the 3*p* orbital from the set of oscillator orbitals was automatic: it was selected by determining the closest oscillator orbital to the target orbital. The target orbitals were obtained by localising the valence MOs from an initial calculation of the S_1 state.

In order to optimise the accuracy of the wavefunctions for the S_1, S_2 and S_3 states relative to each other, all the RASSCF and CASSCF wavefunctions were state-averaged with equal weights over these three states. S_0 was explicitly left out from the state-average weighting because, as already stated, the purpose of the current calculations has

not been to compute all the correlation energy difference between the excited state and the ground state, but to find a calculation method that will give a balanced description of S_1, S_2 and S_3 relative to each other. All the calculations were carried out using a development version of Gaussian.[36] For comparison, a TDDFT calculation of the first 12 excited singlet states of styrene was performed. For the CASSCF wavefunction, transition dipole moments, *R*, were calculated and for the TDDFT calculation, oscillator strengths, *f*, were calculated.

3.4 Results and discussion – characterising the excited states of styrene

The geometry of styrene in the ground state was optimised using a B3LYP/6-31G* DFT calculation. The optimised S_0 geometry is planar, with all the in-plane angles approximately 120º, and the CH distances 1.09 Å. The CC bond lengths on the benzene ring are all 1.40 Å, the ethylene CC bond is 1.34 Å, and the CC bond joining the benzene ring and the ethylene is 1.47 Å. This geometry was then used in all the further calculations of the vertical excitation energies. Table 3.1 shows the first three singlet vertical excitation energies of styrene calculated at several different levels of RASSCF excitations, labelled adiabatically.

	$x = 0$	$x = 1$	$x = 2$	$x = 3$	$x = 4$	$y = 1$	$y = 2$	$x = 0$ (without 3*p*)	$y = 1$ (without 3*p*)	TDDFT HCTH/ 6-311+G*	'New CAS(8,8)'[a]	CASPT2[b]	Experiment
S_1	4.61 ($R = 0.17$)	4.57	4.59	4.58	4.58	4.93	4.93	4.63	4.97	4.47 ($f = 0.03$)	5.45	4.34 ($f = 0.001$)	4.31[c]
S_2	6.35 ($R = 0.11$)	6.25	6.15	6.13	6.13	6.12	6.09	6.49	6.50	4.67 ($f = 0.30$)	6.21	4.97 ($f = 0.316$)	4.88[d], 5.11[e]
S_3	7.00 ($R = 1.77$)	6.32	6.34	6.34	6.34	6.65	6.64	7.41	6.73	5.31 ($f = 0.18$)	7.75	6.19/6.30 ($f = 0.691$/ 0.247)	6.37[f]

Table 3.1 Vertical excitation energies, in eV, for the first three singlet states of styrene calculated using state-averaged RASSCF wavefunctions. Transition dipole moments, *R*, and oscillator strengths, *f*, were calculated for some of the transitions. The first four columns in the table correspond to stepwise increase in the size of the CI expansion in the state-averaged RASSCF wavefunction with the general excitation scheme: CASSCF(8,16,RASSCF(0,0,$\boldsymbol{x}$,8)), with $\boldsymbol{x} = 0$ corresponding to a CASSCF(8,8) calculation. The sixth column, marked $\boldsymbol{y} = 1$, is for the excitation scheme CASSCF(24,32,RASSCF($\boldsymbol{y}$,8,1,16)). For all the calculations, the state-average weights were equal for the S_1, S_2 and S_3 states, and no weight was given to the ground state. The ground state energies from which the vertical excitation energies are calculated for all the RAS and CAS calculations are from the same $S_1/S_2/S_3$ state-averaged calculations in each case. A 6-31G* + 3*p* basis set was used for all the $\boldsymbol{x} = 1,2,3,4$ and $\boldsymbol{y} = 1,2$ calculations, except the seventh and eighth column, where the calculations are without the extra basis function. For comparison, the literature CASPT2 results and experimental results are also given in the last two columns (shaded).

[a]'New CAS(8,8)' results were CAS(8,8)/6-311+G*, optimised from the S_2 natural orbitals from the TDDFT HCTH/6-311+G* calculation, state-averaged as the other CASSCF calculations; [b]values taken from Ref. 12, where the S_3 values shown here are the S_5 and S_6 states, when labelled adiabatically from the CASPT2 calculation; [c]experimental origin of the S_1 state from Ref. 17; [d]experimental origin of the S_2 state from Ref. 23; [e]experimental absorption maximum for jet-cooled molecules from Ref. 23; [f]experimental band centre for the third absorption band from Ref. 37.

The twelve states from the TDDFT calculation were characterised by natural orbital calculations on each of the roots of interest. The results showed that the lowest three singlets were valence π states (the higher states included 6 Rydberg states and one state characterised by a σ to π* excitation). For the lowest level *ab initio* calculations, the CASSCF (8,8) wavefunction, the transition dipole moment, *R*, was also calculated, as shown in column 1 in Table 3.1. The S_3 state calculated at this level has a moment more

than 10 times the value of the other two. Both S_1 and S_3 have moments approximately in the direction of the long axis of the molecule, whereas the *R* direction for S_2 is approximately perpendicular to this. Molina *et al.*[12] in their CASSCF/CASPT2 study calculate a larger *f* for S_2 than S_1, but their S_1 and S_2 states have the transition dipoles directions both approximately in the direction of the long axis of the molecule, with higher states having approximately perpendicular dipole moment directions.

The character of the S_1 state is not in dispute in the literature. In agreement with all previous studies, it is clear from the low transition dipole moment calculated at the CASSCF level, that this is a covalent state. The natural orbitals localised for this state show that the excitation is almost entirely localised on the benzene ring.

Inspection of the trends in energy with $\boldsymbol{x}$ and $\boldsymbol{y}$ in Table 3.1, and the natural orbitals produced from the CASSCF, RASSCF and TDDFT wavefunction optimisations have allowed picture of the electronic character of the S_2 and S_3 states to be derived. First of all, it is clear that although the TDDFT calculations produce reasonably accurate energies for the S_1 and S_2 states, the S_3 state energy is not so good. The S_3 adiabatically labelled state was found by Bearpark *et al.* to be ionic (see Fig. 3.3), and the partially occupied natural orbitals for this state from the CASSCF(24,32,RASSCF(1,8,1,16)) calculation seem to indicate a partial charge transfer from ethylene to benzene, which seems to justify the ionic VB description. These natural orbitals are shown in Fig. 3.6.

Further evidence for the ionic character of the S_3 state is derived from the fact that its energy is much more substantially lowered by the single excitations into the RAS 3 space in the calculation labelled $\boldsymbol{x} = 1$, meaning that there is a significant amount of spin-polarisation or semi-internal correlation associated with this state, as would be expected for an ionic state.

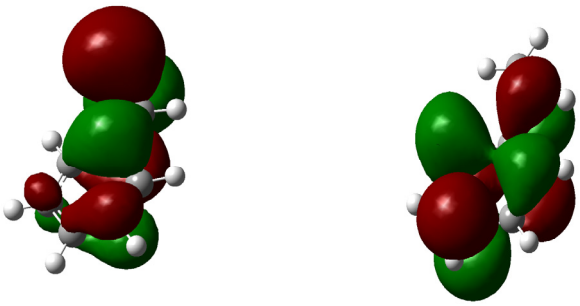

Figure 3.6 Partially occupied natural orbitals for the S_3 state calculated at the CASSCF(24,32,RASSCF(1,8,1,16))/6-31G* + 3*p* level with occupation numbers 1.19 (left) and 0.88 (right).

For S_2, the energy is not much lowered by the addition of the RAS 3 space to the CAS calculations. However, upon addition of the RAS 1 space with excitations from σ orbitals allowed, whilst the S_1 and S_3 states are raised by 0.35 eV and 0.31 eV respectively due to the significant reduction in S_0 energy at this level of theory, the S_2 state is *lowered* by 0.01 eV. Addition of a further excitation allowed from the σ orbitals of the RAS 1 space, *i.e.*, $\boldsymbol{y} = 2$ in the scheme CASSCF(24,32,RASSCF(***y***,8,1,16)), causes the same pattern in energy shifts, with a slight extra lowering of the S_2 compared to the S_1 and S_3 states. The structure suggested by Bearpark *et al.* for S_2 has the benzene in a Dewar structure (see Fig. 3.3). Fig. 3.7 shows two of the partially occupied natural orbitals for S_2 at the CASSCF(24,32,RASSCF(1,8,1,16)) level. These seem to support the Dewar benzene hypothesis, with an apparent excitation into a Dewar bonding orbital from a Dewar anti-bonding orbital. The calculation labelled 'New CAS' in Table 3.1 used the natural orbitals for S_2 from the TDDFT calculation as a starting point, and the energy of the resulting S_2 state is very close to the original CASSCF(8,8) shown in column 1 of Table 3.1. This demonstrates good agreement between TDDFT and the CASSCF results for S_2. The natural orbitals produced by the TDDFT calculation and the CASCF(8,8) and RASSCF(24,32, RASSCF(1,8,1,16)) calculations have very similar shapes for the S_1 and S_2 states, this also indicates good qualitative agreement between

these calculation methods on the character of these two states, despite the energy of the S_2 state being quite different for the TDDFT and the CAS/RAS method results. For S_3, as there is not really any resemblance between the TDDFT and RAS natural orbitals, and the energy of the S_3 state produced by the TDDFT calculation is quite inaccurate, the electronic structure of S_3 produced by this method must be viewed with caution.

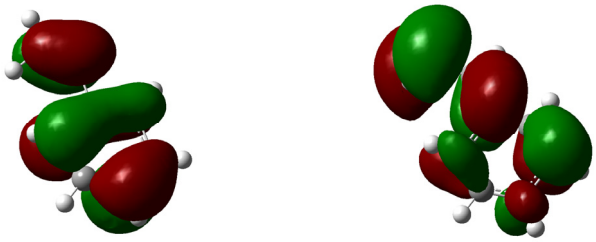

Figure 3.7 Partially occupied natural orbitals for the S_2 state calculated at the CASSCF(24,32,RASSCF(1,8,1,16))/6-31G* + 3*p* level with occupation numbers 1.04 (left) and 0.97 (right).

In the CASPT2 calculations used as a benchmark for the CAS and RAS calculations presented here, the S_2 and S_3 states reverse in energy after the MP2 retrieval of the dynamic correlation. The strong response of a state to dynamic correlation, as already discussed, is a clear indicator of ionic character. There is a possibility that at some point in the series of calculations shown in the first six columns of Table 3.1, enough excitations have been added to the wavefunction to allow the differential dynamic correlation of the states to be retrieved, and the character of the two adiabatically labelled states reversed. Although it is not in agreement with the discussions so far in this section, there is a little evidence to suggest this. Comparing the calculations in Table 3.1 with and without the extra 3*p* basis function, at the CAS(8,8) level, the S_3 state is significantly lowered by the addition of the extra 3*p* function, whereas at the CASSCF(24,32,RASSCF(1,8,1,16)) level, the extra 3*p* basis function has the effect of lowering the S_2 state significantly. The response of the wavefunction to the extra basis function is an approximate diagnosis of ionic character of a state, because it is used to

build dynamic correlation into the wavefunction. A more conclusive test of this hypothesis would, of course, be to carry out a transition dipole moment calculation at every level of theory, but at present the transition dipole moment code is not implemented into the RASSCF code in the Gaussian development version.

3.5 Results and discussion – ionisation correlations for the singlet states of styrene

The TDDFT/HCTH results already presented in Table 3.1 were used along with a similar calculation of the excited state of the cation using the same method. The resulting ground state reference orbitals for these two calculations, for the neutral and for the cation, are very similar, and therefore comparisons between their electronic structure can be made simply by comparing the weights of various configurations of their ground state orbitals. The ground state orbitals for the neutral and cation state are shown in Fig. 3.8. The energies of the cation states relative to the neutral ground state have been calculated using the TDDFT results and the experimental ionisation energy. A summary of the energies and configuration weights of the cation and neutral states is given in Table 3.2. For the calculation of the cation excited states, the total spin of the wavefunction was not constrained, but the expectation values of S^2 for the lowest five excited cation state wavefunctions were between 0.78 and 0.75, which corresponds to them being doublet states.

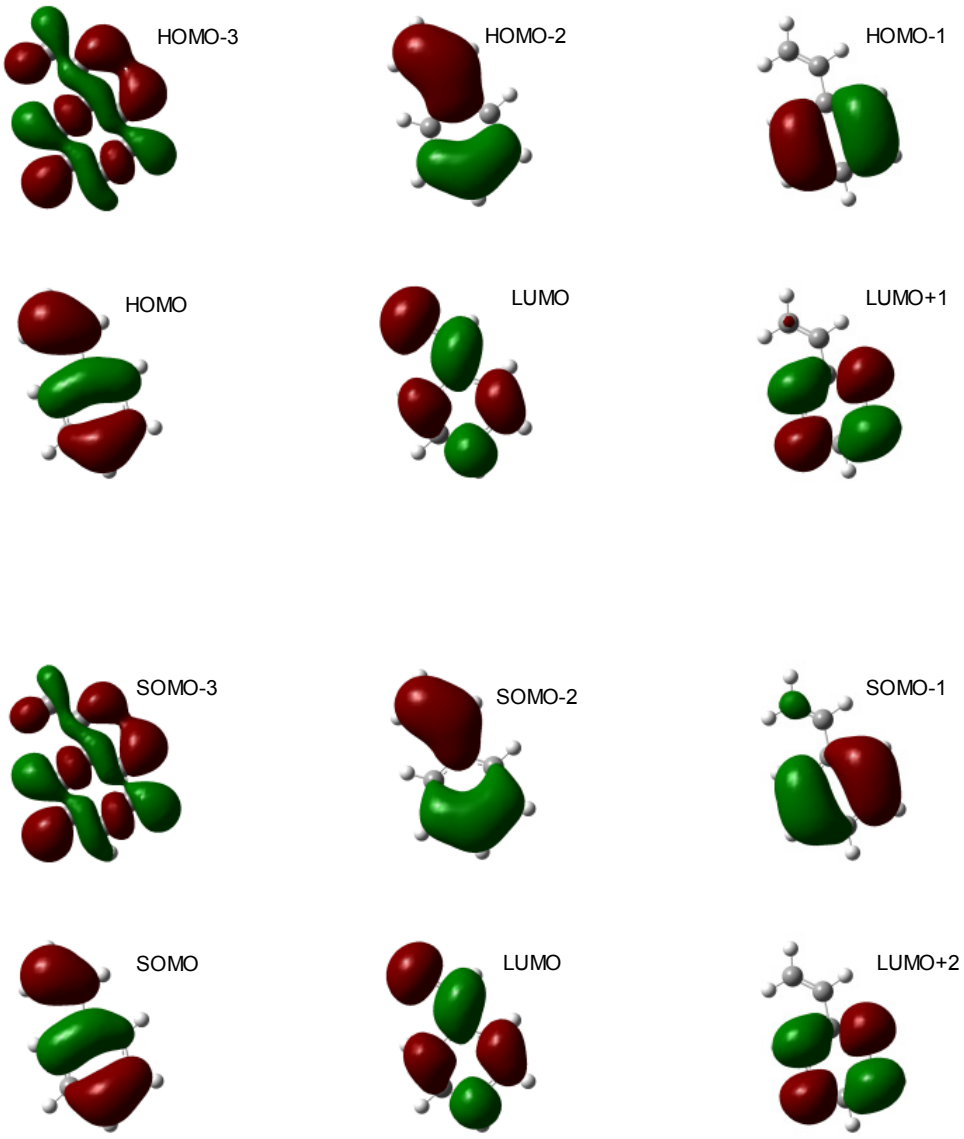

Figure 3.8 Comparison of the important reference orbitals in the wavefunction expansions from the TDDFT HCTH/6-311+G* calculation of the neutral (upper half of figure) and cation (lower half) excited states of styrene. For the cation orbitals, the reference wavefunction is formally unrestricted, and the orbitals shown here are all the α spinorbitals, but the difference between the α and β spinorbitals in this calculation is very small.

	Energy / eV	Configurations	Configuration coefficient	Configuration weight
S_1	4.31[a]	HOMO-1→LUMO	0.48	0.23
		HOMO→LUMO	0.23	0.05
		HOMO→LUMO+1	-0.47	0.22
S_2	4.88[b], 5.11[c]	HOMO-1→LUMO	-0.26	0.07
		HOMO→LUMO	0.64	0.41
S_3	6.19[d]	HOMO-2→LUMO+1	0.20	0.04
		HOMO-1→LUMO	0.41	0.17
		HOMO-1→LUMO+5	-0.15	0.02
		HOMO→LUMO	0.13	0.02
		HOMO→LUMO+1	0.49	0.24
D_0	8.46	Ground configuration of the cation	1.00	1.00
D_1	9.12 $\langle S^2 \rangle = 0.78$	SOMO-1→SOMO	1.00	1.00
D_2	10.76 $\langle S^2 \rangle = 0.75$	SOMO-1→LUMO	0.18	0.03
		SOMO→LUMO	0.27	0.07
		SOMO-2→SOMO	0.94	0.88

Table 3.2 Relative energies and configurations of the neutral and cation states of styrene. The D_0 cation energy is the first ionisation energy of styrene and the D_1 and D_2 cation energies are the cation TDDFT HCTH/6-311+G* vertical excited state energies, calculated at the geometry of the ground state of the neutral, added to the D_0 energy. Literature vertical excitation energies for the S_1, S_2 and S_3 states relative to S_0 are given for comparison. The orbitals referred to in the configurations are shown in Fig. 3.8. Configuration weights are the square of the configuration coefficients. Total weights for each of the neutral and cation states are approximately 0.5, and 1, respectively.[e]

[a]experimental origin of the S_1 state from Ref. 17; [b]experimental origin of the S_2 state from Ref. 23; [c]experimental absorption maximum for jet-cooled molecules from Ref. 23; [d]CASPT2 energy from Ref. 12; [e]The following is from an email from help@gaussian.com written in response to a query regarding comparison of the expansion coefficients from a CIS and TDDFT calculations: "The short answer is that is normal that for singlet references the normalization is to 0.5 and for open shell references it is to 1.0. The basic issue is that for a closed shell singlets there are excitations from both alpha and beta orbitals which will be identical since the alpha and beta orbitals are identical. So 0.5 reflects just half of the configurations and the total will be 1.0. For UHF open shell references the alpha and beta orbitals are different so all of the potential excitations need to be included and the vector listed will normalize closer to 1.0.

"For TD-DFT the situation is similar but not identical. The basic distinction between singlets and open shell references holds but the normalization for TD-DFT is <X+Y|X-Y>=1 where X is the vector of excitation coefficients and Y is the corresponding de-excitation. And the weights given for the TD states in G03 correspond to |X+Y> rather than just X or Y. So minor deviations from 0.5 in the normalization are because you should not be squaring elements of |X+Y> but rather the product with |X-Y>. So in general the values are qualitative rather than quantitative but they will be close in most cases."

The one-electron ionisation correlations can be determined by inspection of Table 3.2, if the D_2 state is assumed to be entirely of SOMO-2→SOMO character. The S_1 state of the neutral correlates with both the D_0 and D_1 state of the cation, and likewise, the S_2 state correlates with both the D_0 and D_1 states, but with different relative weights. The S_3 state correlates with the D_0 and D_1 states and very slightly with the D_2 state. These correlations and weights are summarised in Table 3.3. This table summarises all the information necessary to assign bands in the time-resolved photoelectron spectra of styrene that are presented in Chapter 4.

	Energy / eV	**Correlated cation state**		**Relative weight of correlated cation state (Approximate transition probability)**
S_1	4.31[a]	D_0	8.46 eV	0.54
		D_1	9.12 eV	0.46
S_2	4.88[b], 5.11[c]	D_0	8.46 eV	0.82
		D_1	9.12 eV	0.14
S_3	6.19[d]	D_0	8.46 eV	0.52
		D_1	9.12 eV	0.38
		D_2	10.76 eV	0.08

Table 3.3 Relative energies of the neutral and cation states of styrene, and ionisation correlations. The cation energies are the cation TDDFT HCTH/6-311+G* vertically excited state energies, added to the first ionisation energy of styrene. Literature values for the S_1, S_2 and S_3 states relative to S_0 are also given. The orbitals referred to in the configurations are shown in Fig. 3.8.
[a]experimental origin of the S_1 state from Ref. 17; [b]experimental origin of the S_2 state from Ref. 23; [c]experimental absorption maximum for jet-cooled molecules from Ref. 23; [d]CASPT2 vertical excitation energy from Ref. 12.

There is no way of independently assessing the quality of the excited cation state energies, D_1 and D_2 given by the TDDFT HCTH/6-311+G* method, as there is no experimental data with which to compare them. However, values of the excited cation state energies were calculated by Stolow and co-workers for their time-resolved photoelectron spectra assignments,[3] using the B3LYP functional: they obtained 10.65

eV, and 10.94 eV excitation energies from the ground state, when scaled by the first ionisation potential, for D_1 and D_2 respectively. The values presented in this work are likely to be more reliable than these literature values because, as already mentioned in Section 3.2, the HCTH functional has been shown to be fairly accurate for excited states, whereas B3LYP is not generally used in TDDFT calculations. The ionisation correlations for S_3 should perhaps be viewed with some caution, as the TDDFT result for this state is probably not very accurate (see Section 3.4). A perhaps more rigorous version of the TDDFT method used here would be to calculate the energies of each of the excited states and each of the cation states using a highly correlated *ab initio* calculation, and inspect the various natural orbitals for the cation and neutral states to see which correlate, and extract the energies, as differences, as per the TDDFT results presented here. To calculate accurate values, of the cation energies, a balanced treatment of the different ion states would be required, just as a balanced treatment of the excited states of the neutral was the aim of the calculations presented in Section 3.4; by contrast the TDDFT calculations presented here are a 'black-box' treatment of the electronic excited state wavefunctions.

3.6 Conclusions

The character of the S_2 and S_3 states of styrene has not yet been established, even in this study. As discussed in Section 3.4, there is conflicting evidence from the above results as to whether or not the ionic state, unambiguously identified at the CAS(8,8) level as S_3, remains the S_3 state when the higher excitations are added in the calculations presented here. If the energy ordering of the two states, S_2 and S_3 has been reversed by adding excitations to the 3*p* orbitals, excitations to the σ orbitals and excitations from the σ^* orbitals in the CASSCF(24,32,RASSCF(1,8,1,16)) calculation, then we can conclude that the method has been successful in retrieving the differential dynamic correlation of the states to give a state ordering that agrees with the benchmark CASPT2 calculations. In this case, the next step would be to move onto the carrying out of

geometry optimisations and conical intersection searches on the excited state in the hope of providing a more detailed model for the experimental dynamics reported in Chapter 4. However, at present we cannot definitely confirm this, and so before carrying out any excited state geometry studies, a better understanding of the character of the states in the Franck-Condon region must be obtained.

The calculations of the styrene excited state-cation correlations and energies in Section 3.5 have provided an approximate but very simple method by which to assign photoelectron bands in the time-resolved photoelectron spectra presented in Chapter 4. A much more complete model for the time-resolved photoelectron spectra might involve a combination of the work in Sections 3.4 and 3.5: using the balanced *ab initio* method to describe the excited states, locate a minimum energy path after the excitation to S_2 and then calculate the vertical ionisation correlations, both electrionic and Franck-Condon, for the molecule at different geometries on the pathway. This would give a more *time-dependent* model for the *time-resolved* spectra. The current ionisation correlation results, as summarised in Table 3.3, can be used in an analysis method that allows an approximate interpretation of experimental time-resolved photoelectron spectra results, in which conservation of vibrational energy and unvarying ionisation correlations for the entire decay pathway are assumed; this is the analysis method adopted in the next chapter.

References

1 A. D. G. Nunn, R. S. Minns, M. J. Bearpark *et al.*, Physical Chemistry Chemical Physics, in preparation.

2 M. J. Bearpark, M. Olivucci, S. Wilsey *et al.*, Journal of the American Chemical Society 117 (26), 6944 (1995).

3 S. H. Lee, K. C. Tang, I. C. Chen *et al.*, Journal of Physical Chemistry A 106 (39), 8979 (2002).

4 J. W. Ribblett, D. R. Borst, and D. W. Pratt, Journal of Chemical Physics 111 (18), 8454 (1999).

5 Y. Amatatsu, Journal of Computational Chemistry 23 (10), 950 (2002).

6 J. R. Platt, Journal of Chemical Physics 17 (5), 484 (1949).

7 P. G. Wilkinson and R. S. Mulliken, Journal of Chemical Physics 23 (10), 1895 (1955).

8 J. Michl and V. Bonacic-Koutecky, *Electronic aspects of organic photochemistry*. (Wiley, 1990).

9 J. G. Philis, A. Ioannidou, and A. A. Christodoulides, Journal of Molecular Spectroscopy 174 (1), 51 (1995).

10 P. Swiderek, M. J. Fraser, M. Michaud *et al.*, Journal of Chemical Physics 100 (1), 70 (1994).

11 L. D. Ziegler and C. Carotsis, Chemical Physics Letters 123 (3), 175 (1986).

12 V. Molina, B. R. Smith, and M. Merchan, Chemical Physics Letters 309 (5-6), 486 (1999).

13 J. Wan and H. Nakatsuji, Chemical Physics 302 (1-3), 125 (2004).

14 J. M. Hollas, E. Khalilipour, and S. N. Thakur, Journal of Molecular Spectroscopy 73 (2), 240 (1978).

15 P. H. Hepburn and J. M. Hollas, Molecular Physics 26 (2), 377 (1973).

16 J. M. Hollas, H. Musa, T. Ridley *et al.*, Journal of Molecular Spectroscopy 94 (2), 437 (1982).

17 J. M. Hollas and T. Ridley, Chemical Physics Letters 75 (1), 94 (1980).

18 J. M. Hollas and T. Ridley, Journal of Molecular Spectroscopy 89 (1), 232 (1981).

19 J. A. Syage, F. Aladel, and A. H. Zewail, Chemical Physics Letters 103 (1), 15 (1983).

20 S. Zilberg and Y. Haas, Journal of Chemical Physics 103 (1), 20 (1995).

21 M. de Groot and W. J. Buma, Chemical Physics Letters 435 (4-6), 224 (2007).

22 J. M. Hollas, *High Resolution Spectroscopy*, 2nd Edition ed. (Wiley, 1998).

23 D. G. Leopold, R. J. Hemley, V. Vaida *et al.*, Journal of Chemical Physics 75 (10), 4758 (1981).

24 R. J. Hemley, U. Dinur, V. Vaida *et al.*, Journal of the American Chemical Society 107 (4), 836 (1985).

25 R. J. Hemley, D. G. Leopold, V. Vaida *et al.*, Journal of Chemical Physics 82 (12), 5379 (1985).

26 Y. Amatatsu, Chemical Physics Letters 344 (1-2), 200 (2001).

27 J. G. Philis, E. Drougas, and A. M. Kosmas, Chemical Physics 306 (1-3), 253 (2004).

28 Y. Amatatsu, Journal of Computational Chemistry 23 (9), 928 (2002).

29 Y. Amatatsu, Journal of Molecular Structure-Theochem 624, 159 (2003).

30 C. J. Cramer, *Essentials of Computational Chemistry*, 2nd Edition ed. (Wiley, 2004).

31 F. A. Hamprecht, A. J. Cohen, D. J. Tozer *et al.*, Journal of Chemical Physics 109 (15), 6264 (1998).

32 A. D. Boese and N. C. Handy, Journal of Chemical Physics 114 (13), 5497 (2001).

33 B. O. Roos, K. Andersson, and M. P. Fulscher, Chemical Physics Letters 192 (1), 5 (1992).

34 M. Boggio-Pasqua, M. J. Bearpark, M. Klene *et al.*, Journal of Chemical Physics 120 (17), 7849 (2004).

35 S. F. Boys, Reviews of Modern Physics 32 (2), 296 (1960); J. M. Foster and S. F. Boys, Reviews of Modern Physics 32 (2), 300 (1960).

36 M. J. Frisch, G. W. Trucks, H. B. Schlegel G. E. Scuseria, M. A. Robb, J. R. Cheeseman, J. A. Montgomery, Jr., T. Vreven, G. Scalmani, B. Mennucci, V. Barone, G. A. Petersson, M. Caricato, H. Nakatsuji, M. Hada, M. Ehara, K. Toyota, R. Fukuda, J. Hasegawa, M. Ishida, T. Nakajima, Y. Honda, O. Kitao, H. Nakai, X. Li, H. P. Hratchian, J. E. Peralta, A. F. Izmaylov, K. N. Kudin, J. J. Heyd, E. Brothers, V. N. Staroverov, G. Zheng, R. Kobayashi, J. Normand, J. L. Sonnenberg, F. Ogliaro, M. Bearpark, P. V. Parandekar, G. A. Ferguson, N. J. Mayhall, S. S. Iyengar, J. Tomasi, M. Cossi, N. Rega, J. C. Burant, J. M. Millam, M. Klene, J. E. Knox, J. B. Cross, V. Bakken, C. Adamo, J. Jaramillo, R. Gomperts, R. E. Stratmann, O. Yazyev, A. J. Austin, R. Cammi, C. Pomelli, J. W.

Ochterski, P. Y. Ayala, K. Morokuma, G. A. Voth, P. Salvador, J. J. Dannenberg, V. G. Zakrzewski, S. Dapprich, A. D. Daniels, M. C. Strain, O. Farkas, D. K. Malick, A. D. Rabuck, K. Raghavachari, J. B. Foresman, J. V. Ortiz, Q. Cui, A. G. Baboul, S. Clifford, J. Cioslowski, B. B. Stefanov, G. Liu, A. Liashenko, P. Piskorz, I. Komaromi, R. L. Martin, D. J. Fox, T. Keith, M. A. Al-Laham, C. Y. Peng, A. Nanayakkara, M. Challacombe, W. Chen, M. W. Wong, and J. A. Pople, Gaussian Development Version, Revision G.01 (Gaussian Inc., Wallingford CT, 2007).

37 K. Kimura and S. Nagakura, Theoretica Chimica Acta 3 (2), 164 (1965).

Chapter 4

Time-resolved photoelectron spectroscopy of styrene

The photophysics and photochemistry of small molecules such as styrene are test cases from which the behaviour of larger, more chemically and biologically relevant molecules can be understood. A study of the theoretical electronic spectroscopy of styrene was presented in Chapter 3, laying the groundwork for future theoretical investigations into the *dynamical* behaviour of styrene after photon absorption. In this chapter, an experimental investigation of the excited state dynamics of styrene is presented using two-colour time-resolved photoelectron spectroscopy. The details of the experiment, and the data analysis, are described in Sections 4.2 and 4.3 respectively. Assignments of the excited-state to cation transitions recorded in the photoelectron spectra have been made possible using the Koopmans' correlations and transition energies calculated and presented in Section 3.5. Results and discussion of the assignments is given in Section 4.4, and a conclusion in Section 4.5. There are several theoretical studies, and a few experimental studies, in the literature on the excited state dynamics of styrene, and a discussion of these begins this chapter in Section 4.1, following on from the spectroscopy of styrene that was dealt with in Section 3.1, in Chapter 3. This chapter, and parts of Chapter 3 are currently being edited for publication.[1]

4.1 Excited state dynamics of styrene reported in the literature

The dynamical behaviour of the excited states of styrene can be understood to first order from a theoretical knowledge of critical points and crossings on the ground and excited state potential energy surfaces, as discussed in Chapter 1 (Section 1.1). Recent theoretical studies of the photochemistry of styrene have focussed on the singlet state photodynamics.[2-4] However, although phosphorescence has never been detected from photoexcited styrene, many studies have suggested that photochemical *cis-trans* isomerisation mechanisms for styrene proceed *via* triplet states. For a review of the photophysics and photochemistry of styrene, see Ref. 5 and references therein. Intersystem crossing rates have been calculated from liquid-phase transient absorption measurements.[6]

In terms of experimental investigations, some of the earliest dynamics studies were carried out by Salisbury and co-workers, who reported nanosecond time-resolved fluorescence experiments. Their results led them to the supposition that there is a 'twisted state' in S_2 that exhibits its own fluorescence wavelength, bluer than the main component from S_2 excitation, and with a longer lifetime.[7,8] Fluorescence lifetimes of styrene in the gas-phase after excitation at around 257 nm are 35 ns longer for the bluer emission component, which does not appear at all when excited at the longer wavelength of 287 nm.[8] However, their interpretation of the fluorescence spectra could now be questioned by the definitive measurement of the S_2 origin as 4.88 eV above the S_0 origin,[9] which is an energy some 0.06 eV larger than that of the excitation wavelength used in their experiments (257.25 nm) to excite what they report is S_2. Zewail and co-workers studied the fluorescence of jet-cooled isolated styrene and reported that the fluorescence emission line widths broaden with excitation energy because of IVR, and an estimate of the timescale of IVR was given as 1 ns, with 1200 cm^{-1} of excess energy in S_1.[10]

Planar minima are generally predicted for the first three singlet states from both experimental and theoretical results,[11-13] but this does not rule out the possibility of another perpendicular minimum for the first singlet excited state, as predicted in an early study by Hui and Rice.[14] Changes in energy of the S_0, S_1, S_2, and S_3 excited states as a function of some molecular coordinates have been calculated by Merchan and co-workers[4]; these calculations impact on the predicted decay of the states. The potential energy surfaces of the low-lying triplet and singlet states (S_0, S_1, S_2, T_1 and T_2) have been studied by Bearpark *et al.* with a detailed description of the photochemical isomerisation pathways. More recently, S_0/S_1 and S_2/S_1 conical intersections have been studied by Amatatsu.[2,3] These are thought to be important in the isomerisation reaction, and form a decay path from the S_2 state.

Experimentally, Stolow and co-workers carried out the most recent dynamics measurement, using femtosecond time-resolved photoelectron spectroscopy; these authors reported the direct observation of the S_1-S_2 internal conversion after excitation to the S_2 state using a 254.3 nm pump and probing with a 208 nm or a 218.5 nm pulse. The temporal width of their pulse was c.a. 100-150 fs, and, according to their observations, an IC was recorded that was approximately complete within 300 fs.

4.2 Two-colour femtosecond time-resolved photoelectron imaging experiment

In the present work, two-colour time-resolved photoelectron spectroscopy of vapour-phase styrene was undertaken. The experimental setup consists of the interaction of three main components: an Even-Lavie valve molecular beam, pump and probe lasers, and a photoelectron imaging spectrometer.

Molecular beam

Initial experiments were carried out to try to create a molecular beam with *cis*-stilbene and argon. The mechanism by which the Even-Lavie valve operates relies on fine

micro-precision engineering to open the valve using a solenoid, switched on for 10-20 μs, which forces a plunger away from a sealing gasket on a nozzle. After the first experiments with stilbene and argon, the valve started to malfunction. Upon inspection of the valve, it was apparent that the opening had become blocked with a solid material that resembled *trans*-stilbene. Whilst the valve was operating at its maximum frequency of 1 kHz, the heat caused by the high voltage pulse was not able to dissipate effectively before the next voltage pulse. *Trans*-stilbene is solid even at high temperatures, and therefore it can be concluded that the high temperature resulting from the over heating, as well as the normal high pressure within the valve, were triggering thermal isomerisation of the *cis*-stilbene to *trans*-stilbene within the valve mechanism and thus blocking its opening mechanism. An adaptation of the valve was made in an attempt to improve its operation at 1 kHz, this was carried out in the workshops of the Sackler School of Chemistry at the University of Tel Aviv, where the valve was originally built. Parts of the stainless steel valve supports that connect the valve to the outside flange (the heat sink) were removed and replaced with aluminium, which has a higher conductivity. This adaptation reduced the working temperature of the nozzle by a few degrees when operated at 1 kHz. Experiments with *cis*-stilbene were eventually abandoned, however, after it was found that there was no way to produce a photoelectron signal with a measurable intensity. This was presumably because *cis*-stilbene would not vaporise sufficiently at cool temperatures, and at higher temperatures, as already noted, isomerisation occurred within the valve itself.

A styrene molecular beam was generated by passing helium at very low (<100 mbar) pressure though liquid styrene (Alfa Aesar, 99.5%, stabilised with 4-tert-butyl-catechol) and then expanding into a chamber *via* the Even-Lavie pulsed valve (E.L.-7-4-2008-HRR).[15] An alternative seeding method was first attempted: the valve has a purpose-built cartridge in which solid or liquid samples may be placed. The cartridge is situated in the gas line, so that the seeding-gas can carry the vaporised sample to the nozzle. The small size of the internal cartridge meant that it needed re-filling regularly. Refilling the internal cartridge necessitated removing the entire valve assembly from the

vacuum and it was found that situating a styrene reservoir in the gas line outside the chamber was a more practical method of seeding the styrene than using the internal cartridge. A diagram of the valve is shown in Fig. 4.1.

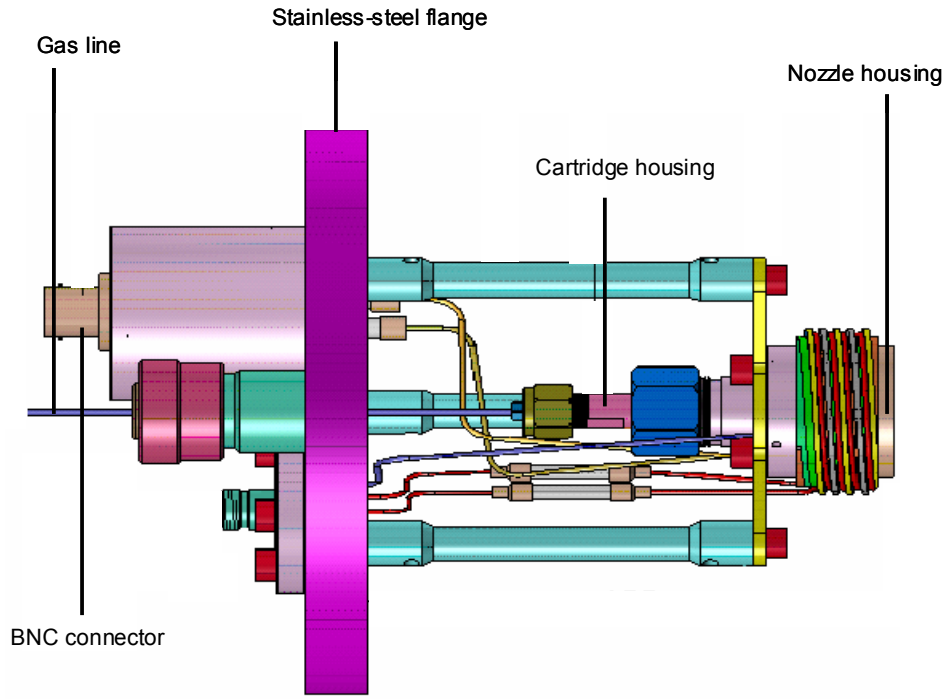

Figure 4.1 Even-Lavie pulsed valve (E.L.-7-4-2008-HRR). The gas line enters the vacuum-sealed flange *via* an opening in the flange, which is itself sealed by a small inset Wilson seal. The valve can easily be dismantled for cleaning by removing the entire gas line and attached cartridge and then removing the mechanism. A BNC cable connects the valve to the controller, from which the opening time and operation frequency is controlled. The valve may be heated, for which a thermocouple is attached to the internal heating *via* another connector. The heating capacity was not used to produce the results presented in this chapter. Figure adapted with permission from Ref. 15.

The valve is pulsed and is synchronised to produce temporal overlap of the molecular beam with the pulsed lasers, reducing the amount of wasted gas. The valve was operated at 500 Hz, half the normal operating frequency of the laser system, to minimise heating in the valve that occurs as the valve operates at its maximum frequency of 1

kHz. The laser operation frequency was also reduced to 500 Hz, so that the timing of the nozzle and laser could be synchronised from the same source. The valve was opened for between 10 and 13 μs, timed to overlap with the laser pulse, and remained closed for the remaining 1990 or 1987 μs of its cycle. The laser-nozzle timing was controlled by a delay generator (DG535). The timing controls for the entire time-resolved photoelectron spectroscopy experiment are shown in Fig. 4.2.

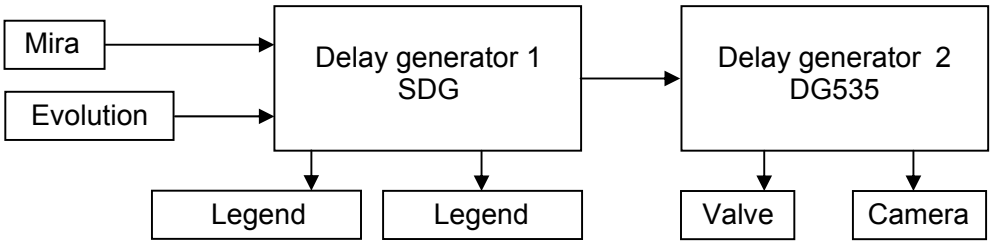

Figure 4.2 Timing trigger controls. The Mira mode-locked femtosecond laser operates at 86 Hz, and the SDG is used to time its entrance and exit from the amplifier (Legend) with Pockels cells 1 and 2, PC1 and PC2, to allow sufficient build-up of the pump laser (Evolution) oscillations in the cavity of the amplifier (more detail on the lasers is found in Chapter 2, Section 2.2). The trigger from the SDG box is used to connect the pulsed valve and photoelectron imaging camera controllers to the amplified laser pulse *via* the DG535.

Characterisation of the molecular beam

Expansion of the gas into the vacuum chamber provided some cooling of the molecules. The likelihood of the formation of clusters in the beam was minimised by using a very low-pressure carrier gas and by choosing helium as a carrier gas over larger molecule carrier gases such as argon, which are known to be more effective at stabilising clusters.[16] In order to make sure that there were no styrene clusters, or indeed styrene polymers[†] in the molecular beam, the mass spectrum of the molecular beam was recorded by ionisation with 240 nm femtosecond pulses from the OPA (see Section 2.2,

[†] Styrene can polymerise as a liquid, or in the gas-phase under certain conditions.[17]

and below for more on the lasers). In order to do this, the polarity of the voltages on the time-resolved photoelectron imaging spectrometer were reversed (see below for more about the photoelectron imaging spectrometer). A de-coupling capacitor connected to the back of the phosphor screen was used to extract the energy-integrated photoion voltage signal from high voltage and this was then sent to an oscilloscope. The resulting trace is displayed in Fig. 4.3.

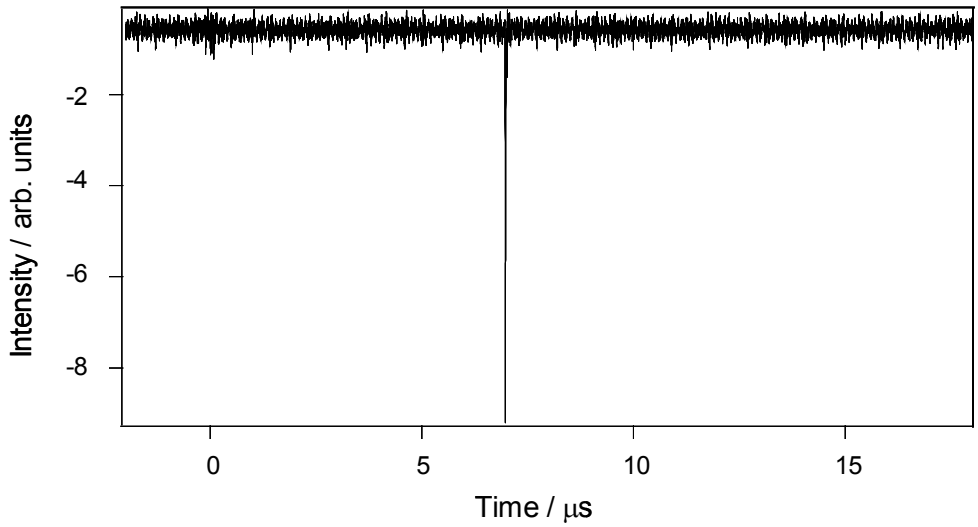

Figure 4.3 Time-of-flight spectrum of styrene. The peak at 7 μs is the styrene monomer.

The spectrum was calibrated using the time-of-flight of benzene, and the resulting times-of-flight of styrene and its clusters were calculated and are listed in Table 4.1. As clearly shown by Fig. 4.3, there is no evidence for the presence of styrene dimers, trimers or larger clusters.

	m/z	***Time-of-flight* / μs**
Styrene	104	7.0
$(styrene)_2$	208	10.1
$(styrene)_3$	312	12.5
$(styrene)_4$	416	14.5
$(styrene)_5$	520	16.2

Table 4.1 Mass-to-charge ratios and times-of-flight of styrene and some styrene clusters.

Vacuum chamber

The vacuum chamber is divided into two by a 4 mm entrance diameter conical skimmer (home built) that separates the valve from the region in which the laser and molecular beams interact. The skimmer selects some of the colder styrene molecules from the beam pulse produced by the valve. The background pressure in the vacuum chamber was maintained at 10^{-8} mbar, and when the Even-Lavie pulsed valve is in operation, the pressure in the chamber is raised by only 1-5 × 10^{-8} mbar. The source side of the chamber is pumped by a turbo magnetic levitation pump (Leybold Mag W2200) with a pumping rate of 2200 L s^{-1} and backed by a rotary pump (Oerlikon Leybold, 25 m^3 h^{-1}), and the detector side is pumped by a turbo pump (Leybold) with a pumping rate of 1000 L s^{-1} and backed by a rotary pump (Oerlikon Leybold, 40 m^3 h^{-1}). A schematic diagram of the vacuum chamber is shown in Fig. 4.4.

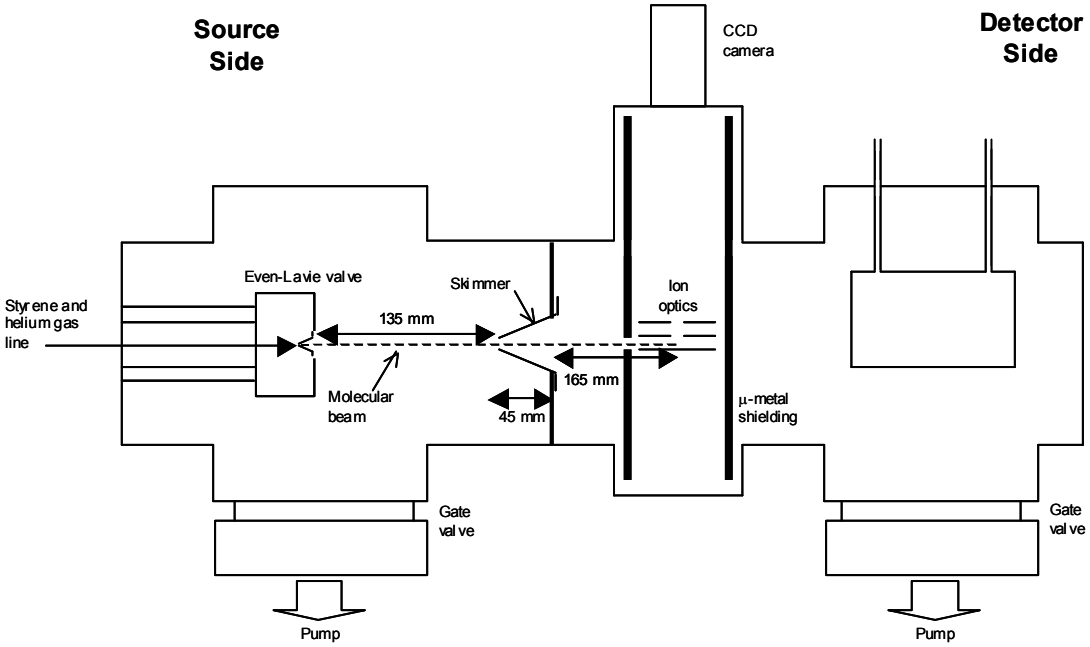

Figure 4.4 Schematic diagram of the vacuum chamber. The molecular beam is generated in the Even-Lavie valve which is mounted on posts attached to a flange. The beam passes through the skimmer (4 mm opening diameter) to the interaction region where it is crossed with the pump and probe lasers (these are aligned perpendicular to the plane of the paper). The ion optics and flight tube are surrounded by a cylindrical μ-metal shield to protect the electrons from the magnetic field of the earth and the Maglev pump. A liquid nitrogen trap is suspended in detector side of the chamber to minimise the amount of background gas in the chamber and thus improve the quality of the photoelectron images.

Pump and probe lasers

After passing through the skimmer, the molecular beam was crossed at 90° by the path of the pump and probe lasers with central wavelengths in the UV region of the spectrum. These pump and probe lasers are produced as described in Section 2.2. Briefly, light pulses of 35 fs duration were produced at a 1 kHz repetition rate with central wavelength of 795 nm and 2.5 mJ per pulse (Coherent Legend regenerative amplifier seeded by a Coherent Mira Ti–sapphire oscillator, see Figs. 2.2 and 2.3). 0.75 mJ of this beam was used to pump each of two commercial optical parametric amplifiers and frequency

conversion units (OPA, Coherent OPerA, Fig. 2.4). These were used to create femtosecond pulses with central wavelengths of 254 nm and 240 nm. The energies of these pulses were of the order of a few μJ, and the spectral widths about 2 nm. For some of the experiments described in this chapter, light of central wavelength around 200 nm was used. This was generated using the third and fourth harmonic generation boxes (Fig. 2.5). The spectrum of these pulses at approx. 200 nm could not be measured using a grating spectrometer, but the central wavelength was estimated as 198.7 nm using the measured spectra of the two pulses that were used to generate the fourth harmonic.

In each experiment, one of the two beams (pump or probe) was sent onto a delay stage so that its path could be increased with respect to the other by a computer-controlled stage (PI MikroMove M-510.12) with μm (~10 fs) accuracy. After the delay line, the probe and pump beams were combined coaxially on a beamsplitter and focussed into the chamber, using a 25 mm focal length convex lens, through a glass window (see Fig. 4.5).

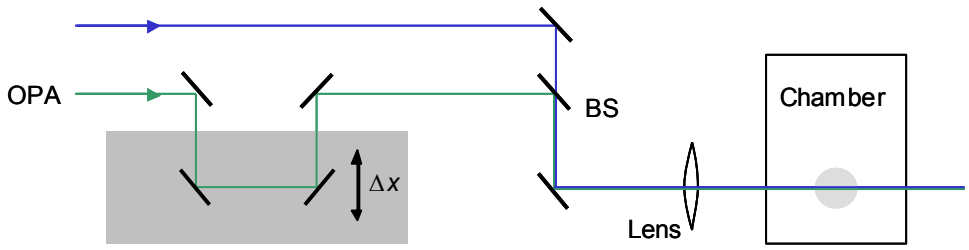

Figure 4.5 Illustration of the pump-probe experiment. The delay between the pump and probe pulses is set by the distance Δx, which was altered by moving the stage, upon which a pair of mirrors is mounted. Alignment of the stage motion axis parallel to the incoming and outgoing beam paths was crucial for accurate measurement of the delay, and to maintain the overlap of the two beams in the interaction region of the chamber (marked with a grey circle) where the lasers and molecular beam intersect.

An upper bound for the intensity of the beam in the interaction region was estimated using a Gaussian optics model as 8×10^{12} W cm^{-2}, so that there was no possibility of a strong laser electric field causing Stark shifting or ionisation. The power of the beam was also reduced so that there are not more than 20 electrons generated by the probe laser pulse in any one cycle of the experiment. This was to minimise any possible distortion of the photoelectron images by electron-electron interactions. Before reaching the interaction region, as the beam entered the chamber window, it passed through a set of homebuilt 4 mm diameter anodised aluminium baffles, and after the interaction region, the laser passed through a symmetrical arrangement of baffles in front of the exit chamber window. The baffles act to reduce the amount of laser scatter in the chamber. Use of the baffles, together with the camera gating (see below) meant that the number of photoelectron counts due to stray light, as measured when the laser was passing through the chamber without interacting with the molecular beam, was 1-2 per second.

Photoelectron imaging

The photoelectron imaging setup follows the standard Eppink and Parker velocity-map imaging (VMI) design.[18] A schematic of this is shown in Fig. 4.6. The basis of the VMI method is that when the laser and molecular beam interact, the *x*-*y* components of the initial velocities of the charged particles are projected onto *x*-*y* positions on a 2D detector in the *x*-*y* plane, regardless of the sign of the *z* component of their initial velocities. The *z* axis is defined by the flight direction, as shown in Fig 4.6, and in this frame of reference, the *x* and *y* axes are defined by the laser and molecular beam directions. All the particles with the same mass-to-charge (*m*/*z*) ratio arrive at the detector at the same time, and the mapping is also independent of the initial positions of the ions or electrons for interaction regions of widths of a few millimetres or less. The size of the interaction region is defined by the laser focal width, which has been calculated as between 10 and 40 μm, with an error dependent the visual estimate of the unfocussed beam diameter. The results that are presented in Section 4.4 were obtained from electron images, but it is worthy of note that VMI may be used to detect the velocity distribution of a range of ions, with time-gated detection of the different masses

of the ions, and the temporal coincidence of all particles with the same *m*/*z* was utilised in the characterisation of the beam by recording a mass spectrum, as in Fig. 4.3.

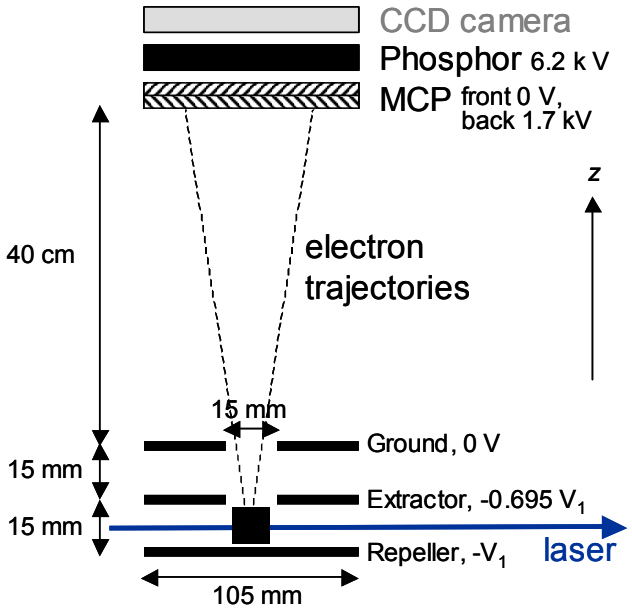

Figure 4.6 Diagram of the VMI photoelectron imaging setup used for photoelectron spectroscopy. The ion optics consist of three circular stainless steel plates: the repeller, extractor and a ground plate, that last of which is held at the same potential as the front of the multi-channel plate (MCP) detector to maintain the field-free flight tube. The lasers and molecular beam intersect perpendicularly in the interaction region (marked by a grey circle), directly between the repeller and extractor plates, and the resulting electrons are accelerated towards the ground plate from whence their trajectory to the detector is set. In the detector, the MCP detects and amplifies the electron impact so that an electron cascade is generated. The electron cascade then meets the phosphor screen and the resulting phosphorescence is recorded by the charge-coupled device (CCD) camera.

In this experiment, the laser and molecular beams cross in the interaction region between two stainless steel discs, the repeller and extractor plates (see Fig. 4.6). Together these plates act to accelerate the electrons produced by the probe laser ionisation: the extractor plate contains a hole to allow the electrons to leave the interaction region and move

towards the detector. After acceleration to the time-of-flight region by the ion optics, the electrons drift through the flight region and collide with the MCP, triggering an electron cascade that is accelerated towards the phosphor detector (Photek VID 240). The repeller is held at a more negative potential than the extractor, with the ratio between the two plates calibrated at 0.695. The experiment was designed with the nominal value of 0.7 for this ratio, and the optimal ratio, 0.695, was obtained by visual comparison of several Xenon images (see Fig. 4.8, below, for an example image) recorded with the ratio set at various values around 0.7. Decreasing the magnitude of the negative potentials on the repeller and extractor plates allows an expansion of the size of the image on the detector. In order to increase the resolution of any photoelectron velocity distribution it is necessary to maximise the spatial extent of the distribution on the detector. For these experiments two different settings of the repeller and extractor voltages were used. The repeller voltage was at -1500 V and the extractor voltage at -1043 V for photoelectron images recorded with pump and probe wavelengths of 254 and 240 nm, measuring photoelectron energies in the range 0 – 1.6 eV. For pump and probe wavelengths of 254 and 199 nm, measuring photoelectron energies from 0 – 3 eV, the repeller voltage was set at -2500 V and the extractor voltage at -1738 V. All the photoelectron images were retrieved from a 780 × 580 pixel CCD camera using commerical software (Photek IFS32).

4.3 Image processing and calibration

Background subtraction

Each image collected with the pump and probe pulses included electrons counts created by the pump-probe process as well as by a two-photon pump-pump process and a two-photon probe-probe process. These latter two ionisation processes are of no interest, and so they were removed by the subtraction of spectra recorded with only the pump laser and only the probe laser. A single photoelectron image was collected for typically 30 minutes, in which time 30 of each of the pump-probe, pump-only and probe-only images

were recorded for 20 seconds each, so that a single set of pump-probe, pump-only and probe-only images were recorded every minute. All of the three types of the spectra are subsequently combined, such that the composite background pump-pump plus probe-probe image was subtracted from the image recorded with both the pump and probe lasers, using an algorithm written in a macro within the camera software. The reason for collecting the sets of images over very short, 1 minute, cycles is to allow for the background subtraction to keep pace with the normal fluctuations in the power of the lasers.

Photoelectron image to photoelectron spectrum

2D angular velocity distributions were obtained from the measured 2D photoelectron velocity images using a polar Basex (pBasex) algorithm by Garcia *et al*.[19] Photofragment distributions are distributed in space, with respect to the polarisation of the light, as a series of Legendre polynomials.[20] The pBasex algorithm uses a sum of Gaussian-weighted Legendre polynomials as a basis set to model the measured distribution of photofragments. This method avoids using inverse Abel transforms, which are difficult to calculate, but relies instead on numerical calculation of only forward Abel transforms. Legendre polynomials of order 2 were used in the inversions in this chapter, because in a one-photon, linearly polarised process, the electron distribution will take the form of a second order Legendre polynomial.

From the 2D velocity distribution, a simple integration around the angular coordinate, θ, (see Fig. 4.7) produced a photoelectron distribution as a function of the radial coordinate, r (velocity). Conversion of the r coordinate of the distribution to r^2 gave a histogram of electrons as a function of energy (unscaled), and then the values in the histogram were scaled by $1/r$ to give a spectrum of photoelectron energies. The lower end of the energy scale was cut-off at 0.01 eV to remove the high intensity noise peak centred at the origin of the image that results from the pBasex inversion process. The photoelectron imaging inversion process is illustrated in Fig. 4.7 and an example of the data processing procedure is given in Fig. 4.8.

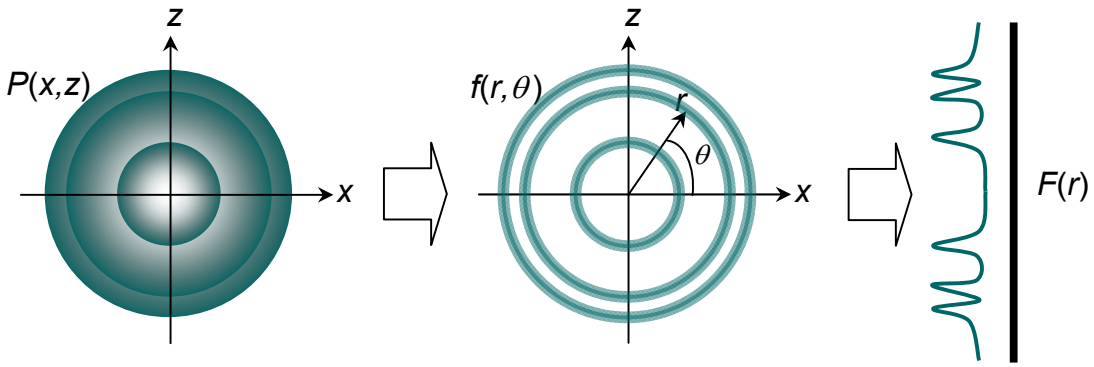

Figure 4.7 Illustration of the data analysis process that transforms the photoelectron velocity image into a photoelectron spectrum. Left: example photoelectron velocity image, $P(x,z)$. Centre: example 2D photoelectron velocity distribution, $f(r,\theta)$, obtained by pBasex (or other) image inversion algorithm. Right: example photoelectron velocity spectrum, $F(r)$, obtained by integration about θ. The coordinates r,θ, define the original 3D photoelectron velocity distribution as well as the 2D image due to the symmetry about the azimuthal angle, ϕ, produced by the polarisation of the laser parallel to the imaging detector. Symmetry about the θ coordinate is dependent on the angular momentum of the electron-wave emitted in the ionisation process, which is governed by the angular momenta of the species before and after ionisation and the number of photons involved in the ionisation process.

Calibration of the energy axis

Calibration of the energy axis was achieved using a pre-calibrated image, recorded using the same repeller and extractor voltages. Photoelectron images collected from ionisation of the Xe atom to the $^2P_{3/2}$ (12.13 eV) and $^2P_{1/2}$ (13.44 eV) cation levels were used as calibration images, *via* a two-photon resonance with a 6*p* Rydberg state of the neutral atom at 9.93 eV.

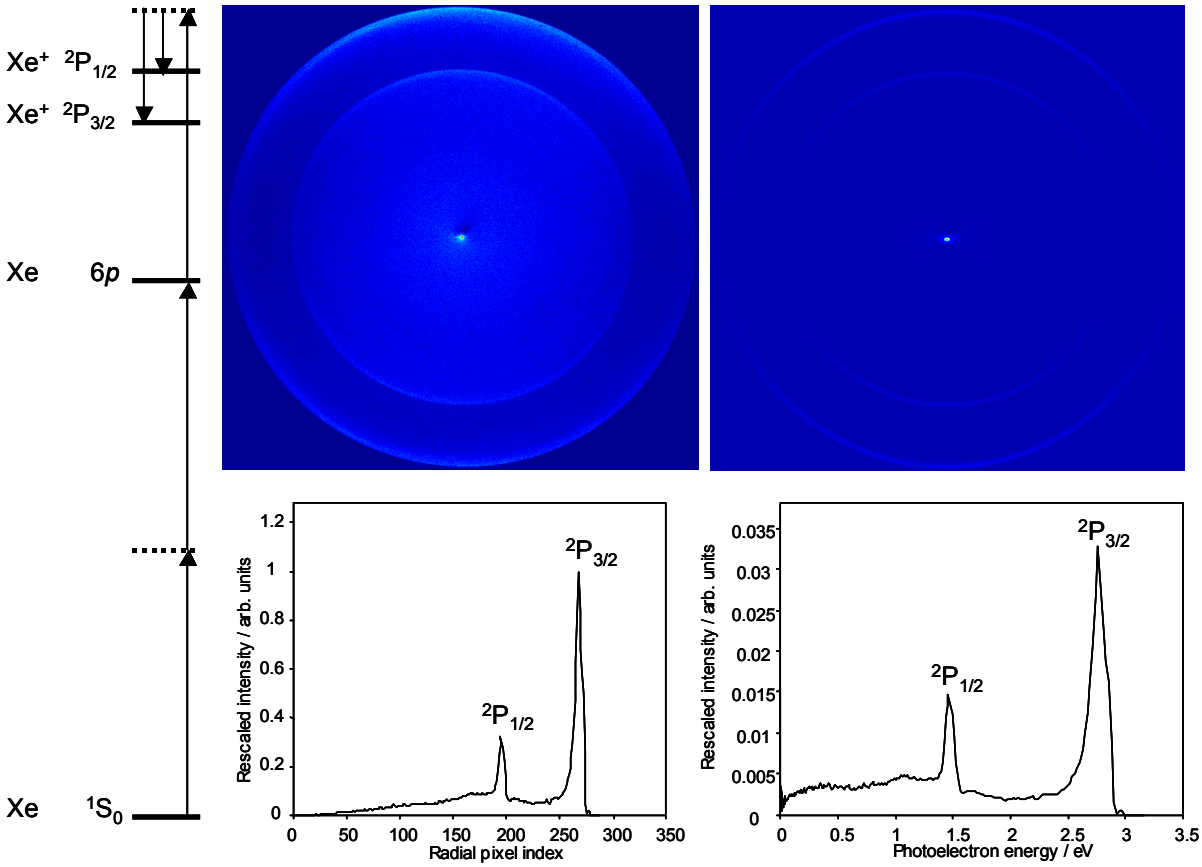

Figure 4.8 Example of the data processing procedure, using one of the Xe calibration images recorded with repeller voltage 2500 V and extractor voltage 1738 V. Left: photoionisation scheme in Xe *via* a 6*p* Rydberg resonance to produce two peaks from the $^2P_{1/2}$ and $^2P_{3/2}$ cation levels. Top centre: photoelectron image. Top right: the image after inversion by the pBasex program. Lower left: Radially integrated inverted photoelectron image. Lower right: photoelectron spectrum. To create the spectrum, the scale was converted to one that was linear in energy, the energy values were then assigned using the centre of the two peaks at 1.46 eV and 2.76 eV, and finally the intensity was scaled by the reciprocal of the pixel number and then normalised so that the integrated spectrum is equal to unity. Some residual styrene was present in the beam when these images were recorded; this can be seen as a low-level background in the spectrum.

Calibration of the pump-probe zero-of-time

The zero-of-time of the pump-probe delay was calibrated by recording a non-resonant two-photon ionisation energy-integrated photoelectron decay curve for nitric oxide. The resulting temporal structure in the decay is a cross-correlation of the laser pulse that defines the time zero (t_0) of the laser pulses in terms of a distance on the stage; at the maximum of the cross-correlation the path lengths of the pump and probe beams are equal. Measured cross-correlations full-widths at half maximum (FWHMs) varied over the course of the experiments, from about 176 fs to 287 fs, see Fig. 4.9.

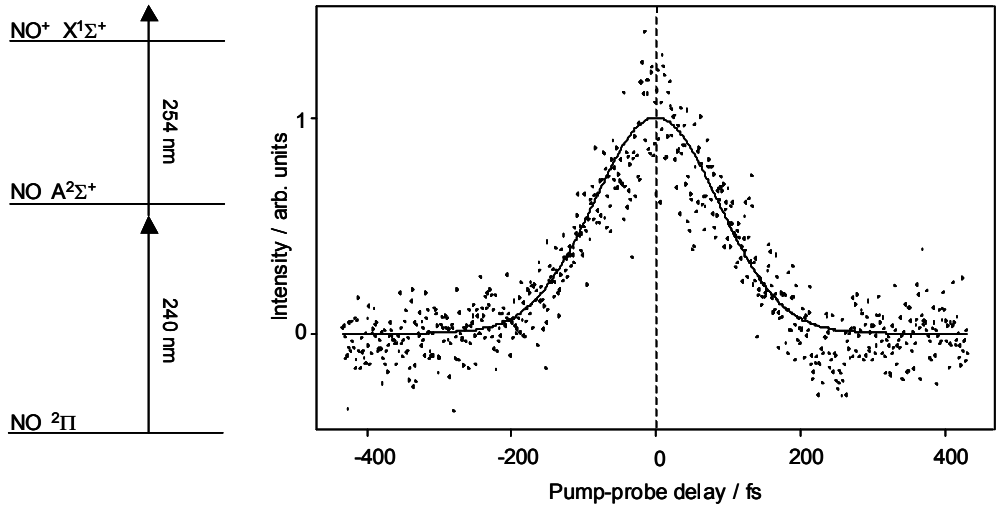

Figure 4.9 Cross-correlation of the pump and probe lasers, measured by two-photon ionisation of NO. An energy level scheme is shown on the left, and the total photoelectron count as a function of pump-probe delay is shown on the right. The full-width at half maximum (FWHM) of the cross-correlation fit (line) is 203 fs. This corresponds to 143 ± 25 fs as an average FWHM for each pulse of the pump and probe pulses, and the value of t_0 was calculated to within an error of 25 fs.

A final rescaling of the time-resolved styrene spectra was necessary because the pBasex program automatically normalises the photoelectron images. The integrated intensities of the resulting spectra at the different pump-probe delays were therefore scaled using an energy-integrated photoelectron count, measured as function of pump-probe delay. The

energy integrated photoelectron counts are presented with the photoelectron spectra in the next section.

4.4 Results and discussion

Four different time-resolved photoelectron spectroscopy experiments were carried out, with four different combinations of pump and probe beams, resulting in four sets of spectra. Some theory of the observation of electron and nuclear dynamics has already been described in the introduction (Chapter 1, Section 1.3). Briefly, the photoelectron spectrum measures the kinetic energy of the electron emitted upon ionisation of a photoexcited species. The photoelectron energy, eKE, will therefore be the difference between the total energy of the pump and probe photons, E_{pump} and E_{probe}, and the energy of the vibronic state of the resultant ion, $E\left(\mathrm{D}_n, \upsilon^+\right)$, relative to the ground state of the neutral,

$$\text{eKE} = E_{\text{pump}} + E_{\text{probe}} - E\left(\mathrm{D}_n, \upsilon^+\right). \tag{4.1}$$

From the measured photoelectron energies, the populations of the intermediate photoexcited states are then assigned using Koopmans' approximation and Franck-Condon arguments to infer, respectively, the electronic and vibrational components of the transition between the excited state and the ion. Generally, it is assumed that vibrational energy is conserved in the transition from the excited state to the ion, as discussed in Section 1.3, and this is known as the "$\Delta\upsilon = 0$ rule". This rule allows approximate photoelectron band energies to be predicted between excited states, and thus the TRPES bands can be assigned to first order, using the Koopmans' correlations to the cation states calculated at the ground state geometry as an approximation. This approximation has been used as an assignment method in other time-resolved experimental studies of styrene[21] and other molecules.[21-23] The four time-resolved photoelectron spectra, their assignments and some discussion are now presented.

240 nm pump, 254 nm probe

The time-resolved photoelectron spectrum of styrene recorded after excitation with a 240 nm femtosecond pulse and ionisation with a 254 nm femtosecond pulse is shown in Fig. 4.10, and a photoionisation energy scheme for this spectrum is given in Fig. 4.11. The pump-probe spectrum was recorded at various delays, to a maximum of over 50 ps, however the most interesting behaviour was observed only at shorter timescales and so for simplicity, only the spectra up to pump-probe delays of 250 fs are displayed in Fig. 4.10. It can be seen immediately in the time-resolved photoelectron spectra that there are two distinct timescales for the decay of the photoelectron bands. The higher energy photoelectrons, above about 1.0 eV, disappear rapidly and are all gone within 200 fs. The lower energy photoelectron band is much longer lived, having decayed after approximately 50 ps. These two different decay patterns are echoed by the biexponential fit parameters for the global photoelectron decay, which are listed in the caption in Fig. 4.10. These net decay parameters cannot exactly describe the decay of the two photoelectron bands, however, and indeed the high degree of error for one of the fitted decay lifetimes (τ_1 = 175 ± 221 fs) also motivates a more detailed look at the decay for different regions of the photoelectron spectra. (The high level of error in this fit parameter is probably due to the fact that the decay at the early times is very fast, and relatively few experimental points were obtained in this region of the global decay plot, see Fig. 4.10, top). The observed change in decay time with photoelectron energy is particularly worthy of further investigation because, within a simple model for the predicted photoelectron band energies, it is indicative of the presence of an ultrafast internal conversion, as will now be described.

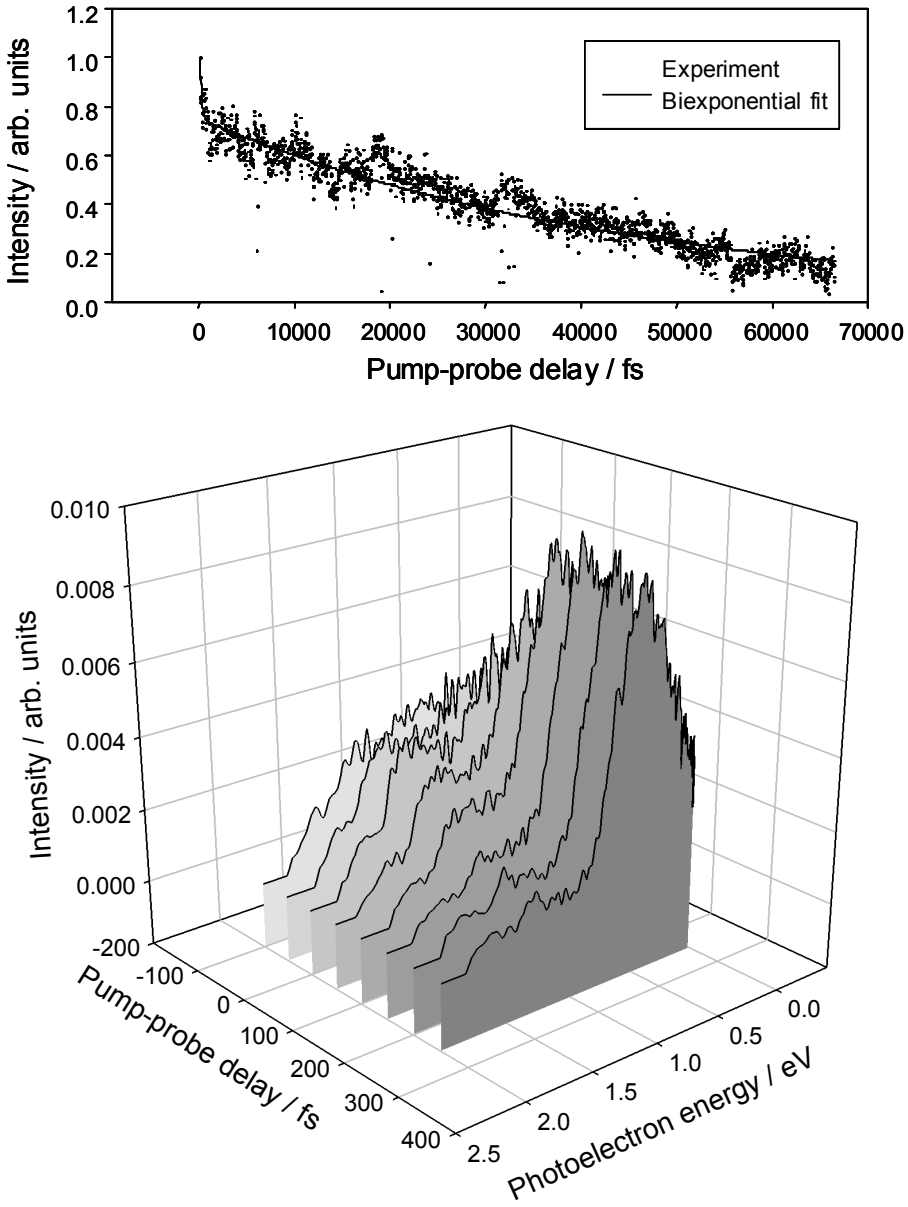

Figure 4.10 Time-resolved photoelectron spectrum of styrene recorded with a 240 nm pump and a 254 nm probe (lower part of figure). The graph at the top of the figure is the energy integrated photoelectron count, fitted with a biexponential function, used to calibrate the individual spectra shown above. The biexponential fit function was $y = a_1\exp[-(x-x_0)/\tau_1] + a_2\exp[-(x-x_0)/\tau_2]$, with x_0 fixed at 110 fs; the resulting optimal values of a_1, a_2, τ_1 and τ_2 are 0.25 ± 0.12, 0.75 ± 0.01, 175 ± 221 fs and 44.8 ± 1.2 ps respectively. The errors quoted here are two times the standard asymptotic errors produced by the fit optimisation carried out using Sigmaplot software.

Excitation of styrene with 240 nm light takes the molecule to the S_2 state, 2300 cm^{-1} above the zeroth vibrational level of the state, from where it may be ionised by 254 nm light to the D_0 or D_1 cation levels (see Fig 4.11 below). An internal conversion to the S_1 state is expected,[3-5,21] at which point the total vibrational energy in the S_1 state would be 6900 cm^{-1}, and from here it could also be ionised to the D_0 or D_1 cation states. Using the TDDFT/HCTH calculations in Chapter 3, Section 3.5, photoionisation correlations have been calculated for the S_2 and S_1 states. S_1 and S_2 are both expected to correlate with D_0 and D_1, but the ionisation correlation between the S_2 and D_1 wavefunctions is significantly smaller that of the S_1 and D_0 wavefunctions. Quantitatively, these calculated one-electron ionisation correlations can be considered to be approximate transition intensities for the photoionisation process; they are displayed for each possible transition between the neutral and cation states in Fig. 4.11. Using the same TDDFT calculations for the cation, together with the experimental vibrational 0-0 excitation energies for the S_1 and S_2 states, and assuming the $\Delta\upsilon = 0$ rule, estimates for the photoelectron energies arising from the transitions S_2-D_0, S_1-D_0, S_2-D_1 and S_1-D_1 have been calculated. These photoelectron energy estimates are illustrated in Fig. 4.11.

In accordance with the predicted photoelectron energy bands, selected portions of the photoelectron spectra displayed in Fig. 4.10 were integrated and the resulting photoelectron counts plotted as a function of pump-probe delay. The photoelectron energy bands predicted to be most intense, between 1.2 and 1.3 eV (the S_2-D_0 transition), between 0.7 and 0.8 eV (the S_1-D_0 transition), and below 0.1 eV (the S_1-D_1 transition), are shown in Fig. 4.12. Most of the photoelectron counts in the S_2 (1.2-1.3 eV) band are gone before 200 fs, and the two S_1 bands both increase in intensity as the S_2 band decreases. This difference in decay behaviour between the S_2 and S_1 bands confirms that an ultrafast internal conversion has been observed. The possibility that the 0.7-0.8 eV band contains some of the S_2-D_1 transition photoelectrons must not be discounted but this transition is expected to be quite weak compared to the S_1-D_0 transition with which it might overlap. In another, similar, analysis, Gaussians were used to fit the different photoelectron bands and a plot of the Gaussian heights *vs.* time

revealed the same pattern: fast decay of a high photoelectron band, and much slower decay of the low energy band.

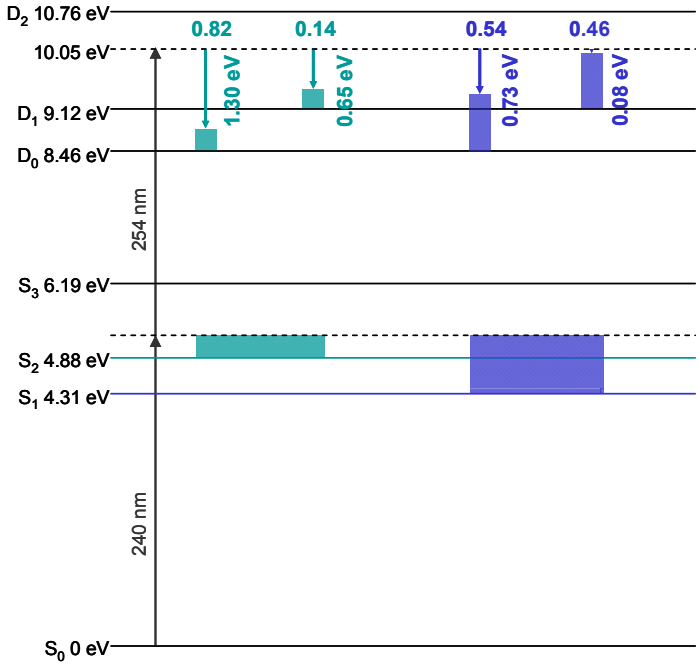

Figure 4.11 Energy level scheme for the pump-probe photoionisation experiment on styrene with 240 nm pump and 254 nm probe photons. Estimates for the energies of four different photoelectron bands are marked, from left to right, S_2-D_0, S_2-D_1, S_1-D_0 and S_1-D_1, assuming the conservation of vibrational energy in the ionisation process. The predicted relative intensities of the transitions are also marked on the diagram, above the photoelectron kinetic energy for each transition. These were calculated as reported in Chapter 3 (Section 3.5, Table 3.3).

A small note of caution must be added here over the interpretation of the very short timescale sections of the photoelectron spectra: as shown in Fig. 4.9, the cross-correlation FWHM for the 254 nm and 240 nm pulses is about 200 fs, and so the intensity of the photoelectron signal within the pump-probe overlap region (between about –100 and +100 fs) will be a combination of pump-probe and probe-pump signals. This caveat does not, however, affect the interpretation of the results given so far: even

outside the pump-probe overlap region, the S_1 photoelectron intensities increase as the S_2 photoelectron signal decreases.

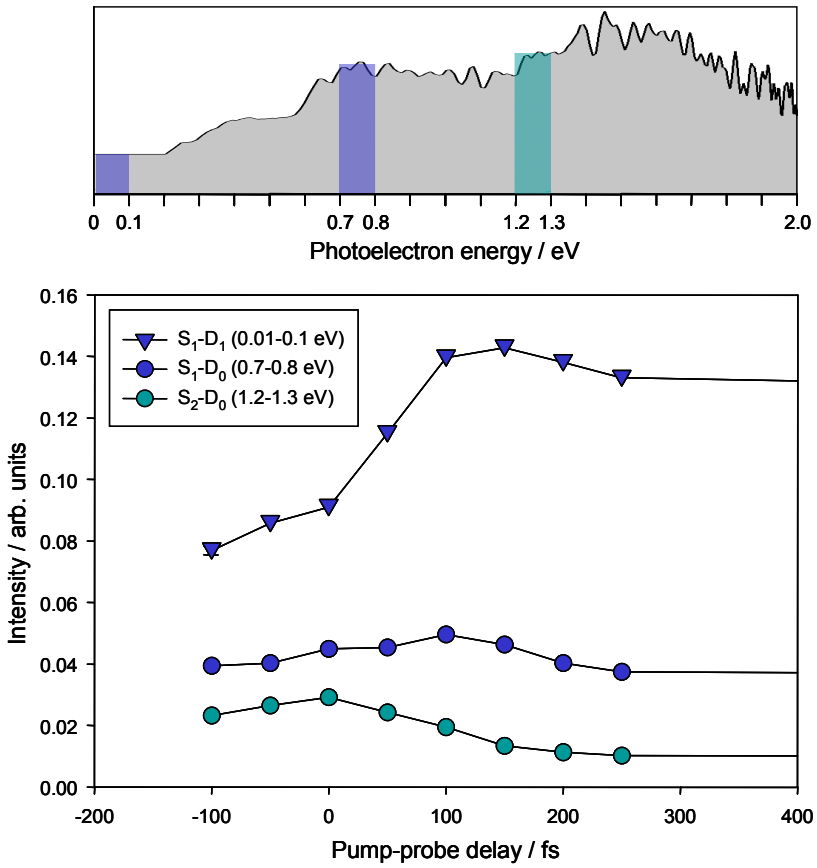

Figure 4.12 Integrated regions from the time-resolved photoelectron spectrum, recorded with a 240 nm pump and 254 nm probe corresponding to the neutral-cation state transitions predicted to be most intense. These expected photoelectron band energies were obtained using the $\Delta\upsilon = 0$ rule, as illustrated in Fig. 4.11. An illustration of the integration process for an example spectrum is shown at the top, and below this the photoelectron band integrated intensities are plotted as a function of pump-probe delay. The errors in the intensity are plus or minus two times the RMS of the differences of the photoelectron intensities and average photoelectron intensities for the band. The largest of these very small errors for each decay curve is plotted on the point at pump-probe delay equal to –100 fs. The lines through the data points are to guide the eye.

254 nm pump, 240 nm probe

Pumping styrene with a 254 nm photon gives the molecule less energy than the 240 nm photon, and takes it just to the origin of the S_2 state at 4.88 eV. A time-resolved photoelectron spectrum for the most interesting short values of pump-probe delays is shown in Fig. 4.13. Outside of the pump-probe pulse overlap region, for delays of 100 fs and greater, the whole photoelectron spectrum looks fairly uniform, and is centred at 0.8 eV; no obvious differences in timescale as a function of photoelectron energy can be seen, as might be expected if an internal conversion were present. The global decay was fit with a sum of exponentials centred at -110 fs, with lifetimes 294 ± 37 fs and 65.1 ± 11.0 ps, and weights 0.83 ± 0.06 and 0.17 ± 0.01 respectively. As in the case of the 240 nm pump, 254 nm probe spectrum already discussed, photoelectron band energies have been calculated from Eq. 4.1 and assuming the conservation of vibrational energy in the ionisation process, and the results are displayed are illustrated schematically in Fig. 4.14 below.

Integrations of three photoelectron bands corresponding approximately to the most intense of the predicted transitions from S_2 and S_1 to the energetically accessible cation states are illustrated in Fig. 4.15. All of the photoelectron bands show a fast decay. The band corresponding to ionisation from S_2 contains two components: one very small and short-lived, the other extremely long-lived. In fact the shorter timescale feature of this band probably indicates that it is due to a probe-pump process rather than a pump-probe process. The small amount of very long-lived photoexcited styrene apparent in this band could be due to a very small amount of S_2 that has been excited with no vibrational energy, resulting in an inability of this population to decay *via* IVR followed by non-adiabatic crossings. The lack of intensity in the S_2 band is not surprising: the pump energy in this experiment (254 nm, 4.88 eV) is exactly the energy of the 0-0 transition from S_0 to S_2, and as the Franck-Condon region for S_2 appears to be at around 5.11 eV, (the maximum in S_2 band in the room temperature absorption spectrum is at 5.21 eV, see Fig. 3.2, but the maximum in the absorption of the jet-cooled spectrum is at 5.11 eV[9]) it is unsurprising that there is not much excitation of this state using 254 nm radiation.

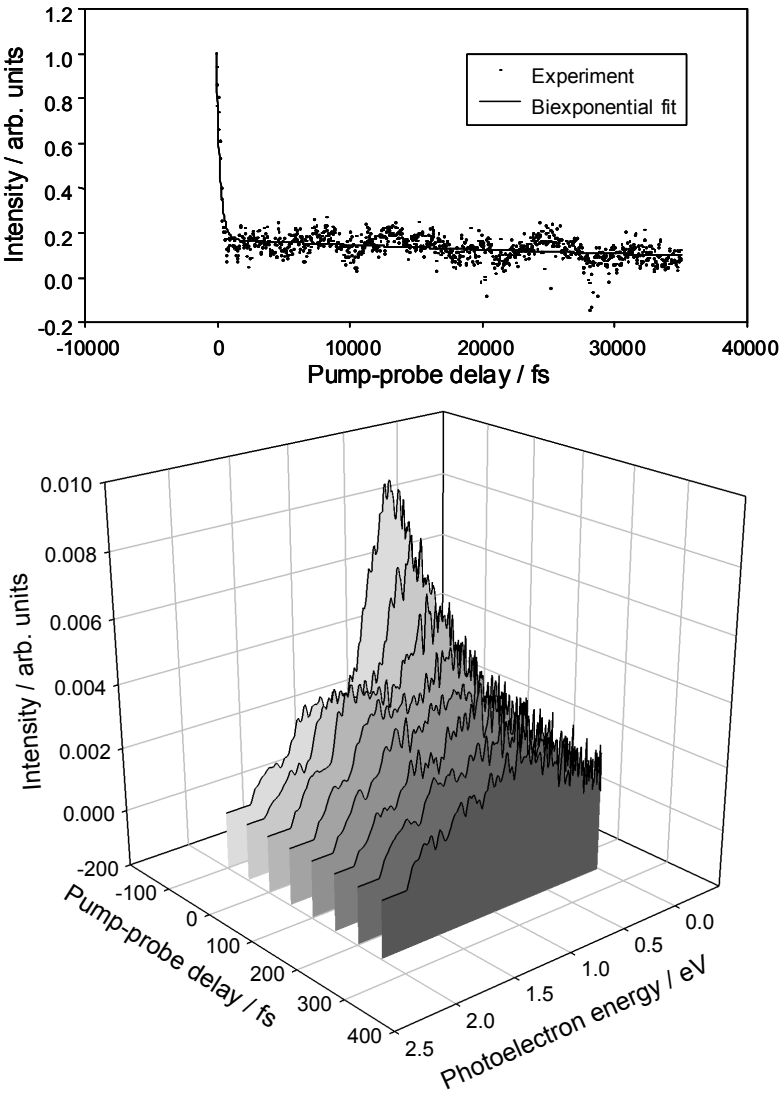

Figure 4.13 Time-resolved photoelectron spectrum of styrene recorded with a 254 nm pump and a 240 nm probe (lower part of figure). The graph at the top of the figure is the energy integrated photoelectron count, fitted with a biexponential function, used to calibrate the individual spectra shown above. The biexponential fit function was $y = a_1\exp[-(x-x_0)/\tau_1] + a_2\exp[-(x-x_0)/\tau_2]$, with x_0 fixed at -110 fs; the resulting optimal values of a_1, a_2, τ_1 and τ_2 are 0.83 ± 0.06, 0.17 ± 0.01, 294 ± 37 fs and 65.1 ± 11.0 ps respectively. The errors quoted here are two times the standard asymptotic errors produced by the fit optimisation carried out using Sigmaplot software.

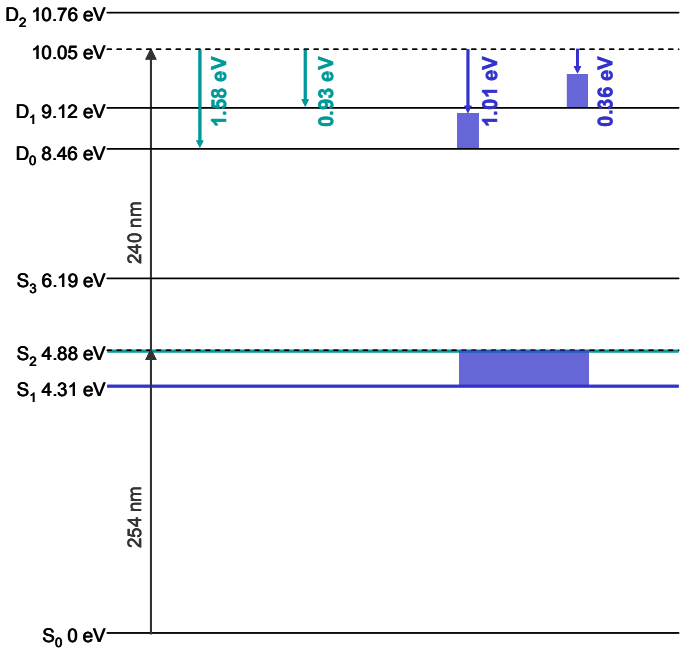

Figure 4.14 Energy level scheme for the pump-probe photoionisation experiment on styrene with 254 nm pump and 240 nm probe photons. Estimates for the energies of four different photoelectron bands are marked, from left to right, S_2-D_0, S_2-D_1, S_1-D_0 and S_1-D_1, assuming the conservation of vibrational energy in the ionisation process. The predicted relative intensities of the transitions are also marked on the diagram, above the photoelectron kinetic energy for each transition. These were calculated as reported in Chapter 3 (Section 3.5, Table 3.3).

The apparent lack of S_2 intensity and the fact that no internal conversion is observed from this state in this work is in contrast to the results of experiments carried out by another group in which the observation of an internal conversion in styrene after excitation with 254.3 nm light was reported.[21] The speed of the decay of S_1 observed here, after excitation with 254 nm (4600 cm^{-1} vibrational energy in S_1), compared to the decay from S_1 after excitation with 240 nm (previous experiment) is probably a function of the dependence of the decay channel on IVR. This is discussed in more detail in the next section, 4.5.

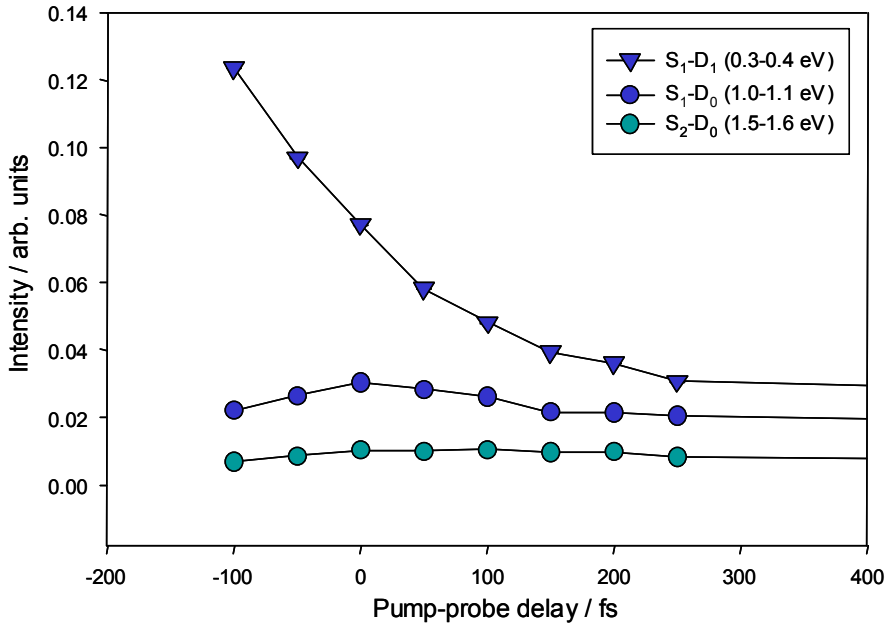

Figure 4.15 Integrated regions from the time-resolved photoelectron spectrum, recorded with a 254 nm pump and 240 nm probe corresponding to the neutral-cation state transitions predicted to be most intense. These expected photoelectron band energies were obtained using the $\Delta\upsilon = 0$ rule, as illustrated in Fig. 4.14. The photoelectron band integrated intensities are plotted as a function of pump-probe delay. Errors were calculated as plus or minus two times the RMS of the differences of the photoelectron intensities and average photoelectron intensities for the band; they are, however, smaller than the size of the plotted points in all cases. The lines through the data points are to guide the eye.

254 nm pump, 199 nm probe

In order to confirm that no excitation to the S_2 state is possible when pumping styrene with femtosecond laser light of central wavelength 254 nm, a second experiment with this pump wavelength but with a different probe wavelength (199 nm) was carried out and is now analysed. The resulting photoelectron spectrum (Fig. 4.16) has a very similar structure to that for 254 nm pump and 240 nm probe (Fig. 4.13). This rules out the possibility that structure in the ionisation continuum could contribute significantly to the dynamics observed in the time-resolved spectra in the case of pumping styrene with 254 nm light.

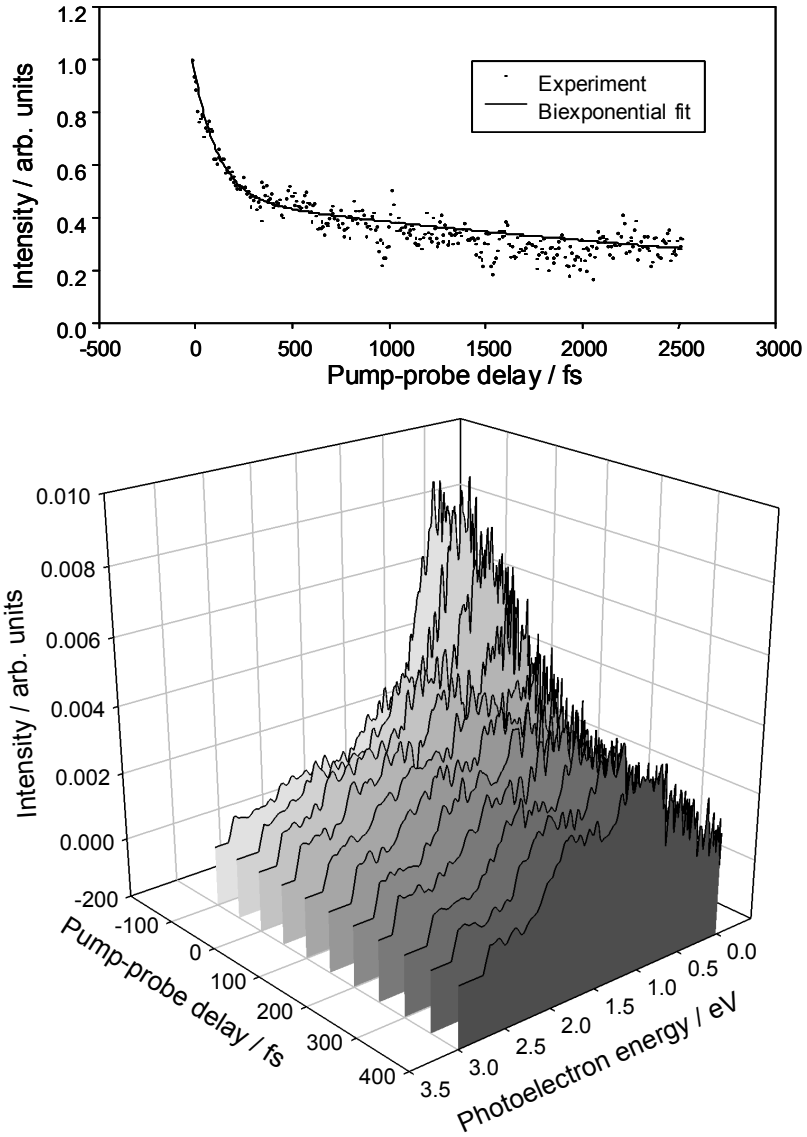

Figure 4.16 Time-resolved photoelectron spectrum of styrene recorded with a 254 nm pump and a 199 nm probe (lower part of figure). Spectra at pump-probe delays up to 1.2 ps were recorded, but only the more interesting short-timescale spectra are plotted here for clarity. The graph at the top of the figure is the energy integrated photoelectron count, fitted with a biexponential function, used to calibrate the individual spectra shown above. The biexponential fit function was $y = a_1\exp[-(x-x_0)/\tau_1] + a_2\exp[-(x-x_0)/\tau_2]$, with x_0 fixed at -16 fs; the resulting optimal values of a_1, a_2, τ_1 and τ_2 are 0.53 ± 0.04, 0.47 ± 0.02, 123 ± 20 fs and 5.0 ± 0.7 ps respectively. The errors quoted here are two times the standard asymptotic errors produced by the fit optimisation carried out using Sigmaplot software.

A photoexcitation scheme for the 254 nm pump, 199 nm probe scheme is given in Fig. 4.17. Although higher ionisation channels are energetically within reach of the 199 nm probe, these are not observed because of unfavourable Koopmans' correlations with the S_1 and S_2 states of the neutral molecule. As for the other data, integrated photoelectron bands corresponding to the predicted energies given in Fig. 4.17 are plotted in Fig. 4.18.

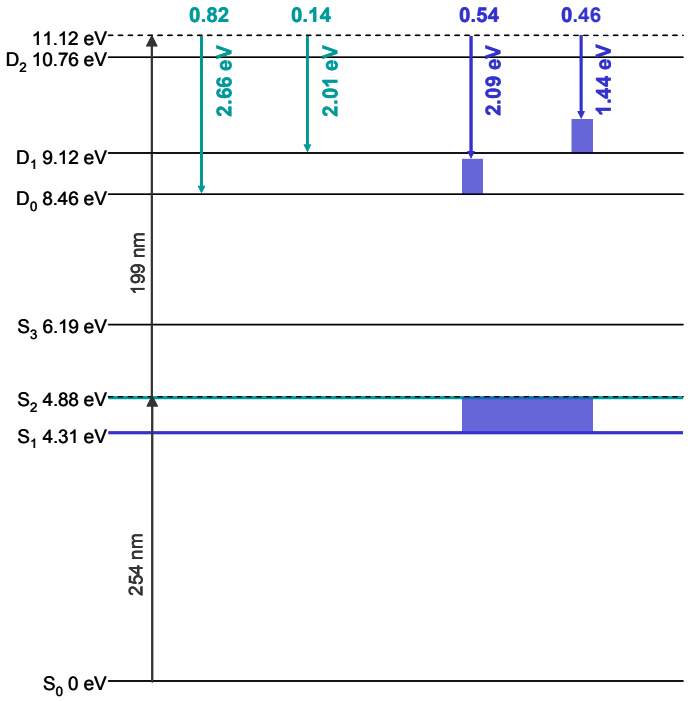

Figure 4.17 Energy level scheme for the pump-probe photoionisation experiment on styrene with 254 nm pump and 199 nm probe photons. Estimates for the energies of four different photoelectron bands are marked, from left to right, S_2-D_0, S_2-D_1, S_1-D_0 and S_1-D_1, assuming the conservation of vibrational energy in the ionisation process. The predicted relative intensities of the transitions are also marked on the diagram, above the photoelectron kinetic energy for each transition. These were calculated as reported in Chapter 3 (Section 3.5, Table 3.3).

The amount of photoelectrons in the band from the S_2 state is very small, as expected, and seems not to decay very fast; this could because, as for the previous experiment, decay of this population, which has zero vibrational energy, is very slow. The S_1-D_1 band appears to decay less quickly when probed with 199 nm (Fig. 4.18) compared with

when probed with 240 nm (Fig. 4.15). The reason for this may be that there is some slight difference in the ionisation dynamics after excitation to S_1 with these two wavelengths.

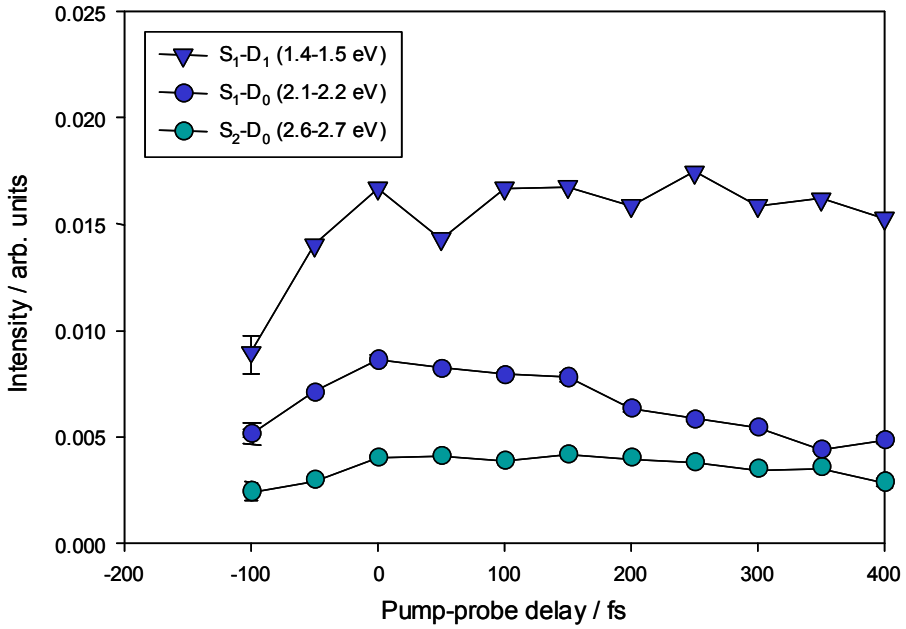

Figure 4.18 Integrated regions from the time-resolved photoelectron spectrum, recorded with a 254 nm pump and 199 nm probe corresponding to the neutral-cation state transitions predicted to be most intense. These expected photoelectron band energies were obtained using the $\Delta\upsilon = 0$ rule, as illustrated in Fig. 4.17. The photoelectron band integrated intensities are plotted as a function of pump-probe delay. The errors, the largest of which for each decay curve is plotted on the point at pump-probe delay equal to –100 fs, are plus or minus two times the RMS of the differences of the photoelectron intensities and average photoelectron intensities for the band. The lines through the data points are to guide the eye.

199 nm pump, 254 nm probe

Pumping styrene with a 199 nm photon allows excitation into an excited state higher than S_2. The exact energy of the S_3 state has not yet been determined experimentally, but high-level *ab initio* calculations in the literature give a bright valence excited state at 6.19 eV.[24] Photoelectron spectra were recorded using a 199 nm pump pulse together with a 254 nm probe pulse and these are plotted in Fig. 4.19.

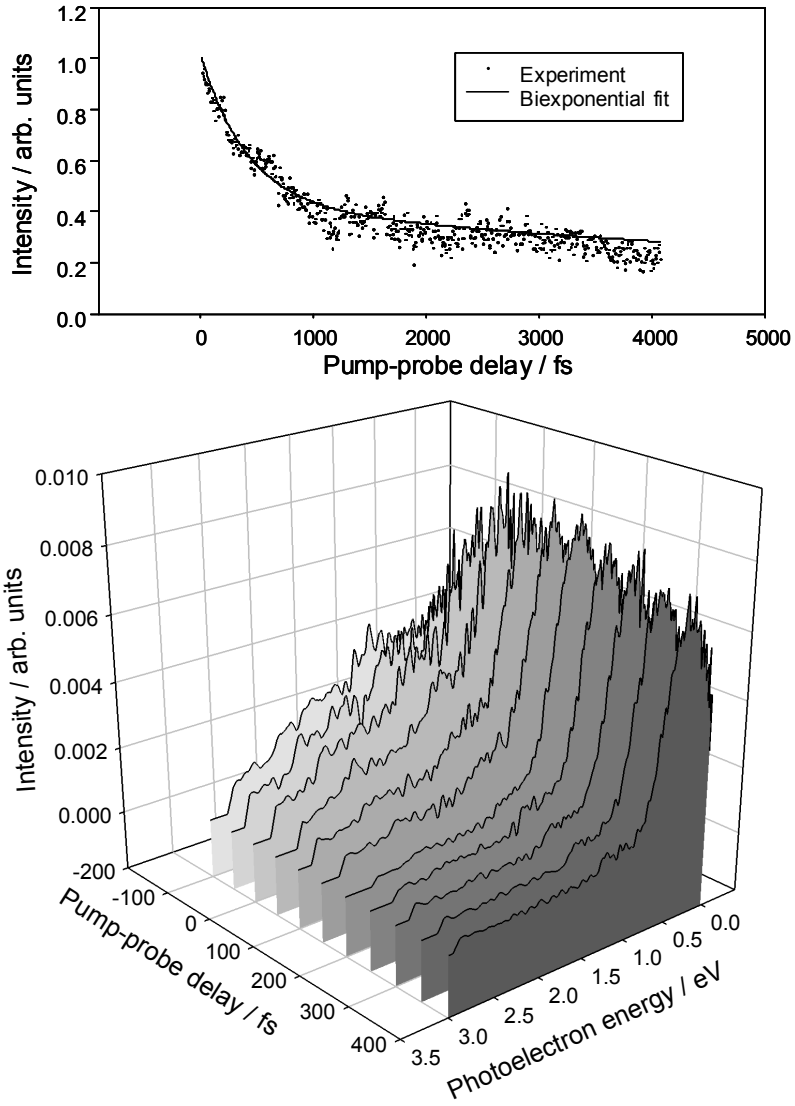

Figure 4.19 Time-resolved photoelectron spectrum of styrene recorded with a 199 nm pump and a 254 nm probe (lower part of figure). Spectra at pump-probe delays up to 1.8 ps were recorded, but only the more interesting short-timescale spectra are plotted here for clarity. The graph at the top of the figure is the energy integrated photoelectron count, fitted with a biexponential function, used to calibrate the individual spectra shown above. The biexponential fit function was $y = a_1\exp[-(x-x_0)/\tau_1] + a_2\exp[-(x-x_0)/\tau_2]$, with x_0 fixed at +16 fs; the resulting optimal values of a_1, a_2, τ_1 and τ_2 are 0.58 ± 0.03, 0.42 ± 0.03, 417 ± 36 fs and 10.0 ± 2.4 ps respectively. The errors quoted here are two times the standard asymptotic errors produced by the fit optimisation carried out using Sigmaplot software.

The total photoelectron decay was fit to a biexpoential with approximately equal weight to two decay times of 417 ± 36 fs and 10.0 ± 2.4 ps (see details in Fig. 4.19). Model photoelectron energy bands have been calculated using the theoretical value for the vertical excitation energy of the S_3 state, the energies of the lower state origins at 4.88 eV and 4.31 eV, and the excited cation state energies from the TDDFT calculations, as before, and are illustrated in Fig. 4.20. The neutral and cation TDDFT calculations reveal that the S_3 state correlates with the D_0, D_1, and very slightly to the D_2 ion states (Chapter 3, Table 3.3).‡

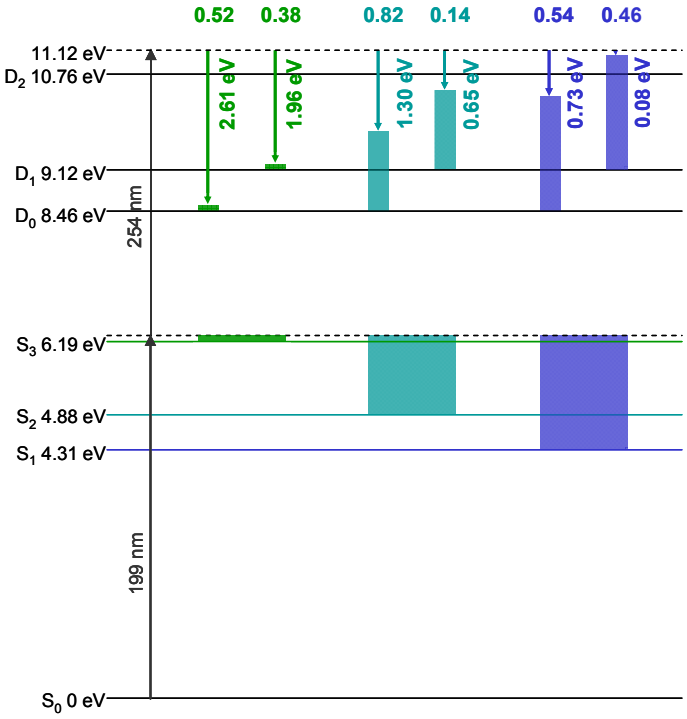

Figure 4.20 Energy level scheme for the pump-probe photoionisation experiment on styrene with 199 nm pump and 254 nm probe photons. Estimates for the energies of six different photoelectron bands are marked, from left to right, S_3-D_0, S_3-D_1, S_2-D_0, S_2-D_1, S_1-D_0 and S_1-D_1, assuming the conservation of vibrational energy in the ionisation process. The predicted relative intensities of the transitions are also marked on the diagram, above the photoelectron kinetic energy for each transition. These were calculated as reported in Chapter 3 (Section 3.5, Table 3.3).

‡ These S_3 correlations should be viewed with caution, however, because the energy given by the TDDFT calculation for the S_3 valence state does not agree with the high level *ab initio* results, as mentioned in Section 3.4.

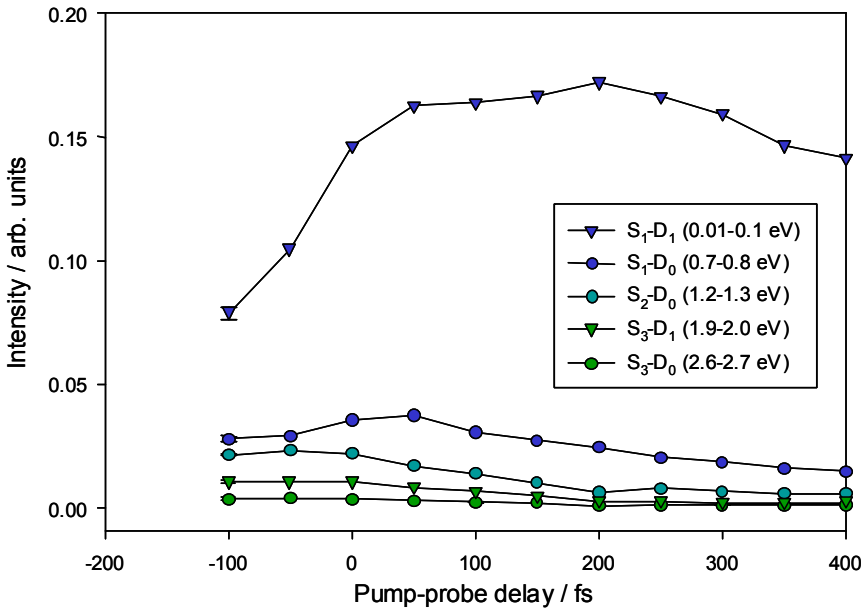

Figure 4.21 Integrated regions from the time-resolved photoelectron spectrum, recorded with a 199 nm pump and 254 nm probe corresponding to the neutral-cation state transitions predicted to be most intense. These expected photoelectron band energies were obtained using the $\Delta\upsilon = 0$ rule, as illustrated in Fig. 4.20. The photoelectron band integrated intensities are plotted as a function of pump-probe delay. The errors, the largest of which for each decay curve is plotted on the point at pump-probe delay equal to –100 fs, are plus or minus two times the RMS of the differences of the photoelectron intensities and average photoelectron intensities for the band. The lines through the data points are to guide the eye.

Integrated photoelectron bands over energies corresponding to the bands predicted to be most intense, including the S_3-D_0 and S_3-D_1 transitions, are plotted in Fig. 4.21. The decay of the S_1 photoelectron bands is clearly quite different to those of the S_2 and S_3 bands: for S_1 the intensity increases after the zero-of-time. As for the 240 nm pump, 254 nm probe data, the different decay of the photoelectron bands is obvious by looking at the photoelectron spectra (Fig. 4.19), where the photoelectron intensity for energies above about 1 eV fall off early on, apparently after about 200 fs. The difference in the time decay of the S_2 and S_3 bands is not significant, and the main difference between the bands seems to be their relative intensity. It is not therefore possible to say definitely

that an S_3/S_2 internal conversion is observed in these photoelectron spectra. The first state populated by the 199 nm probe is definitely S_3; the precise position of S_3 has not yet been identified, but the third band in the UV spectrum of styrene is very strong, and 199 nm is within that band, which has its maximum at around 200 mn (see Fig. 3.2). If a predicted theoretical vertical energy at 6.19 eV[24] is taken as approximately the zero-point energy for the state, excitation with 199 nm gives the molecule at least 300 cm^{-1} of vibrational energy. This is sufficient energy to allow the molecule to decay quickly to the S_2 state, and it is likely that the decay of S_3 to S_2 is too fast to be observable on the timescale of this experiment.

4.5 Conclusions

These experiments demonstrate that internal conversion in the styrene molecule can be observed using TRPES; the internal conversion between S_2 and S_1 is unambiguous, and is apparent simply from the looking at the experimental spectra in Fig. 4.10. The predictions for the photoelectron energies from the TDDFT calculations of the cation states are in fairly good agreement with the experimental bands. The internal conversion from S_2 is observed when the molecule is pumped with 240 nm, with approximately 2300 cm^{-1} vibrational energy in S_2, but not when pumped with 254 nm at the S_2 origin. When pumped with light at 199 nm (~300 cm^{-1} vibrational energy in S_3) more complex processes occur, and the time-dependence of the spectra indicates that some internal conversion may occur. As already discussed, the possibility that the theoretical value for the S_3 state is not correct, and therefore that the excitation with 199 nm light is not to S_3 but to highly excited S_2 is an unlikely one because 199 nm lies well within the third band in the absorption spectrum of styrene. A fast decay between S_3 and S_2 followed by a slower IC to S_1 seems likely, and is more probable than a slower decay to S_2 followed by a faster decay to S_1 because of the more favourable energy difference between S_2 and S_3 than between S_2 and S_1.

The decay pathways from S_2 described by Bearpark *et al.*[5] and Amatatsu[3] both link two conical intersections, an S_2/S_1 CI and an S_1/S_0 CI. Fast decay at the first CI would explain the initial ultrafast decay observed after excitation to the S_2 state with 240 nm light (Fig. 4.10). The slow decay of the S_1 energy photoelectron bands would imply that the subsequent decay from S_1 has some barrier when approached directly from S_2 (Fig. 4.12). The direct decay from S_1 (254 pump, see Fig. 4.13) is very fast, implying that an S_1/S_0 CI is directly accessible from the S_1 Franck-Condon region. Some change of geometry must occur either after the S_2/S_1 CI, and the decay-time difference for direct (254 nm pump) and indirect (240 nm pump) decay from S_1 is a function of the speed of IVR in the S_1 state. Bearpark *et al.* found an S_2/S_1 CI with a twisted quinoid structure: the outer CH_2 on the ethylene group is rotated out of the plane by about 40°. Two S_1/S_0 CIs were located by Bearpark *et al.* with quite distorted geometries. Amatatsu describe photochemical pathways from the S_2/S_1 CI to a stable S_1 geometry, followed by emission or decay *via* an S_1/S_0 CI with a slightly different structure than those predicted by Bearpark *et al.* In any of the possible theoretical S_1/S_0 CIs, the geometry change from the S_2/S_1 CI geometry is significant, and decay at the second CI would thus depend on IVR. IVR on a long (ns) timescale in S_1 as observed by Zewail and co-workers[10] is likely, and this explains the long lifetime observed for S_1, following S_2-S_1 IC, in these results. The possible decay paths from S_2 are illustrated in Fig. 4.22.

An accurate experimental energy for the S_3 origin needs to be determined to allow for a better model of the experimental data shown in Fig. 4.19. The other spectra, in Figs. 4.10, 4.13 and 4.16 are fairly well understood, as discussed above. The styrene S_2/S_1 internal conversion reported here is worthy of further more detailed modelling, using more parameters from electronic structure theory. In the analysis presented here, the cation excitation energies were calculated using the methods described in Section 3.5, but the arguments about the geometrical effects on decay timescales are from theoretical models that need reinvestigation with more rigorous methods; specifically, the geometries of the relevant conical intersections need re-calculating with methods that give a more balanced treatment of the electronic states involved. In the future, it is

hoped that the *ab initio* CASSCF/RASSCF methods that were used in Section 3.4 to attempt to calculate the vertical excitation energies of the singlet states of styrene in the Franck-Condon region can be used to study the geometries of conical intersections on the photochemical pathway from S_2. The Koopmans' analysis used to predict photoelectron energy band intensities is only strictly true for the Franck-Condon region, as noted at the beginning of Section 4.4 and therefore a better understanding of the spectra could be given if the ionisation correlations were calculated at different geometries along a theoretical predicted decay pathway.

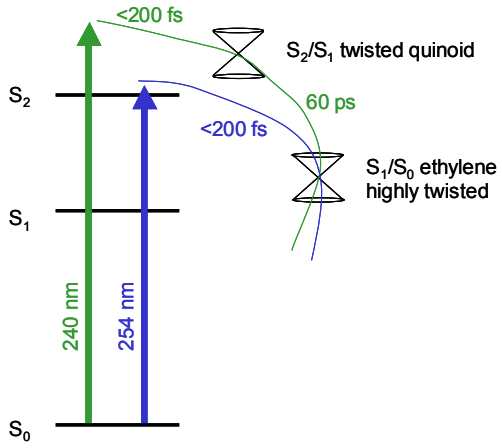

Figure 4.22 Energy level scheme and schematic illustration of the two excited state decay paths of S_2 styrene after excitation with 240 nm and 254 nm ultrafast pulses. Excitation to S_2 with 240 nm femtosecond pulses is followed by a fast decay to S_1 and then a slow IVR-dependent decay to S_0. Excitation to S_1 with 254 nm femtosecond light is followed by fast decay to S_0.

References

1 A. D. G. Nunn, R. S. Minns, M. J. Bearpark *et al.*, Physical Chemistry Chemical Physics, in preparation.

2 Y. Amatatsu, Chemical Physics Letters 344 (1-2), 200 (2001).

3 Y. Amatatsu, Journal of Computational Chemistry 23 (10), 950 (2002).

4 V. Molina, M. Merchan, B. O. Roos *et al.*, Physical Chemistry Chemical Physics 2 (10), 2211 (2000).

5 M. J. Bearpark, M. Olivucci, S. Wilsey *et al.*, Journal of the American Chemical Society 117 (26), 6944 (1995).

6 R. Bonneau, Journal of the American Chemical Society 104 (10), 2921 (1982); R. Bonneau, Journal of Photochemistry 10 (6), 439 (1979).

7 K. P. Ghiggino, K. Hara, K. Salisbury *et al.*, Journal of Photochemistry 8 (4), 267 (1978); K. P. Ghiggino, K. Hara, K. Salisbury *et al.*, Journal of the Chemical Society-Faraday Transactions Ii 74, 607 (1978); K. P. Ghiggino, D. Phillips, K. Salisbury *et al.*, Journal of Photochemistry 7 (2), 141 (1977); R. P. Steer, M. D. Swords, P. M. Crosby *et al.*, Chemical Physics Letters 43 (3), 461 (1976).

8 K. P. Ghiggino, K. Hara, G. R. Mant *et al.*, Journal of the Chemical Society-Perkin Transactions 2 (1), 88 (1978).

9 D. G. Leopold, R. J. Hemley, V. Vaida *et al.*, Journal of Chemical Physics 75 (10), 4758 (1981).

10 J. A. Syage, F. Aladel, and A. H. Zewail, Chemical Physics Letters 103 (1), 15 (1983).

11 L. D. Ziegler and C. Carotsis, Chemical Physics Letters 123 (3), 175 (1986).

12 J. M. Hollas, E. Khalilipour, and S. N. Thakur, Journal of Molecular Spectroscopy 73 (2), 240 (1978); J. M. Hollas and T. Ridley, Chemical Physics Letters 75 (1), 94 (1980); J. M. Hollas and T. Ridley, Journal of Molecular Spectroscopy 89 (1), 232 (1981).

13 R. J. Hemley, U. Dinur, V. Vaida *et al.*, Journal of the American Chemical Society 107 (4), 836 (1985).

14 M. H. Hui and S. A. Rice, Journal of Chemical Physics 61 (3), 833 (1974).

15 U. Even and N. Lavie, (2008).

16 *Section II.A* in R. E. Smalley, D. H. Levy, and L. Wharton, Journal of Chemical Physics 64 (8), 3266 (1976).

17 M. S. El-Shall, Accounts of Chemical Research 41 (7), 783 (2008).

18 A. T. J. B Eppink and D. H. Parker, Review of Scientific Instruments 68 (9), 3477 (1997).

19 G. A. Garcia, L. Nahon, and I. Powis, Review of Scientific Instruments 75 (11), 4989 (2004).

20 B. J. Whitaker (Ed.), *Imaging in Molecular Dynamics*, (Cambridge, 2003).

21 S. H. Lee, K. C. Tang, I. C. Chen *et al.*, Journal of Physical Chemistry A 106 (39), 8979 (2002).

22 V. Blanchet, M. Z. Zgierski, T. Seideman *et al.*, Nature 401 (6748), 52 (1999).

23 B. J. Kim and P. M. Weber, Journal of Physical Chemistry 99 (9), 2583 (1995).

24 V. Molina, B. R. Smith, and M. Merchan, Chemical Physics Letters 309 (5-6), 486 (1999).

Chapter 5

Conclusion

This chapter consists of some analysis of the outcomes of each of the three projects described in the previous three chapters - UV pulse shaping, theoretical electronic spectroscopy of styrene, and time-resolved photoelectron spectra of styrene - as individual studies, and together as a global project.

Ultraviolet femtosecond pulse shaping and characterisation for coherent control

In Chapter 2 the capabilites of the new UV pulse shaper were fully demonstrated using the XFROG characterisation apparatus. The design, building and testing of this apparatus design experiment is an important achievement and a milestone on the road towards a working laser control experiment. The obvious next step is to test it on a molecule in some form of optical control experiment. Any control experiment using the time-resolved photoelectron spectrometer as a diagnostic tool would be a complex and challenging arrangement. Therefore, for the purposes of planning the future use of the UV pulse shaper and characterisation within such an experiment, a practical analysis of its experimental usability is given now.

First of all, the pulse shaper, XFROG and GRENOUILLE are already aligned and ready to use with visible light for the input to the pulse shaper from the OPA and with IR light for the XFROG and GRENOUILLE from the amplifier. The temporal beam overlaps for the XFROG have been determined and set by the 7 m delay line in the beam line of the IR pulse as depicted in Fig. 2.12. This means that the pulse shaper and XFROG are ready to use, and may create shaped UV pulses centred at wavelengths from 235 to 800 nm, depending on whether or not SHG is used to double the output of the shaper. Minor realignment procedures need to be undertaken from day-to-day as the OPAs are re-aligned for normal operation, but these are easily carried out using the procedure described in Section 2.5 and the markings on the laser table for the optimal positions of the optics. Similarly, cross-correlation measurements over part of the XFROG stage length may need to be undertaken in order to determine the precise overlap of the XFROG beams. This is very simple to carry out using the photoelectron spectrometer, and this is also described in Section 2.5. Control of the pulse shaper and XFROG was using Labview programs. The relations governing the control of the pulse shaper are very simple – a pair of simultaneous equations, as in Eq. 2.7 – and this needs only be combined with a phase wrapping algorithm and connected to a voltage calibration file, and a chosen phase function, to run the spatial light modulator (SLM). The SLM control program, is already written, but may very easily be re-written together with any new

desired phase function. The program to run the XFROG, which is simply a connection between Labview drivers for the delay stage and the spectrometer, has also been written. Phase retrieval from the XFROG using the output of the GRENOUILLE is very fast: the XFROG algorithm took less than one minute to converge for all the traces reported in this thesis, running on a PC. In conclusion, the pulse shaper and XFROG experiment, as presently built, provides a fast and easily used method for producing shaped deep UV light.

An alternative way of measuring a UV shaped pulse would be to use the photoelectron spectrometer to resolve the cross-correlation in a photoelectron imaging-XFROG experiment. Although the spectral resolution of the spectrometer would not be sufficient to characterise the shaped pulses in a test of the shaping method, as has been presented here, it might be sufficient to characterise some pulse shapes. The advantage of such a method is that the measurement would be *in situ* for a molecular control experiment, and thus it would be a more exact measurement of the control pulse.

Theoretical and experimental excited state dynamics of styrene

In Chapter 4, an experimental method to observe the electronic dynamics of styrene was described and demonstrated, and in Chapter 3, the ground work for further theoretical investigations of the excited electronic states of styrene was presented. The ultimate goal for the electronic structure theory presented in Chapter 3 is to extend the calculations to geometry optimisations of the excited states, and to locate crossings on between the excited states, and with the ground state. In order to do this, a better characterisation of the excited states calculated with the RASSCF methods must first be obtained. Hints from the styrene molecule calculation results in Section 3.4 that sufficient correlation energy may have been included in the CASSCF(24,32,RASSCF(1,8,1,16)) wavefunction to re-order energy of the states so that the S_2 vertical state is ionic, as per the CASPT2 results, are very promising. But this needs further work to definitively establish the nature of the S_2 wavefunction at this level of theory.

A more detailed analysis of all the time-resolved photoelectron spectra that are presented in Chapter 4 requires the determination of geometry differences between the excited states and cation states. Using this data, an attempt at an analysis of whether the $\Delta\upsilon = 0$ rule holds exactly could be carried out. Perhaps more interestingly, a theoretical decay path might be fit to the data. Also, the electronic ionisation correlations at different geometries along a possible pathway would allow a better analysis of the time-resolved photoelectron spectra. For all of these possible analyses, the wavefunctions, excitation energies and ionisation energies at all the relevant geometries would have to be quite exact. A more realistic goal would be the optimisation of critical points on the excited state surfaces, to validate the different decay mechanisms proposed from S_1. Experimentally, further studies of the decay behaviour at slightly different excitation energies between 254 nm and 240 nm could be undertaken, to find out the onset of excitation energy of the fast decay from S_1, and the onset of a significant observed photoelectron signal from S_2.

Coherent control of styrene?

A coherent control mechanism for styrene could be developed with a more concrete theoretical picture of the excited state photochemical reaction pathway. Alternatively, with more experimental studies at different excitation energies, enough information about the excited state decay could be deduced to design a control scheme. For example, a control experiment could be designed to optimise the relative times of the two decays, by enhancing or reducing the IVR in S_1 that is required for efficient decay to S_0.